Vilnius University
Faculty of Physics
Institute of Photonics and Nanotechnology

Mantas Skaržinskas

CRYSTAL STRUCTURE AND MAGNETIC PROPERTIES OF $Bi_{1-x}Ca_xFe_{1-y}Mn_yO_3$ MULTIFERROICS NEAR THE POLAR - ANTI(NON)POLAR PHASE BOUNDARY

MASTER'S FINAL THESIS

Photonics and nanotechnology study programme

Student	Mantas Skaržinskas
Supervisor	Prof. Dr. Uladzimir Khomchanka
Reviewer	Dr. Vytautas Rumbauskas
Representative of the institute	Dr. Augustas Vaitkevičius

Vilnius 2024

Contents

Introduction

Having been considered as materials of exceptional technological importance, magnetoelectric multiferroics continue to attract tremendous research interes [1]. However, despite the progress achieved in this field, a number of topics remains to be debated. In particular, the approaches allowing to combine large spontaneous magnetization and polarization in a classical room temperature multiferroic, $BiFeO_3$, were not yet proposed.

Since its properties are known to be strongly affected by chemical substitution, recognition of the doping-related factors determining the multiferroic behavior of this material would pave the way towards designing the structures with enhanced magnetoelectric functionality. Known examples of chemical substitution-related strategies to achieve spontaneous magnetization in the multiferroic $BiFeO_3$ exploit the possibility to affect the magnetic anisotropy to suppress its cycloidal antiferromagnetic structure in favour of the canted antiferromagnetic one. The maximum spontaneous magnetization associated with the canted antiferromagnetic arrangement depends on the structural characteristics and does not typically exceed 0.3 emu/g.

In this project, we intend to explore an alternative approach towards attaining a large switchable magnetization in the ferroelectric compound. I will use a doping scheme in which Fe^{3+} ions are partially replaced by manganese in the mixed (Mn^{3+}/Mn^{4+}) oxidation state providing the ferromagnetic exchange coupling Mn^{3+}: $t_{2g}^3 e_g^1$–O–Mn^{4+}: $t_{2g}^3 e_g^0$. Such an approach can be implemented on the basis of the $Bi_{1-x}AE_xFe_{1-y}Mn_yO_3$ systems (AE= alkali-earth ion), in which the charge imbalance introduced by the replacement of Bi^{3+} by AE^{2+} is compensated by the appearance of Mn^{4+} (which coexist with Mn^{3+} at $y > x$) [2].

I will carry out the systematic investigation of $Bi_{1-x}Ca_xFe_{1-y}Mn_yO_3$ multiferroics to reveal peculiarities of changes of their crystal structure and magnetic properties near the chemical substitution-stabilized polar/anti(non)polar phase boundary.

Ceramic samples of the $Bi_{1-x}Ca_xFe_{1-y}Mn_yO_3$ perovskites will be prepared by a solid-state reaction method and investigated using X-ray diffraction, scanning electron microscopy and vibrating sample magnetometry techniques.

1 Literature review

1.1 Defining Multiferroics and the Magnetoelectric Effect

Ferroelectric materials are materials that exhibit a permanent electric dipole moment, which is a separation of positive and negative charges within the material. This separation of charges creates an electric field, which can be observed as a change in the material's polarization when an external electric field is applied. Switchable electric dipole moment in the presence of an applied electric field can be described by the following equation:

$$\mu = q\boldsymbol{r}, \tag{1}$$

where μ is the dipole moment, q is the charge, and r is the vector distance between the two charges. Ferroelectric materials are characterized by their ability to switch their polarization direction upon the application of an external electric field. Not all materials with molecular dipole moments are ferroelectric, as the dipole moments must be spontaneously aligned to produce a polarization. For example, water molecules possess effective electric dipole moments, but they are randomly oriented in space and do not spontaneously polarize, so water is not a ferroelectric material [3]. The ferroelectric effect was first discovered by Valasek in 1921, in Rochelle salt, $KNaC_4H_4O_5.H_2O$ [4].

Ferroelectricity is a property exhibited only by materials with a specific crystal structure. According to [5], ferroelectricity cannot exist in centrosymmetric materials because the required dipole moment would be forced to be zero by symmetry. In addition to a lack of centrosymmetry, a material must also have a spontaneous local dipole moment. This means that the central atom must be in a non-equilibrium position, resulting in a separation of the centers of gravity of the positive and negative charges. This concept is illustrated in Fig. 1.

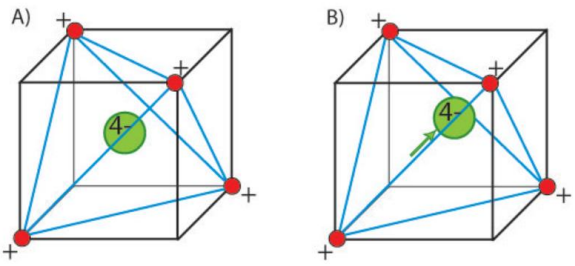

Fig. 1. The structure in (A) is non-polar because the central atom is not displaced and there is no net dipole moment. In (B), the central atom is displaced and the structure is polar, resulting in an inherent dipole moment and polarisation [3].

Ferromagnetic materials are characterized by the alignment of their atomic magnetic moments, which results in a persistent magnetic moment and the ability to be magnetized in response to external magnetic fields. Ferromagnetic materials are typically highly magnetic, with a large magnetic susceptibility and a high saturation magnetization. The saturation magnetization is the maximum magnetization that a material can attain when fully magnetized, and is a measure of the strength of the material's magnetic moment, typically expressed in units of magnetic moment per unit volume.

The high saturation magnetization of ferromagnetic materials arises from the strong alignment of their atomic magnetic moments and a high density of these moments within the material.

Ferromagnetic materials are also characterized by their Curie temperature, which is the temperature above which the material's magnetic moments become disordered and the material becomes paramagnetic. Above the Curie temperature, the thermal energy of the atoms is sufficient to disrupt the alignment of the magnetic moments, leading to the loss of ferromagnetic properties.

The magnetic properties of solids are affected by the arrangement of its atoms. We can try to imagine that we have a solid containing transition metal ions which have at least one unpaired electron in their electron configuration. Various magnetic states can arise depending on chemical bonding, as depicted in Fig. 2. In the paramagnetic state, the atomic magnetic moments are randomly oriented with respect to each other, resulting in a net magnetic moment of zero. If this crystal is subjected to an external magnetic field, these moments start to align, causing the crystal to acquire a small net magnetic moment. In a ferromagnetic crystal, the atomic magnetic moments are already aligned without the need for an external field. A ferrimagnetic crystal exhibits a net magnetic moment due to the presence of two types of atoms with magnetic moments of different magnitudes that are arranged in an antiparallel configuration (see Fig. 2). If the antiparallel magnetic moments are equal in magnitude, the crystal is antiferromagnetic and has a net magnetic moment of zero [6].

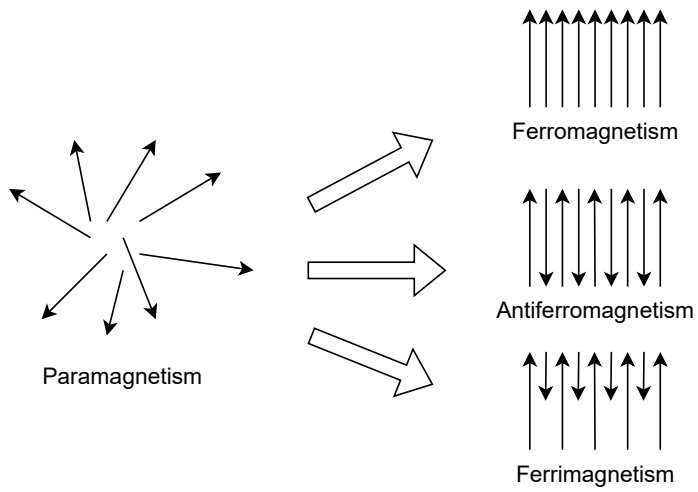

Fig. 2. The alignment of the magnetic moments of individual atoms in different materials.

If a ferromagnet with magnetic strength M is exposed to an external magnetic field of strength H, the magnetization curve in Fig. 3 is obtained. This curve shows that the magnetization of the material increases with the strength of the applied field until it reaches a saturation value, M_S. The magnetization curve also exhibits a hysteresis loop, which occurs because not all domains return to their original orientations when the applied field is decreased after the saturation magnetization is reached. As a result, when the applied field is returned to zero, there is a remnant magnetization, M_R, which can only be removed by applying a coercive field, H_C, in the opposite direction to the original field [6].

Magnetoelectric coupling refers to the phenomenon often observed in multiferroic materials, where the electric and magnetic properties are interdependent. This allows for the ability to ex-

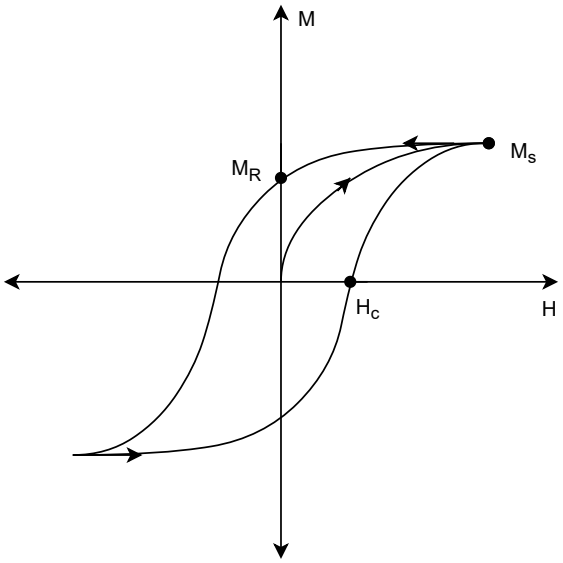

Fig. 3. The magnetization, M, as a function of the applied magnetic field, H.

ternally control the electric and magnetic properties of the material through the application of an magnetic or electric field. This phenomenon, known as the Direct ME Effect (DME) and Converse ME Effect (CME), respectively, is characterized by the coupling between ferroelectric and magnetic order parameters [7].

In DME, the electrical polarization (P) of a multiferroic material can be tuned and switched by an applied magnetic field (H). The amount of change in polarization, represented by ΔP, is proportional to the applied magnetic field, represented by ΔH, and a material-specific constant known as the ME coupling coefficient, represented by α_H. The relationship between these variables is given by the equation:

$$\Delta P = \alpha_H \Delta H. \tag{2}$$

In CME, the magnetization (M) of a multiferroic material can be tuned and switched by an applied electric field (E). The change in magnetization, represented by ΔM, is proportional to the applied electric field, represented by ΔE, and a material-specific constant known as the ME coupling coefficient, represented by α_E. The relationship between these variables is given by the equation:

$$\mu_0 \Delta M = \alpha_E \Delta E, \tag{3}$$

where μ_0 is the vacuum permeability [7].

Single phase multiferroic materials are defined as those materials that simultaneously exhibit at least two "ferroic" properties, such as ferroelectricity, ferromagnetism, or ferroelasticity. These properties are characterized by the presence of electric polarization, magnetization, or elastic deformation that can be switched by the application of an electric field, a magnetic field, or stress, respectively, as depicted in Fig. 4. More recently, the term "multiferroic" has been extended to include materials with other magnetic orders, such as ferrimagnetism or antiferromagnetism, and even to include a ferrotoroid order [8].

Ferroic materials, such as ferromagnets and ferroelectrics, exhibit spontaneous symmetry break-

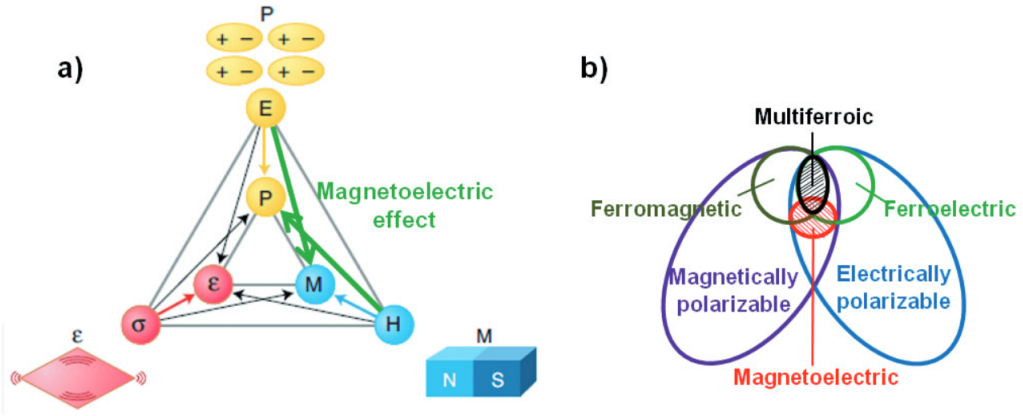

Fig. 4. (a) Phase control in ferroic and multiferroic materials can be achieved through the application of electric (E), magnetic (H), or stress (σ) fields, which control the electric polarization (P), magnetization (M), and strain (ϵ), respectively. In magnetoelectric multiferroic materials, thicker arrows indicate the ability to control P with H or M with E. (b) The relationship between ferroic, multiferroic, and magnetoelectric materials [8].

ing, which means that their ground state is not symmetric under certain transformations, such as time reversal or spatial inversion. This breaking of symmetry leads to the emergence of ferroic properties, such as magnetization in ferromagnets and electric polarization in ferroelectrics. In multiferroic materials, which exhibit both ferromagnetic and ferroelectric properties, the breaking of time-reversal and spatial-inversion symmetry can lead to magnetoelectric coupling, allowing for the possibility of externally controlling the magnetic and electric properties of the material [9].

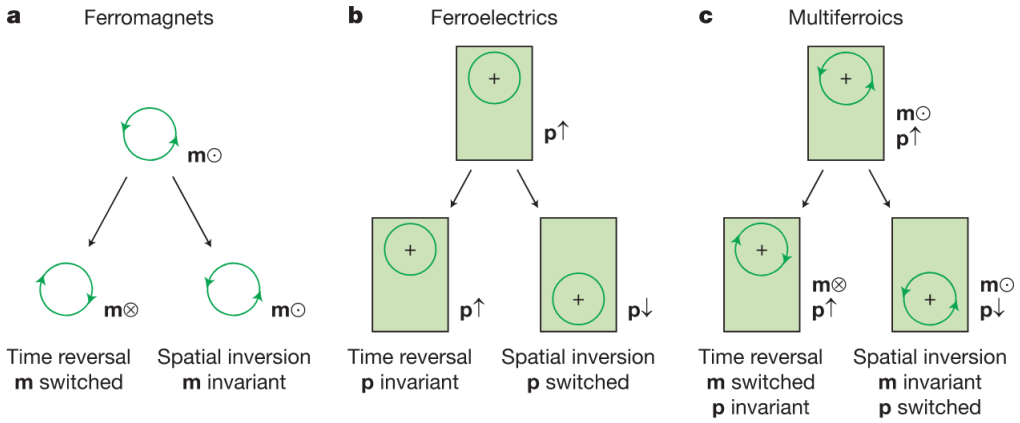

Fig. 5. a) The local magnetic moment m may be represented by a charge moving in an orbit, as indicated by the arrowheads. A spatial inversion does not affect the orbit, but a time reversal switches the direction of the orbit and thus m. b) The local dipole moment p may be represented by a positive point charge asymmetrically positioned within a unit cell with no net charge. There is no time dependence in p, but a spatial inversion reverses the direction of p. c) Multiferroics which exhibit both ferromagnetic and ferroelectric properties, do not have either time-reversal or spatial-inversion symmetry [9].

1.2 Exploring the Untapped Potential of Magnetoelectric Multiferroics

Ideal magnetoelectric (ME) multiferroics (MF) are materials that simultaneously exhibit both ferromagnetic and ferroelectric properties in the same phase and show a linear coupling between these properties. These materials have garnered significant research interest due to their potential multifunctional applications in modern technologies, as well as the fundamental physics involved. ME multiferroics display a magnetoelectric coupling, in which the spontaneous magnetization can be switched by an applied electric field, and the spontaneous electrical polarization can be switched by an applied magnetic field, due to the cross coupling between ferroelectric and ferromagnetic ordering. In addition to these properties, multiferroics may offer additional functional parameters, such as the ability to have more than two logic states, for a wide range of new applications [10].

These materials have a number of potential applications, including:

- Sensors: Medical diagnostics that rely on electrical signal acquisition methods, like electrocardiography (ECG) and electroencephalography (EEG), have been extensively studied and are now commonly used in clinical practice [11]. Currently, researchers are investigating room-temperature magnetic field sensors, including optically pumped magnetometers, xMR sensors, orthogonal fluxgates, and more. These sensors offer several benefits, including contactless signal acquisition, increased precision, and improved positioning. Obtaining biomagnetic signals is advantageous compared to traditional electrical methods due to their improved spatial resolution, reduced interference, and lack of susceptibility to changes in the body's composition [12].

  Research on thin-film magnetoelectric (ME) sensors is particularly noteworthy as it allows for new opportunities in medical signal acquisition. These sensors do not require cooling or heating to function, making them easy to use and providing unprecedented flexibility. Additionally, they are able to operate in the presence of interference fields, such as the Earth's magnetic field, which opens up new possibilities for their use in medicine [13–15]. Magnetic recording methods are believed to have the potential to take over and substitute traditional electrical methods. The effectiveness of a magnetic field sensor is generally defined by its unique characteristics such as operational temperature, inherent noise, dynamic range, bandwidth and sensitivity [16, 17].

- Energy harvesting: Magnetoelectric multiferroics can be used to convert energy from one form (e.g., magnetic energy) into another form (e.g., electrical energy) for use in applications such as energy harvesting. According to [18], a movable permanent magnet and a pair of piezoelectric (PIN-PMN-PT single crystal plates)/magnetostrictive (multilayer amorphous FeBSi alloys) ME laminates were used to harvest biomechanical energy. The excellent ME coupling properties of the laminates allowed the harvester to efficiently convert mechanical energy into electrical energy. The ME harvester exhibited a high output performance, with an open-circuit voltage of approximately 17 V and a short-circuit current of around 7.2 μA, under simulated human running conditions (mechanical excitation at 18 m/s^2 and 2 Hz). This was sufficient to power 7 LEDs simultaneously, charge a capacitor, or recharge a lithium-

polymer battery. Many wearable and portable electronics rely on lithium-ion batteries as their power source, which can pose challenges in terms of sustainability. The multiferroic module is capable of harvesting biomechanical energy to power LEDs, temperature and humidity sensors, or even serve as an external power supply to charge lithium-ion batteries in personal electronics. This makes it an ideal solution for small-scale energy scavenging in sustainable personal electronics and Internet of Things applications, as it can meet demands for low-power electronic devices.

- Spintronics: Has been actively studied for the past 30 years which involves the use of conventional ferromagnets and utilizes the spin of electrons in addition to their charge state. This field has the potential to revolutionize electronics by incorporating the quantum mechanical property of spin into the foundation of electronic devices [19].

  There are already several commercial products that utilize spintronic technology, such as the magnetoresistance (TMR) read head in some hard disk drives. These spintronic devices have the potential to offer faster data processing and lower power consumption. Additionally, spintronics can be easily integrated with magnetic systems, such as data storage, and provides new approaches for addressing the limitations of current CMOS technology [20].

  Antiferromagnetic (AFM) materials do not produce stray fields, which allows for increased information density in storage devices because the memory cells do not interfere with each other. Additionally, antiferromagnetic materials have faster spin response times, making them attractive for use in high frequency applications such as THz communication and data transfer. This is because ferromagnets typically resonate in the GHz range, while AFMs can operate at higher frequencies. A large percentage of known magnetic materials, including various types of semiconductors, insulators, and metals, are actually AFMs, which provides a wide range of options for device design [21].

  The terahertz (THz) band, which ranges from 0.1 to 30 THz, has data rates that exceed current technology, making it a promising candidate for next-generation wireless communication and ultrahigh-speed data processing. However, a lack of materials that can operate at these frequencies has hindered the development of THz devices. The discovery of THz spin currents at sub-picosecond timescales has opened up new possibilities for ultrafast data processing using femtosecond laser excitation of ferromagnets. To further advance THz device integration and applications, there is a need for a low-energy electric field to control THz spin currents [22].

  Single phase magnetoelectric (ME) multiferroic materials, can be used to explore new ways of manipulating spin transport in devices. These materials are insulators and have unique magnetic structures, like spirals or cones, that can be controlled by both magnetic and electric fields. Research on spin transport in these ME multiferroic materials could lead to the development of energy-efficient spintronic applications that use electrical voltage to control spin transport [23].

  The ability of multiferroic materials, particularly BFO, to exhibit magnetoelectric coupling presents an alternative way to control AFM-based devices. If the AFM order parameter can

be controlled using low-dissipation electric fields, it may be possible to significantly improve AFM spintronic devices. BFO's magnetoelectric coupling has been used to control the AFM state (either cycloidal or G-type AFM) using an applied electric field, which has led to great interest of using BFO in AFM spintronics research [24].

- Photovoltaics: multiferroic materials have the potential to be used in photovoltaics due to their low band gap, which is similar to the photovoltaic effect in ferroelectrics [25]. When a photon is absorbed by a dipole, the electron and hole in the pair become separated. The electric field in the ferroelectric crystal, which is caused by the separation of charge carriers, maintains the separation and results in an open circuit voltage (V_{oc}) [25].

  Ferroelectric materials traditionally have a low power conversion efficiency (PEC) of around 1% due to their wide band gap [26]. However, multiferroic oxides, which have a low band gap, have been used to improve the PEC of photovoltaic cells. A PEC of 8.1% has been reported for Bi_2FeCrO_6 thin film solar cells using this approach [27].

  $BiFeO_3$ is a multiferroic material that has been extensively studied for its potential use in photovoltaic cells due to its tunable band gap, which can be modified through doping [28–30]. Recently, the prediction of a linear spin photovoltaic effect in $BiFeO_3$ has opened the possibility for the integration of spintronics with optoelectronics. This spin-dependent photovoltaic response has been observed experimentally in a 2D hybrid organic-inorganic perovskite [31].

- Magnetoelectric nanoparticles: using MENPs, it is possible to wirelessly access and manipulate the internal mechanisms within cells, giving the ability to control basic biological processes. This technology can overcome the limitations of using electric fields to control biological processes, as electricity is already present in these processes. The ME effect allows remotely applied magnetic fields to generate or detect local electric fields near the nanoparticles. This can be used for both stimulating or recording purposes [32].

  Ideally, the ME effect of MENPs allows to overcome the limitations of current stimulation technologies. This was first proposed in a theoretical study by [33]. The free energy, G, that accounts for the interaction between the electric field, E, and the magnetic field, H, in the second order approximation can be described using the Landau theory of multiferroics.

$$G(E,H) = -\alpha_{ij}E_iH_j \rightarrow \Delta P_i = -\partial G/\partial E_i = \alpha_{ij}H_j, \tag{4}$$

  here α_{ij} represents the nanoparticles magnetoelectric coefficient tensor and P represents the polarization. When a nanoparticle acts like an electric dipole, an applied magnetic field can induce a local electric field in the vicinity of the nanoparticle. The proportionality between the magnetic field and the induced electric field is defined by the nanoparticles' magnetoelectric coefficient. For example, if the magnetoelectric coefficient is 10 V cm^{-1} Oe^{-1}, then the application of a 1000 Oe magnetic field would induce an electric field of approximately 10,000 V/cm (or 1 mV/nm) [34].

According to the principle of reciprocity, if MENPs can be used to stimulate neurons (write information), they can also be used to record neural activity (read information). This is achieved through the use of the converse magnetoelectric effect of MENPs, which occurs when an external electric field causes a change in the magnetization of the nanoparticles.

$$G(E,H) = -\alpha_{ij}E_iH_j \rightarrow \Delta M_i = -\partial G/\partial H_i = \alpha_{ij}E_j, \tag{5}$$

where magnetization of the nanoparticles is represented by M_i and affected by changes in the electric field near the nanoparticle. If the electric field changes due to neural activity, it will cause a change in the magnetization. This change can be detected using a magnetic field sensor or magnetic imaging technique, such as MRI or magnetic particle imaging (MPI). In a theoretical paper [35] Guduru proposed that the converse magnetoelectric effects of MENPs could be used in conjunction with MRI or MPI to detect neural activity.

Fig. 6. Idea of using MENPs to create a wireless brain-machine interface that can communicate both ways. The MENPs are depicted as bright circles within the brain [34].

Despite their potential, the practical applications of magnetoelectric multiferroics are still in the early stages of development and much research is needed to fully realize their potential. Further progress will require the discovery of new magnetoelectric multiferroic materials and the development of new fabrication techniques that can produce these materials on a large scale.

1.3 Categorizing Multiferroics: Single-Phase Materials and Composites

Single-phase multiferroics are materials that exhibit both ferroelectric and magnetic ordering in a single chemical compound. These materials can be further divided into two categories: type-I and type-II.

Type-I, in which ferroelectricity and magnetism appear largely independently, are fairly common and often have good ferroelectric properties, with high critical temperatures for their magnetic and ferroelectric transitions. However, the coupling between their magnetism and ferroelectricity is typically relatively weak. Researchers are interested in finding ways to improve this coupling while maintaining the other beneficial characteristics of these materials. There are several different subclasses of type-I multiferroics, which can be distinguished based on the mechanism responsible for their ferroelectricity (see Fig. 7) [36].

Multiferroic perovskites are the most widely studied Type-I materials. Some of the most well-known ferroelectric materials are perovskites, such as $BiFeO_3$ and $Pb(ZrTi)O_3$ (PZT). There are also a large number of magnetic materials that belong to the perovskite family [37]. Ferroelectricity in transition metal perovskites, which contain ions such as Ti^{4+}, Ta^{5+}, and W^{6+} with empty d shells, is typically caused by the off-center shifts of these transition metal ions. These shifts allow the transition metal ions to form strong covalent bonds with one or three oxygens, using their empty d states. On the other hand, the presence of real d electrons in d^n configurations of magnetic transition metals can inhibit this process and prevent ferroelectricity in magnetic perovskites. This phenomenon, known as the "d^0 vs d^n problem," has been the subject of much study, but a full solution to this problem has yet to be found [36, 38, 39].

It is thought that the reason for the mutual exclusion between ferroelectricity and magnetism in certain materials may not be a fundamental principle, but rather a matter of probability. In most cases, a magnetic d^n ion is stable in the center of its O_6 octahedra, but there may be exceptions to this rule. One potential solution to this problem may be the use of "mixed" perovskites that contain both d^0 and d^n ions, as shown in Fig. 7. However, the coupling between the magnetic and ferroelectric subsystems in these mixed perovskites is typically quite weak [36].

In Type-II single-phase multiferroic materials ferroelectricity only exists in a magnetically ordered state and is caused by a specific type of magnetism. For example, in $TbMnO_3$, magnetic ordering occurs at T_{N1} = 41 K, and at a lower temperature, T_{N2} = 28 K, the magnetic structure changes. It is only in the low-temperature phase that a nonzero electric polarization appears. Similar behavior is observed in $TbMn_2O_5$ [40]. The first study of $TbMnO_3$ found that a magnetic field can significantly impact the electric polarization of this material. For example, in $TbMnO_3$, the polarization rotates or "flops" by 90 degrees when a critical magnetic field is applied along a specific direction [40]. According to [41], in $TbMn_2O_5$, the influence of an external field is even stronger than in $TbMnO_3$. The polarization of $TbMn_2O_5$ changes sign with the field, and an alternating field of +1.5 to -1.5 Tesla leads to corresponding oscillations in the polarization.

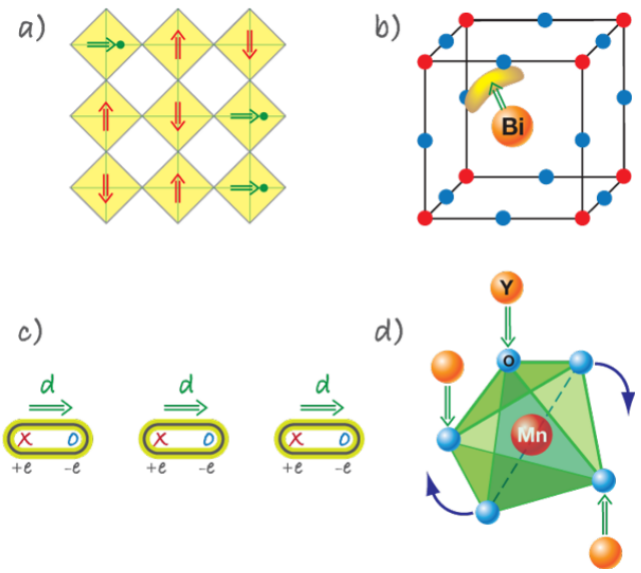

Fig. 7. There are several different mechanisms that can give rise to ferroelectricity in type-I multiferroics. One example is the use of "mixed" perovskites that contain both ferroelectrically active d^0 ions and magnetic d^n ions, as shown in a). In this case, shifts of the d^0 ions from the centers of the O_6 octahedra can lead to polarization (green arrows), while the magnetic order (red arrows) remains. b) The use of materials such as $BiFeO_3$ and $PbVO_3$, in which the ordering of lone pairs (yellow "lobes") of Bi^{3+} and Pb^{2+} ions (orange) contributes to the polarization (green arrow). c) In charge-ordered systems, the coexistence of inequivalent sites with different charges and inequivalent (long and short) bonds can lead to ferroelectricity. d) The "geometric" mechanism in $YMnO_3$ involves the tilting of a rigid MnO_5 block with a magnetic Mn at the center, resulting in the formation of dipoles (green arrows) and ferroelectricity (green arrows) when the Mn spins order at lower temperatures [36].

Type-II multiferroic materials can be divided into two groups based on the mechanism responsible for their multiferroic behavior. The first group includes materials in which ferroelectricity is caused by a specific type of magnetic spiral. The second group consists of materials in which ferroelectricity appears even for collinear magnetic structures.

Spiral type-II multiferroics. Most known type-II multiferroic materials belong to a subgroup in which ferroelectricity appears in conjunction with a spiraling magnetic phase, often of the cycloid type. This is the case in $TbMnO_3$, $Ni_3V_2O_6$, and $MnWO_4$. In $TbMnO_3$, below T_{N1} = 41 K, the magnetic structure is a sinusoidal spin-density wave, where all spins point in one direction but the size of the local moment varies periodically in space. Below T_{N2} = 28 K, the Mn spins order in a way that the tip of the spins trace out a cycloid, see Fig. 8 [36].

Katsura, Nagaosa, and Balatsky [42] and Mostovoy [43] demonstrated that in a cycloidal spiral, a polarization (P) appears that can be expressed as:

$$P \sim r_{ij} \times [S_i \times S_j] \sim [Q \times e], \tag{6}$$

where r_{ij} is the vector connecting neighboring spins S_i and S_j, Q is the wave vector describing the spiral, and $e \sim [S_i \times S_j]$ is the spin rotation axis. The microscopic mechanism behind this polarization involves the spin-orbit interaction [42, 43].

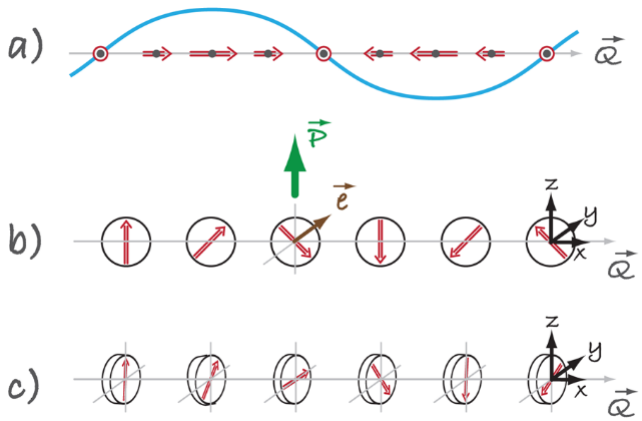

Fig. 8. Illustrates three different types of spin structures that are relevant for type-II multiferroic materials. (a) A sinusoidal spin density wave, in which the direction of the spins is constant but their magnitude varies. This structure is symmetrical about its center and therefore does not exhibit ferroelectricity. (b) A cycloidal spiral with the wave vector Q = Q_x and spins rotating in the (x,z)-plane. In this case, a nonzero polarization $P_z \neq 0$ is observed. (c) In a so-called "proper screw," the spins rotate in a plane perpendicular to Q. In this case, the inversion symmetry is broken, but most often it does not result in polarization, although in some cases it may [44].

Multiferroic materials with collinear magnetic structures of Type II often exhibit polarization due to exchange striction, as the magnetic coupling varies based on the positions of the atoms. An example of this is found in Ca_3CoMnO_6, a material consisting of chains of alternating Co^{2+} and Mn^{4+} ions. At high temperatures, the distances between the ions along the chain are equal, the chain has inversion symmetry, and no polarization is present [45].

Magnetic ordering breaks inversion symmetry, as the spins form a ↑↑↓↓ type magnetic structure. This results in a different distortion of ferro and antiferro bonds (↑↑ and ↑↓) due to exchange striction, leading to the situation shown in Fig. 7 where the material becomes ferroelectric. Theoretical calculations support this explanation [46].

Exchange striction, a phenomenon that arises due to the different distortions of ferro and antiferro bonds, can lead to ferroelectricity in multiferroic materials with collinear magnetic structures. This occurs when transition metal ions with different valences are present, or when the exchange between metal ions occurs through intermediate oxygens and depends on both the distance between the metal ions and the metal-oxygen-metal bond angle. In the latter case, the Mn magnetic order in the basal plane of $RMnO_3$ perovskites (where R is a small rare earth) can cause the oxygen ions to shift perpendicular to the Mn-Mn bonds, resulting in a polarization along the direction of the shift [47–49]. Ferroelectricity can also occur in collinear magnets through a mechanism known as "electronic" ferroelectricity in frustrated magnets. Here, the polarization of a triangle of spins is proportional to the spin correlation function:

$$S_1(S_2 + S_3) - 2S_2S_3, \tag{7}$$

where the numbers denote positions on the vertices of the triangle. If this function is nonzero, the polarization will also be nonzero [50].

Composite multiferroics are materials that are composed of multiple phases, each of which exhibits either ferroelectric or ferromagnetic ordering. The multiferroicity in these materials is not intrinsic to the material itself, but rather arises from the combination of the individual phases. Magnetoelectric (ME) composites, which are made up of ferromagnetic magnetostrictive and ferroelectric piezoelectric components, have been developed as an alternative to single-phase materials that can operate efficiently at room temperature. These composites can be fabricated in granular or layered arrangements, and in theory, the coupling between the components can be up to 10^8 times stronger than in single-phase materials. In single-phase ME materials, coupling occurs through direct polarization-magnetization interactions, while in ME composites, coupling occurs extrinsically through one of three mechanisms: strain, charge carrier, or spin exchange. The strain-mediated ME coupling mechanism is well-established, while the other two mechanisms are still in their early stages of development [51].

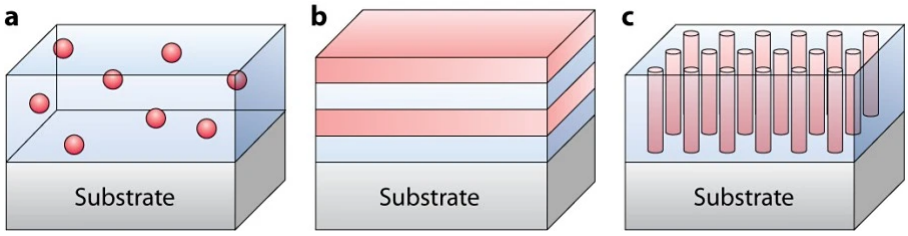

Fig. 9. A schematic illustration shows three types of ME composite nanostructures with common connectivity schemes: a) nanocomposite films with magnetic particles embedded in a ferroelectric film matrix. b) Horizontal heterostructure with alternating ferroelectric and magnetic layers, or a ferroelectric (or magnetic) thin film grown on a magnetic (or ferroelectric) substrate. c) Vertical heterostructure with one-phase nanopillars embedded in a matrix of another phase [52].

In essence, single-phase (Type-I and Type-II) multiferroic materials are both ferroelectric and magnetically-ordered materials, but there are some important distinctions between the two.

- The degree of connection between the magnetic and ferroelectric properties of Type-I and Type-II multiferroics differs significantly. Magnetism and ferroelectricity are often weakly coupled in Type-I multiferroics, whereas they are strongly coupled in Type-II multiferroics.
- The critical temperature at which their magnetic and ferroelectric transitions take place is another distinction between the two varieties of multiferroics. While Type-II multiferroics often have lower critical temperatures, Type-I multiferroics frequently have quite high critical temperatures.

On the other hand, composite multiferroics are materials made up of multiple phases that exhibit ferroelectric or ferromagnetic ordering due to the combination of the individual phases. ME composites, made of ferromagnetic magnetostrictive and ferroelectric piezoelectric components, are an alternative to single-phase materials with strong coupling between their components.

1.4 Popularity of $BiFeO_3$

An ideal multiferroic material is expected to be both ferromagnetic and ferroelectric, and demonstrate strong coupling between magnetization and polarization at room temperature. Since such a material has not been discovered so far, much attention now focuses on the antiferromagnetic and ferroelectric bismuth iron oxide ($BiFeO_3$), which possesses exceptionally high transition temperatures. It has ferroelectricity with a high Curie temperature (T_C = 820-850°C) and antiferromagnetic properties below the Néel temperature (T_N = 350-380 °C) [53–56].

Further more, $BiFeO_3$ is known for its very large spontaneous polarization ($P_s \sim 100\mu C\ cm^{-2}$) and superimposed incommensurate cycloid spin structure with a periodicity of 620 Å along the $[110]_h$ axis (where h stands for "hexagonal") at room temperature [57, 58].

The electric polarization arising from the stereochemical activity of the lone pair electrons of Bi^{3+} affects the G-type antiferromagnetic arrangement stabilized by the Fe^{3+}: $t_{2g}^3 e_g^2$ –O–Fe^{3+}: $t_{2g}^3 e_g^2$ superexchange thus giving rise to the cycloidal modulation of the AFM order. This cycloidal modulation cancels any linear magnetoelectric effect, however, researchers have shown that reducing the particle size of $BiFeO_3$ can suppress the cycloid structure and increase the material's magnetic moment [59, 60].

On top of that, linear ME coupling can be observed in phases with cone-type or canted AFM structures stabilized by a strong (10 − 15T at room temperature) magnetic field, epitaxial strain or chemical substitution. Also $BiFeO_3$ exhibits notable changes in dielectric properties near its magnetic transition temperature [60].

One of the main challenges in using $BiFeO_3$ is its large leakage current, which is caused by the presence of impure phases such as $Bi_2Fe_4O_9$ and $Bi_{25}FeO_{39}$ [61]. However, $BiFeO_3$ is relatively simple to synthesize, which makes it attractive for use in device fabrication. It can be synthesized using a variety of methods, including the sol-gel method, precipitation - coprecipitation, hydrothermal synthesis, high energy ball milling, and liquid phase sintering with a high heating rate (100 °/s). Researchers have also extensively studied solid solution systems between $BiFeO_3$ and other ferroelectric materials such as $PbTiO_3$, $SrBi_2Nb_2O_9$ [58–60, 62, 63].

In conclusion, $BiFeO_3$ is a highly promising material for multiferroic applications due to its high transition temperatures, large spontaneous polarization, and potential for strong coupling between magnetization and polarization at room temperature. Despite the challenges of large leakage current caused by impurities and difficulty in observing linear ME effect due to its cycloidal modulation, researchers have found ways to suppress the cycloid structure and increase the magnetic moment by reducing particle size and applying external factors such as magnetic field, epitaxial strain or chemical substitution. Furthermore, $BiFeO_3$ is relatively simple to synthesize using various methods, and solid solution systems between $BiFeO_3$ and other ferroelectric materials have also been extensively studied. Overall, $BiFeO_3$ is a material with great potential for future multiferroic applications and research in this area is ongoing.

1.5 Crystal structure of $BiFeO_3$

At room temperature and atmospheric pressure, the crystal structure of $BiFeO_3$ exhibits a rhombohedrally distorted perovskite arrangement, which belongs to the R3c symmetry group (that allows polar atomic displacements along the 3-fold rotational axis). The unit cell parameters of this structure are $a_{rh} = 3.965$ Å and $\alpha_{rh} = 89.3 - 89.4°$. Additionally, the unit cell can be described in terms of hexagonal symmetry, with lattice constants $a_{hex} = b_{hex} = 5.58$ Å and $c_{hex} = 13.90$ Å. The rotation angle of the oxygen octahedra, which is related to the Goldschmidt tolerance factor (t) for perovskites, is a significant structural parameter in $BiFeO_3$. The tolerance factor t for $BiFeO_3$ is 0.88, leading to a requirement for the oxygen octahedra to deform in order to fit into the unit cell, resulting in a Fe-O-Fe angle (θ) of 154-156° [64].

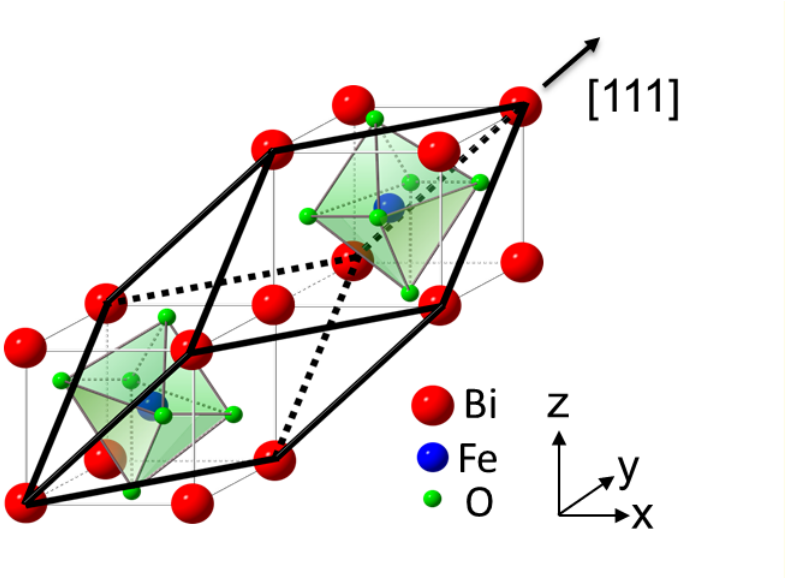

Fig. 10. A schematic illustration of the crystal structure of the perovskite $BiFeO_3$ (space group: R3c) is shown, with two crystals depicted along the [111] direction [65].

In some cases, there have been discrepancies found regarding the crystal structure of α-$BiFeO_3$ at room temperature. For instance, in crystals with a grain size smaller than 30 nm, a change from rhombohedral to cubic symmetry has been observed [66].The structure of epitaxial $BiFeO_3$ films has also been suggested to be rhombohedral, tetragonal, or monoclinic [67, 68].

In Fig. 11 a, b the [111] direction is depicted as the axis of rotation for antiferrodistortive (AFD) octahedral tilting ($a^-a^-a^-$ in Glazer notation) [69]. The unit cell of $BiFeO_3$ is distorted due to the mismatch of ionic radius (when considering the tolerance factor [70]), resulting in a rotation angle of the octahedra of more than 11° [71,72]. This antiphase tilting of the octahedra leads to an effective doubling of the pseudocubic unit cell, forming the rhombohedral unit cell as shown in Fig. 11 b. The hexagonal setting (denoted by the subscript "h" in Fig. 11 c) is often used to describe $BiFeO_3$. The correspondence between the cubic, rhombohedral, and hexagonal unit cells is depicted in Fig. 11 d.

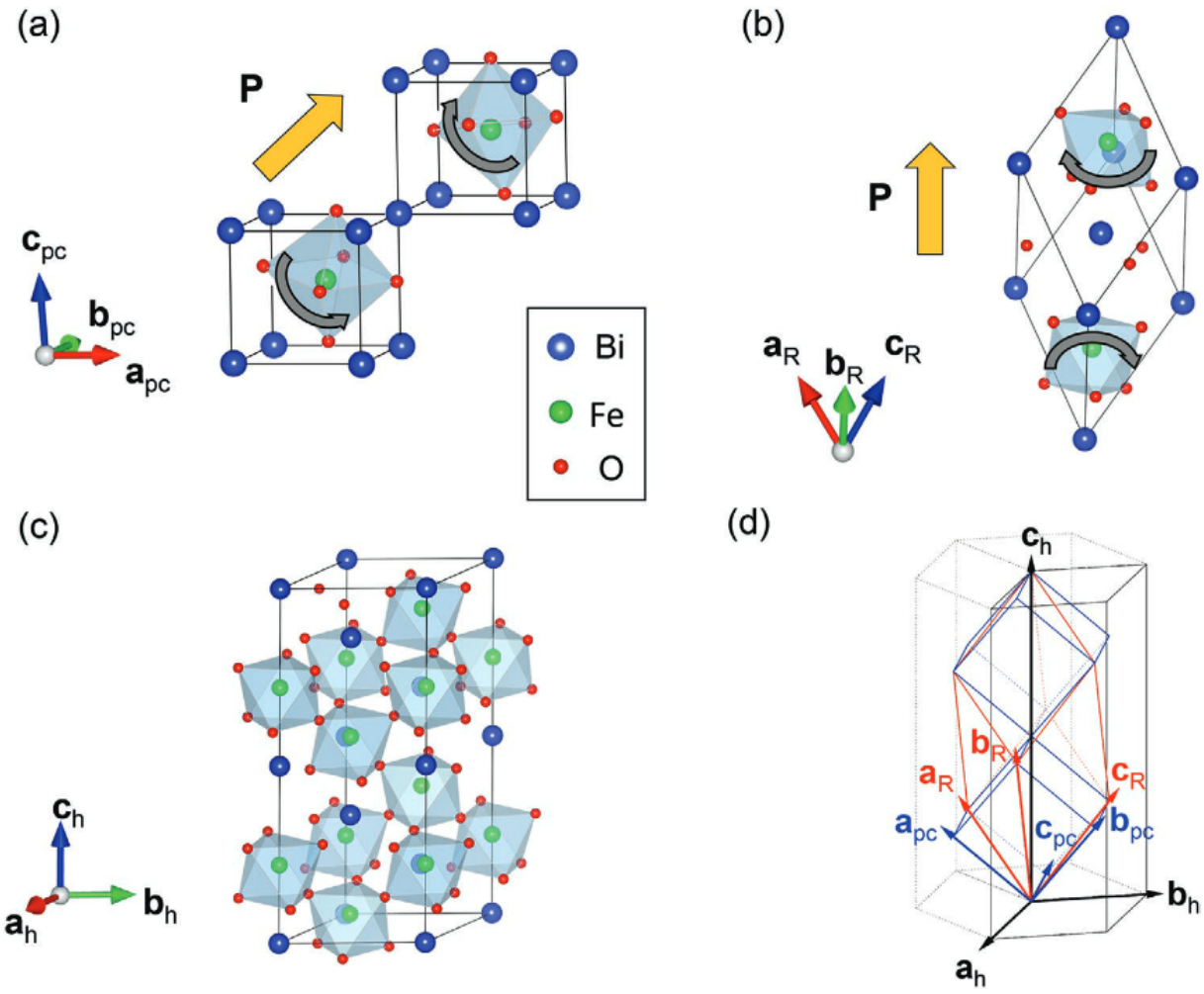

Fig. 11. In several ways, the crystal structure of $BiFeO_3$ can be depicted. Figure a) shows two pseudocubic perovskite unit cells combined along the [111] direction to form the doubled $BiFeO_3$ unit cell, with bismuth ions appearing as blue, Fe ions as green, and oxygen as red. The rhombohedral unit cell is illustrated in b) with the P direction along [111]. The hexagonal unit cell, made up of 6 pseudocubic unit cells, is depicted in c). Correspondences between the hexagonal (black lines), rhombohedral (red lines), and pseudocubic (blue lines) representations of the $BiFeO_3$ unit cells are shown in d). The directions of rotations of oxygen octahedra are represented by the curved arrows, while the orange arrows indicate the direction of ferroelectric polarization [73].

1.6 Magnetic structure of $BiFeO_3$

In the unit cell, the magnetic structure of $BiFeO_3$ is determined by the superexchange interaction through the Fe-O-Fe bond, which has an exchange energy of -5.3 meV. A Dzyaloshinskii-Moriya interaction, which is smaller by an order of magnitude and results from the inhomogeneous magnetoelectric interaction, causes a spin cycloid with a long period of approximately 62 nm [74]. A second Dzyaloshinskii-Moriya interaction, which is smaller by another order of magnitude and results from the rotation of the oxygen octahedra, leads to a periodic canting of the cycloid and therefore a spin density wave perpendicular to the plane of the cycloid [73, 75]. This second Dzyaloshinskii-Moriya interaction also causes a weak ferromagnetic moment, but this is averaged to zero in the cycloidal state. If the cycloid is suppressed by factors such as high magnetic field, strain, or doping, the weak ferromagnetic moment can be observed.

The long-range incommensurate spin cycloid structure of bismuth ferrite [76], which is schematically illustrated in Fig. 12 a, has a periodicity of 62 nm in the bulk. It typically propagates along one of three crystallographic directions:

$$k_1 = [-110],$$

$$k_2 = [0-11],$$

$$k_3 = [10-1].$$

In Fig. 12 b, c, where k_i represents all three possible propagation vectors (i = 1, 2, 3). Propagation vectors are all contained within the (111) plane, i.e., the propagation vector k_i is orthogonal to the P direction [111]. The rotation axis of the spins (the cycloid plane) is typically confined to the plane defined by k_i and P (Fig. 12 a). For example, for the k_1 propagation vector and $P \parallel [111]$, the cycloid plane is $k_i \times P = (11-2)$.

It's important to mention that in epitaxial thin films, a different kind of spin order, which is called the type-2 cycloid, has been observed [77–80]. This cycloid, which has (to date) not been observed in the bulk, propagates along one of the following three directions (for $P \parallel [111]$):

$$k_1' = [-211],$$

$$k_2' = [1-21],$$

$$k_3' = [11-2].$$

In Fig. 12 d, e note that these k_i vectors still remain orthogonal to the polarization direction [111]. Interestingly, in contrast with the type-1 cycloids, the type-2 cycloid k vectors do not link the next-nearest Fe sites. The fact that this spin order has not been observed in the bulk suggests that additional anisotropy terms arising from epitaxial strain are required to stabilize it.

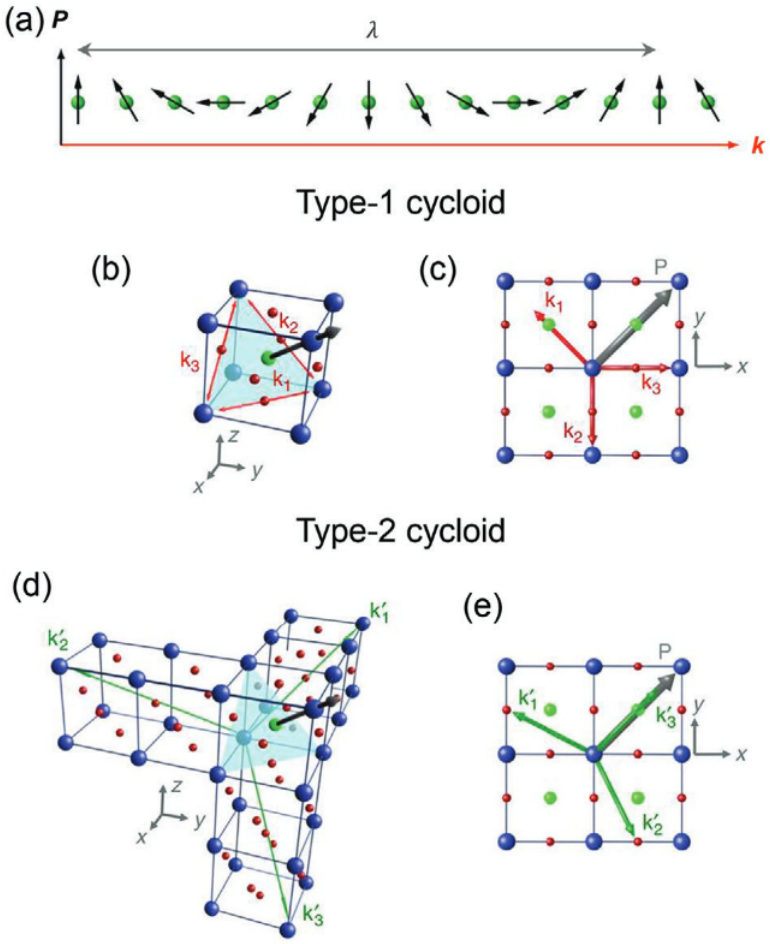

Fig. 12. Representation of spin cycloids in $BiFeO_3$. a) Cycloid manifests as a gradual rotation of the antiferromagnetically coupled spins along the propagation vector k. The spins rotate in a plane defined by k and P (typically $P \parallel [111]$). The cycloid period λ is about 62-64 nm in the bulk. b) The type-1 cycloid, which is commonly observed in bulk samples with it's propagation vectors. c) Shows the projection of the type-1 cycloid k vectors on the film plane for (001) oriented films. d) The type-2 cycloids, which have only been observed in thin film samples of $BiFeO_3$ with their propagation vectors. It's showing the projection of the type-2 cycloid k' vectors on the film plane for the (001) crystallographic orientation. Bismuth ions are represented as blue, Fe ions as green, and oxygen as red [79].

1.7 Addressing Weaknesses in $BiFeO_3$ Cycloidal Spin Ordering

The cycloid in bulk samples of $BiFeO_3$ can average out the weak canted ferromagnetic moment over its period and suppress the linear magnetoelectric effect [81]. Researchers attempt to eliminate the cycloid in $BiFeO_3$ films in order to release the "latent magnetic moment" and enhance the linear magnetoelectric effect. It was also found that a large magnetic field could be used to access the linear magnetoelectric effect in single crystal $BiFeO_3$ [82]. The spin ordering of the magnetic cycloid can be perturbed through various means:

- External fields:
    - a) Magnetic Fields
    - b) Electric Fields
- Chemical and Hydrostatic Pressure:
    - a) Doping
    - b) Pressure
- Strain Engineering:
    - a) Biaxial Strain—(001) Orientation
    - b) Uniaxial Strain—(110) Orientation

Magnetic fields. It is expected that the cycloid, as a magnetic modulation, would be sensitive to applied magnetic fields [83]. The ground state energy of a homogeneous G-type anti-ferromagnetic (AFM) material decreases significantly when the magnetic field strength is above a critical value, H_{cr}. This is because the AFM state becomes more energetically favorable than the cycloid state at these field values. The critical field can be calculated using the exchange stiffness (A), cycloid wavenumber ($q_0 = \frac{2\pi}{\lambda}$), and transverse magnetic susceptibility ($\chi_\perp$) of the material. These values can be plugged into the following equation:

$$H_{cr} = (\frac{4Aq_o^2}{\chi_\perp})^{\frac{1}{2}}. \tag{8}$$

For the specific material being considered, the estimated values for these parameters are $A = 3 \times 10^{-7}$ erg cm^{-1}, $\chi_\perp = 4.7 \times 10^{-5}$, and $\lambda = 62$ nm. It's important to note that this equation only applies when the magnetic field is applied parallel to the polar axis. To calculate the critical field when the field is applied at an arbitrary angle, the magnetization and anisotropy of the material must also be taken into account [81, 83].

Electric fields. In 1994, Sparavigna et al. published the first study on the effects of electric fields on the spatially modulated spin structure in BFO. They compared the response of BFO to electric fields with the behavior of nematic liquid crystals under such fields, and also explored the combined impact of electric and magnetic fields on the critical magnetic field (H_{cr}) required for the transition from a modulated spin structure to a homogeneous AFM order. The authors predicted that the application of an electric field along the $[001]_h$ direction would reduce H_{cr} [84].

Doping. Over the past decade, there has been a great deal of interest in the possibility of doping BFO to enhance its functional properties [85], drawing on the success of doping in piezoelectric materials such as $Pb(Zr_xTi_{1-x})O_3$ (PZT) and $Pb(Mg_{1/3}Nb_{2/3})O_3$-$PbTiO_3$ (PMN-PT). In BFO, efforts have been made to improve the material through two primary mechanisms. One approach involves doping the A-site, which has a significant impact on the polarization and piezoelectric properties of BFO due to the central role played by the bismuth lone pair [64] in determining the ferroelectric order of the material [86]. The other approach involves doping the B-site, which is used to modify or enhance the magnetic characteristics (including the weak magnetic moment) and multiferroic coupling of BFO [74, 87]. It is thought that any changes to the polarization in BFO, which is closely related to the cycloid, will also affect the cycloid.

Epitaxial strain occurs when a thin film is grown on a single crystal substrate and the lattice parameters of the film and substrate do not match. The misfit strain, which is a measure of this mismatch, can be expressed as a percentage using the equation:

$$\epsilon = \frac{a_{sub} - a_{bulk}}{a_{bulk}} \times 100\%, \tag{9}$$

where a_{bulk} is the bulk pseudocubic lattice parameter of the film and a_{sub} is the pseudocubic lattice parameter of the substrate.

If a film is grown coherently on a substrate with a smaller lattice parameter, it will experience compressive strain in the plane (denoted as negative), while a film grown on a substrate with a larger lattice parameter will experience tensile strain (denoted as positive). However, this strain cannot be sustained indefinitely and will eventually be relieved through the formation of misfit dislocations in the film beyond a certain thickness, known as the Matthews-Blakeslee limit [88]. This process leads to an exponential strain profile and a strain gradient, which can impact the physical characteristics of the film such as ferroelectric and magnetic orders [89].

In conclusion, the cycloidal spin ordering in $BiFeO_3$ can suppress the linear magnetoelectric effect and researchers have attempted to modify or eliminate the cycloid in order to enhance this effect. Various methods have been explored to perturb the spin ordering, including applying external magnetic or electric fields, applying chemical and hydrostatic pressure through doping or pressure techniques, and using strain engineering. It is expected that the cycloid will be sensitive to applied magnetic fields and that the critical field required for a transition from a modulated spin structure to a homogeneous AFM order can be calculated using certain material parameters. Electric fields applied along the $[001]_h$ direction have been predicted to reduce the critical field, and both A-site and B-site doping have been explored as methods for modifying the polarization and magnetic characteristics of $BiFeO_3$. Strain engineering has also been shown to be an effective method for modifying the cycloid and enhancing the linear magnetoelectric effect, particularly through the use of biaxial strain in the [001] orientation or uniaxial strain in the [110] orientation.

1.8 Effects of Chemical Substitution on the Properties of $Bi_{1-x}RE_xFeO_3$, $BiFe_{1-x}Mn_xO_3$ and $Bi_{1-x}AE_xFeO_{3-x/2}$

- $Bi_{1-x}RE_xFeO_3$

The introduction of rare-earth ions (RE) in BFO can result in the partial destruction of its magnetic cycloid and the formation of a mixed (cycloidal + canted) antiferromagnetic structure [90,91].

Structural investigations of $Bi_{1-x}RE_xFeO_3$ solid solutions have revealed intriguing behaviors, such as the modulated phases found between the known ferroelectric $R3c$ state at low RE concentrations and the established nonpolar $Pnma$ phase at higher RE concentrations [92,93].

An interesting behavior in $Bi_{1-x}RE_xFeO_3$ is the significant decrease of the Curie temperature at which the $R3c$ state disappears in comparison to the relatively small dependency of the Néel temperature as the RE composition increases, potentially leading to the optimization of magnetoelectricity at certain concentrations (equalizing T_N and T_C) [94].

It is worth noting that for a fixed RE composition, the Curie temperature (T_C) decrease when the ionic radius of the rare-earth element is reduced. This dependence on the ionic radius may offer an additional means of controlling the structural, electric, and magnetic properties of $Bi_{1-x}RE_xFeO_3$ systems [95].

- $Bi_{1-x}AE_xFeO_{3-x/2}$

AE-substituted $BiFeO_3$ can show weak ferromagnetism in the polar phase [96]. The variation in oxidation states between AE^{2+} and Bi^{3+} leads to the creation of oxygen vacancies to maintain the stable valence of Fe^{3+} [97]. The presence of anion vacancies has been shown to significantly impact the magnetic structure, causing a disruption in the cycloidal magnetic modulation in the $R3c$ phase [98, 99]. However, the introduction of lattice defects through doping is not the only factor that determines the evolution of magnetic properties in the $Bi_{1-x}AE_xFeO_{3-x/2}$ series. The size of the alkali-earth substituent also plays a important role (specifically, the spontaneous magnetization decreases as the ionic radius of the AE^{2+} ion increases) [100]. Diffraction studies have shown that the replacement of bismuth ions with Sr^{2+} and Ba^{2+} ions (which have ionic radii significantly larger than that of Bi^{3+}) [101] leads to a structural transformation to a pseudo-cubic structure [100, 102] or to tetragonal phase [103] at $x \sim 0.20$. Replacement of Bi^{3+} ions with Ca^{2+} ions (which have a smaller ionic radius) results in a more intricate sequence of structural phase transitions, including the presence of an intermediate antipolar phase at $x \sim 0.10$ [96].

To produce complex-ordered perovskites in bismuth alkaline earth-based ferrites, there is a need to be mindful of the two main parameters of stoichiometry, while investigating the systems like $Bi_{1-x}AE_xFe^{3+}O_{3-x/2}$ (AE = Sr and Ca) with a fixed ratio of (Bi+AE)/Fe = 1 and a consistent valence state of iron (Fe^{3+}). This methodology encourages the stabilization of long-range ordering that is linked to oxygen stoichiometry [104].

- $BiFe_{1-x}Mn_xO_3$

Bismuth manganite ($BiMnO_3$) has a perovskite structure and a monoclinic distortion of its unit cell. Its magnetic transition temperature(T_C) is around 100 K, and the ferromagnetic state is caused

by orbital ordering of Mn^{3+} ions, which remain stable until around 475 K. The type of magnetic coupling in $BiMnO_3$ is influenced by the chemical bond lengths and angles, and can be modified through chemical doping or other methods. At temperatures above 770 K, there is a phase transition to an orthorhombic structure with the space group *Pnma* [105].

It has been observed that bismuth ferrite ($BiFeO_3$) and bismuth manganite ($BiMnO_3$) can form a solid solutions throughout their entire composition range if a high-pressure synthesis is being used [106].

The crystal structure of the $BiFe_{1-x}Mn_xO_3$ transforms from the polar rhombohedral, specific to the initial $BiFeO_3$, to an antipolar orthorhombic structure, and then to a monoclinic one ($BiMnO_3$) through stabilization of respective two-phase regions. The substitution of Mn^{3+} ions for Fe^{3+} ions in $BiFeO_3$ leads to a decrease in the magnetic transition temperature and a change in the magnetic state from antiferromagnetic to long-range ferromagnetic [107].

As a result, the magnetic structure of the $BiFe_{1-x}Mn_xO_3$ shifts from the G-type antiferromagnetic ($BiFeO_3$) with spiral modulation, to a ferromagnetic structure due to the ordering of Mn d_z^2 orbitals [108].

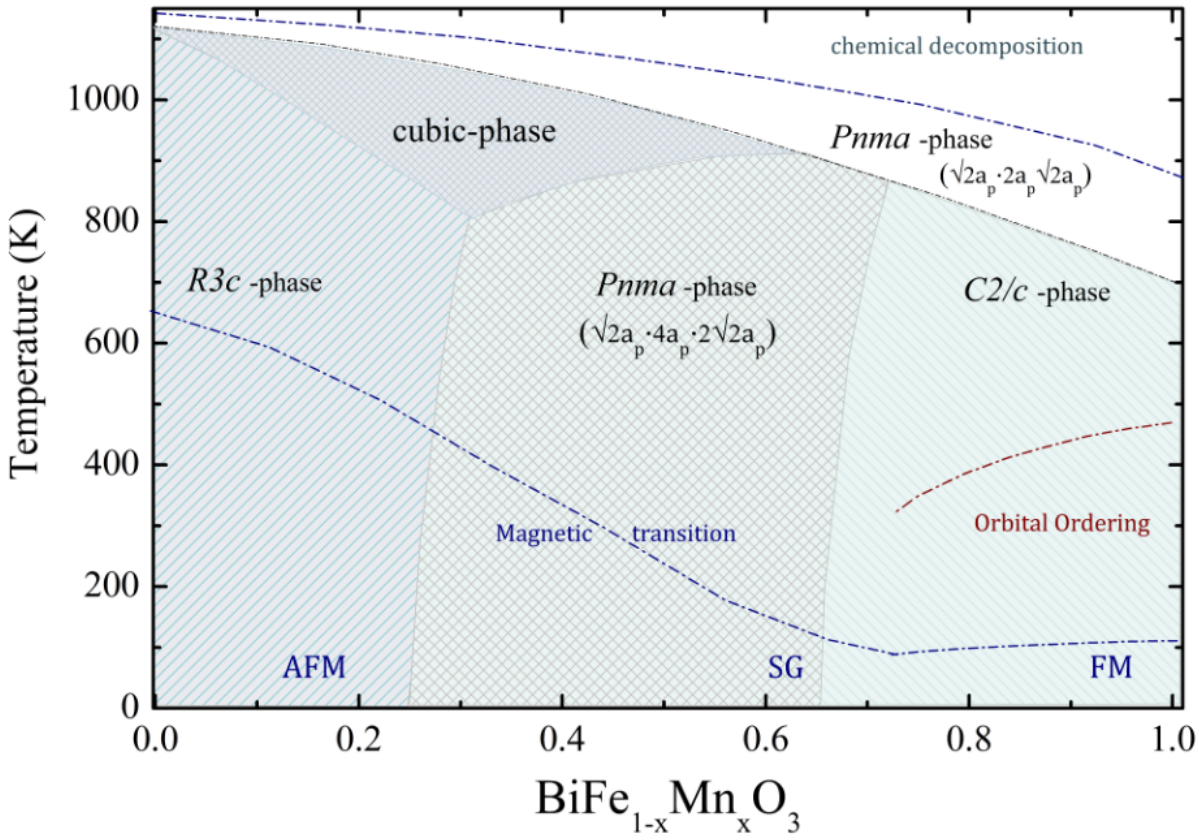

Fig. 13. Phase diagram of the $BiMnO_3$-$BiFeO_3$ solid solution, showing the relationship between temperature and chemical composition, with regards to the structural and magnetic properties [108].

We can see that an increase in dopant concentration leads to a transition from a rhombohedral to an orthorhombic structure, which disrupts the modulated antiferromagnetic structure and gives rise to a non-colinear antiferromagnetic structure accompanied by weak ferromagnetism [108].

Furthermore, in $Bi_{1-x}Ca_xFeO_{3-x/2}$, the concurrent substitution of Fe^{3+} with Mn^{4+} or Ti^{4+} ions

shifts the polar boundary (which occurs at x = 0.10) to larger values of x (x = 0.19 and x = 0.27 for the Ca/Mn and Ca/Ti series, respectively) [109].

To sum up, using bismuth substitution with alkali-earth or rare-earth elements, and/or iron substitution with transition metal ions like Mn, Ti or Nb, has been proven to be a useful method for adjusting the crystal structure and physical properties to enhance the multiferroic properties of $BiFeO_3$. However, despite many studies, a comprehensive understanding that would allow for forecasting the effects of "chemical substitution-induced pressure" on $BiFeO_3$ has not yet been established [96, 110, 111].

Overall, the doping of $BiFeO_3$ with various elements has been shown to be a promising method for controlling and modifying its crystal structure and physical properties, but further research is needed to fully understand and predict the behavior of these doped materials. In previous studies, attempts to induce spontaneous magnetization in the multiferroic material $BiFeO_3$ have focused on altering the magnetic anisotropy in order to suppress a cycloidal antiferromagnetic structure and promote a canted antiferromagnetic one. However, the maximum spontaneous magnetization attainable with this method is typically limited to around 0.3 emu/g [109, 112].

In this project, we propose to explore a different approach by using a doping method where some of the Fe^{3+} ions are replaced with manganese in mixed oxidation states, in order to create ferromagnetic exchange coupling (Mn^{3+}: $t_{2g}^3 e_g^1$–O–Mn^{4+}: $t_{2g}^3 e_g^0$). This approach would be implemented using the $Bi_{1-x}Ca_xFe_{1-y}Mn_yO_3$ system, where the charge imbalance caused by the replacement of Bi^{3+} with AE^{2+} ions is compensated by the presence of Mn^{4+} (which coexist with Mn^{3+} at y > x) [113].

2 Methodology

2.1 Sample preparation

Ceramic samples of $Bi_{1-x}Ca_xFe_{1-y}Mn_yO_3$ (x = 0.10, 0.15 and y = 0.35, 0.40, 0.45) were prepared via a conventional solid-state reaction method using Bi_2O_3, Fe_2O_3, Mn_2O_3, and $CaCO_3$ powders (with a purity of ≥99%) as starting materials. The reagents were thoroughly mixed in stoichiometric proportions. Subsequently, the resulting mixtures were shaped into pellets and annealed in alumina crucibles at 950°C for 20 hours under atmospheric conditions, followed by controlled cooling to room temperature at a rate of 100°C per hour.

The synthesis resulted in the formation of chemically uniform ceramic materials. Confirmation of their homogeneity was achieved through secondary electron microscopy and backscattered electron microscopy analysis performed with a VEGA-3 SBH (TESCAN) scanning electron microscope.

X-ray diffraction (XRD) data was obtained over a 2h span, ranging from 15° to 100° in increments of 0.01°, with an exposure time of 2 seconds per step. The measurements were conducted using a Bruker D8 Advance diffractometer equipped with Ni-filtered Cu K_α radiation. Subsequent analysis of the XRD patterns was performed utilizing the whole-pattern decomposition method, employing the FullProf software.

(a) TESCAN VEGA-3 SBH.

(b) Bruker D8 Advance.

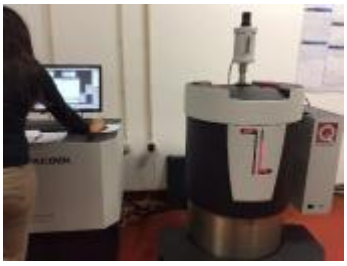

(c) Dynacool Quantum Design PPMS.

Fig. 14. (a) Scanning electron microscope, (b) X-ray powder diffractometer, (c) Physical properties measuring system.

Magnetic measurements were performed utilizing the Dynacool Quantum Design Physical Properties Measuring System (PPMS), which is equipped with a 9 T superconducting magnet and capable of operating within a temperature range from 1.8 K to 400 K. The PPMS DynaCool functions as a closed-cycle system, obviating the necessity for liquid cryogens. It employs a two-stage Pulse Tube cooler to produce the necessary liquid helium for cooling both the superconducting magnet and the sample chamber, thus maintaining a low-vibration setting required for precise measurements.

2.2 X-ray diffraction

X-ray diffraction (XRD) is a technique that allows for the determination of the crystal structure, symmetry, lattice parameters, lattice strain, phase composition, and grain orientation in crystalline materials, without causing any damage to the sample. It is particularly useful for studying polycrystalline materials [114].

X-rays are electromagnetic waves with high energy and wavelengths ranging from 10^{-3} to 10^{1} nanometers. There are several methods for generating X-rays, including sealed tubes, rotating anodes, and synchrotron radiation sources. Sealed tubes and rotating anodes, which are commonly used in laboratory equipment, work by heating a tungsten filament in a vacuum to generate electrons, which are then accelerated through a high potential field and directed towards a target. The impact of the electrons on the target causes two effects that lead to the generation of X-rays. First is the deceleration of the electrons, which leads to the emission of X-ray photons with a broad, continuous distribution of wavelengths known as Bremsstrahlung. Second is the emission of X-ray photons through the excitation and subsequent de-excitation of inner shell electrons in the target material [115].

When X-ray photons interact with matter, they can be absorbed or scattered in various ways. Elastic scattering, also known as Rayleigh scattering, occurs when X-ray photons are scattered by the electrons surrounding atomic nuclei. In this case, the energy of the scattered wave is unchanged and it retains its phase relationship with the incident wave. As a result, X-ray photons impinging on all atoms in an irradiated volume will be scattered in all directions. However, the periodic nature of crystalline structures can lead to constructive or destructive scattered radiation, resulting in characteristic diffraction patterns that can be used to study the crystal structure of materials [116, 117].

The principle of X-ray diffraction (XRD) is based on the diffraction of X-rays by periodic atomic planes and the detection of the diffracted signal at specific angles or energies. The geometric interpretation of XRD (constructive interference) was provided by W.L. Bragg [118]. Bragg's law is given in Equation 10 and depicted in Fig. 15.

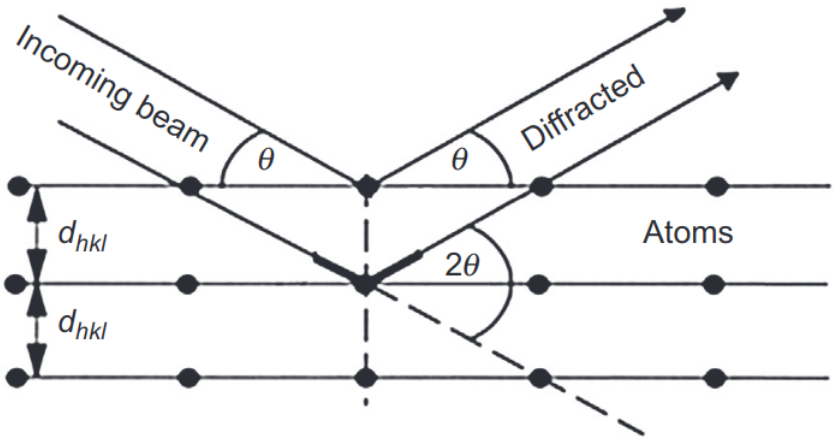

Fig. 15. Conditions required for diffraction to occur from lattice planes [119].

$$n\lambda = 2d_{hkl}\sin\theta, \tag{10}$$

where n is the order of diffraction, λ is the wavelength of the incident beam in nanometers, d_{hkl} is the lattice spacing in nanometers, and θ is the angle of the diffracted beam in degrees [118].

The intensity of diffraction by a unit cell is the sum of the intensities scattered by its individual atoms. The diffracted intensities, represented by $I_{(hkl)}$, are directly proportional to the square of the crystallographic structure factor $F_{(hkl)}$ [117].

$$F_{(hkl)} = \sum_{j=1}^{N} f_j \times e^{2\pi i(hx_j + ky_j + lz_j)}. \tag{11}$$

The crystallographic structure factor, $F_{(hkl)}$, is a sum over all atoms in a unit cell of the form factor or atomic scattering factor f_j, of each atom multiplied by a term involving the Miller indices hkl, of the diffracting planes and the relative atomic positions, x_j, y_j, z_j, in the unit cell. The summation j, runs over all atoms in the unit cell [120]. The intensity of the diffraction pattern produced by a lattice plane $I_{(hkl)}$ is influenced by various factors, which can be combined to produce an equation that describes the intensity at any 2θ position:

$$I_{(hkl)} = K \times |F_{(hkl)}|^2 \times f_a e^{\frac{-B\cdot\sin^2(\theta)}{\lambda^2}} \times A \times L(\theta) \times P(\theta) \times m, \tag{12}$$

where K is a constant independent from 2θ, $f_a e^{\frac{-B\cdot\sin^2(\theta)}{\lambda^2}}$ temperature factor which is a measure of the average deviation of atoms from their mean positions due to thermal motion, A absorption factor, m is a multiplicity describing number of equivalent planes that can diffract at a given Bragg angle, $L(\theta)$ Lorentz factor which is:

$$L(\theta) = \frac{1}{\sin(2\theta)} \tag{13}$$

and $P(\theta)$ polarization factor described as:

$$P(\theta) = \frac{1 + \cos^2(2\theta)}{2} \tag{14}$$

[117]. Diffraction data is typically represented as an intensity distribution plotted as a function of the 2θ angle. The amount of information that can be obtained from this data is represented by the intensity at each angle, see Fig. 16 [119].

The intensity of a diffraction peak, its position, width, and the amount of information it contains can be characterized and measured in various ways. The transmitted intensity of X-rays through a material is reduced due to absorption and scattering, following an exponential relationship described by the Beer-Lambert law:

$$I = I_0 \times \exp(-\mu \times x), \tag{15}$$

where I transmitted intensity, μ the mass absorption coefficient which is a measure of how effectively a material absorbs X-rays, depends on both the wavelength of the X-rays and the properties of the material, the thickness of the absorbing layer is represented by x [121].

A goniometer is a device that is present in all laboratory equipment and is a crucial component

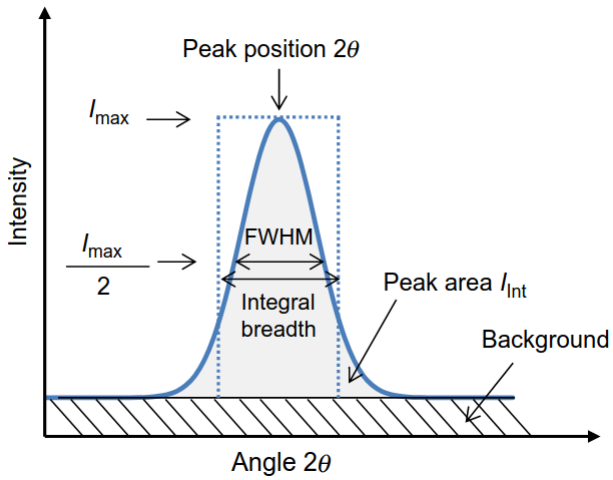

Fig. 16. The intensity of the diffraction peaks and the amount of information that can be extracted from them [119].

of a diffractometer. It allows for precise movement of the X-ray source, the sample, and the detector relative to one another.

There are two main types of goniometers that are commonly used: θ/θ goniometers, in which the sample is fixed and the X-ray source with detector move, and $\theta/2\theta$ goniometers, in which the X-ray source is fixed and the sample and detector move.

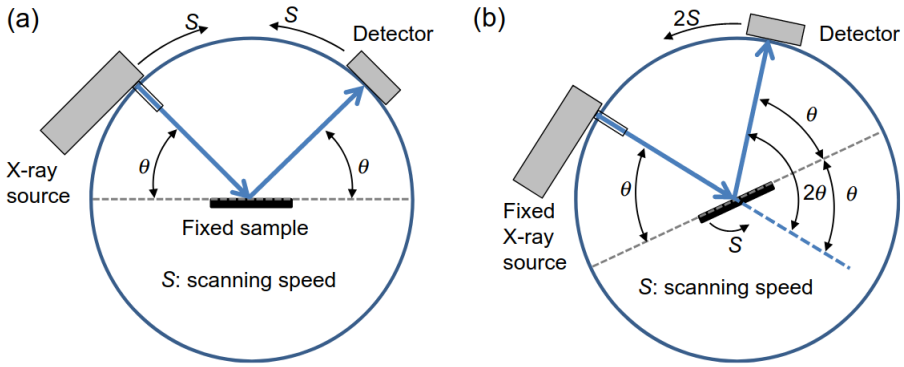

Fig. 17. The principle of θ/θ goniometers is shown in (a), while the principle of $\theta/2\theta$ goniometers is shown in (b) [122].

Depending on the shape of the sample and the goals of the measurement, specific sample holders or a controlled sample environment can be employed. These may include features such as automatic sample positioning, automatic sample changing, continuous sample rotation or translation.

2.3 Scanning electron microscopy

A scanning electron microscope (SEM) is an instrument that creates images of a sample by using a focused beam of electrons to scan the surface of the sample. The electrons interact with the atoms in the sample, producing signals that contain information about the surface features and composition of the sample. This information is used to create an image of the sample. SEMs can achieve high resolutions, sometimes better than 1 nanometer, and are useful for studying a variety of samples. The most common way to operate an SEM is to use a secondary electron detector to measure the secondary electrons emitted by atoms that have been excited by the electron beam. The intensity of the detected signal depends on the topography of the sample and other factors [123].

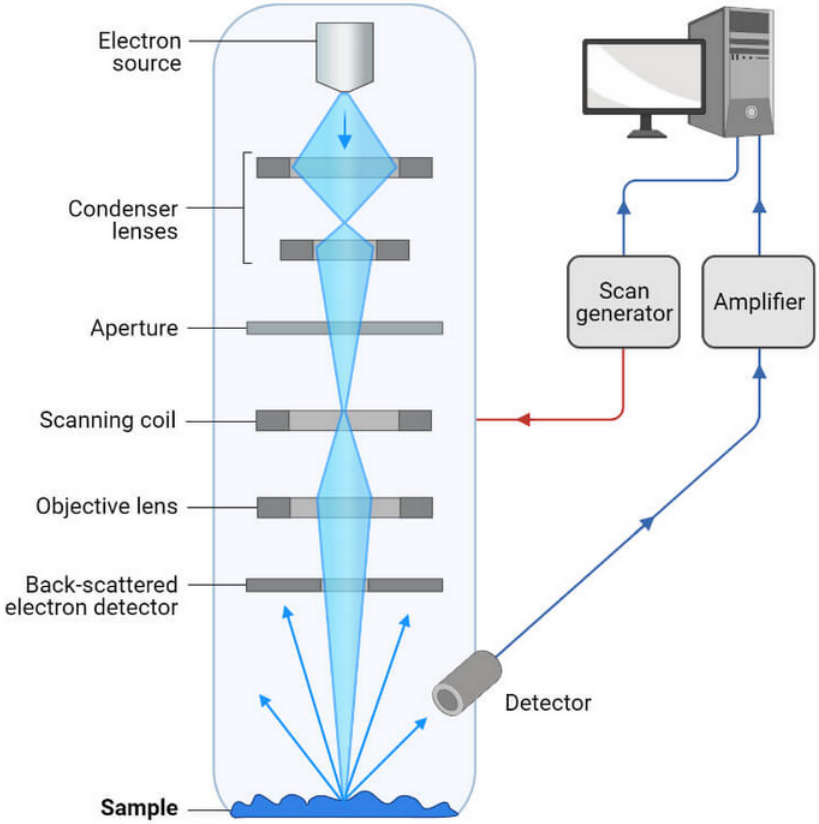

Fig. 18. Schematic diagram of a scanning electron microscope (SEM) showing the key components [124].

Several factors can affect the interaction volume and scattering of electrons in a sample during analysis with a scanning electron microscope (SEM). These include the atomic number and concentration of atoms in the sample, the incoming electron energy (accelerating voltage), and the angle of incidence of the electron beam. Increasing the electron energy or angle of incidence can increase the interaction volume and scattering, while a high atomic number or concentration of atoms can decrease it. Materials with a higher atomic number absorb or stop more electrons and produce a smaller interaction volume, while higher voltages generate high-energy electrons that penetrate deeper into the sample and create a larger interaction volume [125].

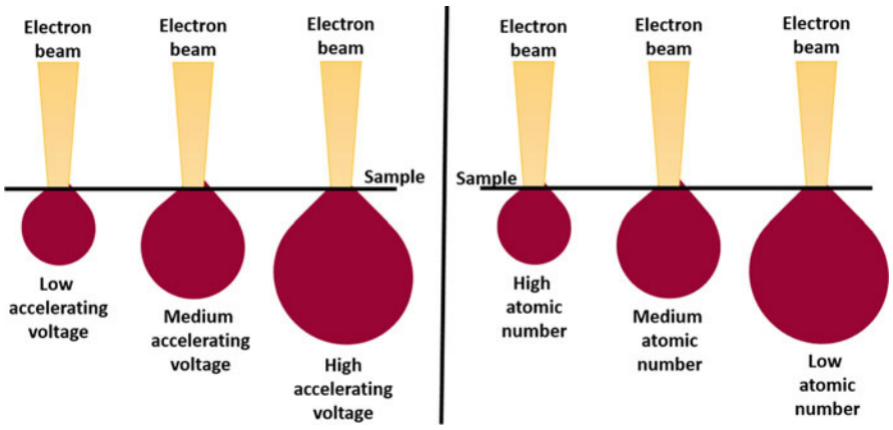

Fig. 19. Dependence of interaction volume and penetration depth on the accelerating voltage of the electron beam and atomic number of the sample [125].

When an incoming electron interacts with the nucleus and electrons of a specimen through the Coulomb field, a variety of signals may be emitted, such as secondary electrons, backscattered electrons, X-rays (used for elemental analysis), and visible light (cathodoluminescence). These signals are collected by detectors and processed by a computer to produce the desired image [126].

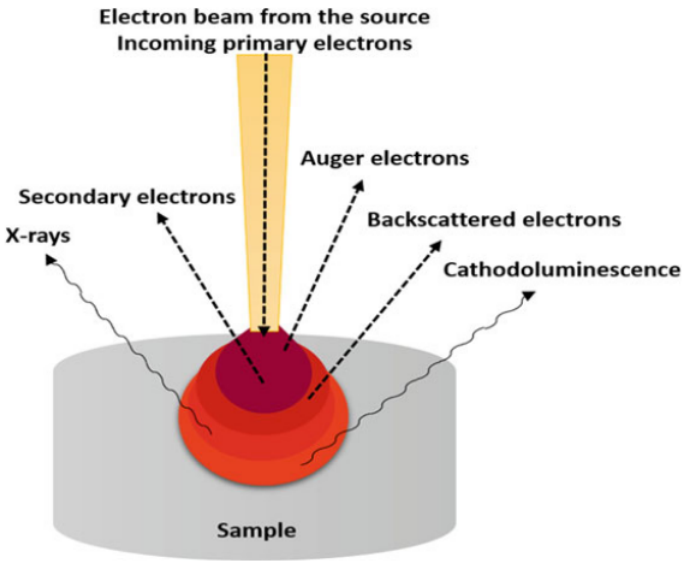

Fig. 20. The interaction between an electron beam and a specimen, and the resulting signal emitted from the sample [125].

SEM images are typically created using backscattered and secondary electrons. Secondary electrons are considered the most important for showing sample morphology and topography, while backscattered electrons are used to show contrast in the composition of multiphase samples. X-rays are also generated through the interaction of the incident electron beam with the sample atoms, causing the excitation of the electrons to higher energy levels. When these electrons return to lower energy levels, they emit X-rays with a specific wavelength that is characteristic of the element. SEM is non-destructive, as the X-ray generation process does not result in any loss of material, allowing the same sample to be analyzed repeatedly [125].

2.4 Vibrating sample magnetometry

The Vibrating Sample Magnetometer (VSM) is a tool used to measure the magnetic moment of a sample. It works by vibrating the sample perpendicular to a uniform magnetizing field and detecting changes in the sample's magnetic moment as small as $10^{-5}$to 10^{-6} emu. This technique is based on Faraday's law of magnetic induction and can be used to obtain detailed information about the magnetic properties of a sample [127].

The sensitivity of the Vibrating Sample Magnetometer (VSM) is limited by the signal-to-noise ratio at the input circuit, where noise is any signal not caused by the sample's magnetic moment. The primary sources of noise are the Johnson noise of the wire used for the pickup coils and the magnetic properties of the sample holder, which can add an in-phase signal to the desired signal. The small magnetic contribution of the sample holder can be corrected for by taking measurements with the sample removed [127].

Sample is placed on a sample holder and positioned between the poles of an electromagnet. The sample can be oriented either horizontally or vertically, depending on the type of measurement being performed. There are several types of sample holders that can be used, including those that allow for measurements to be taken in the plane of the sample and those that allow for measurements to be taken out of the plane of the sample [128].

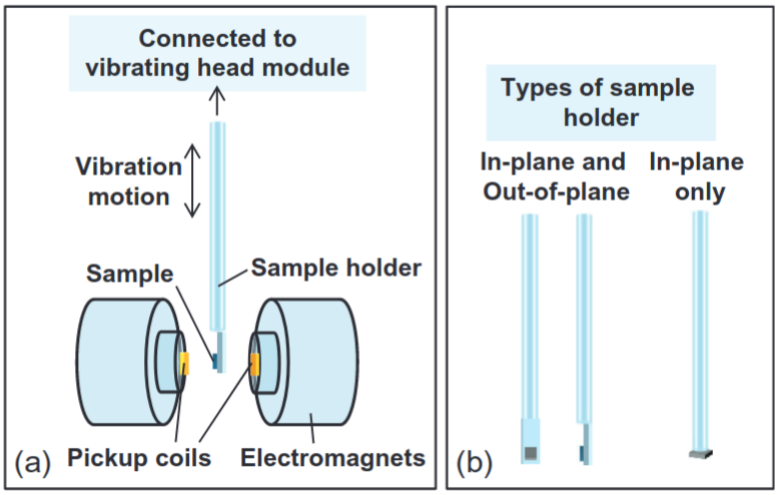

Fig. 21. a) Schematic diagram of the VSM setup. b) Illustrates the different types of sample holders that can be used in VSM [128].

Before measurements are taken with the Vibrating Sample Magnetometer (VSM), the optimal position for the sample, known as the "saddle point," must be determined through positioning calibration. During the measurement process, the sample is vibrated vertically at a fixed frequency ω. Changes in the magnetic flux, which are proportional to the magnetic moment of the sample, cause an alternating current (AC) voltage to be induced in pickup coils located near the electromagnet poles. This voltage is used to determine the magnetic moment of the sample by feeding it into a lock-in amplifier. Flux changes can be detected by altering the applied magnetic field, the position of the coils, or the position of the sample [127].

3 Results and discussion

3.1 X-ray diffraction

The X-ray diffraction patterns of $Bi_{1-x}Ca_xFe_{1-y}Mn_yO_3$ (x = 0.10, 0.15 y = 0.35, 0.40, 0.45) were investigated at room temperature. Analysis was conducted within a trigonal crystal system, employing unit cell parameters $a = \sqrt{2}a_p$ and $c = 2\sqrt{3}c_p$, where a_p and c_p represent the parameters of the primitive pseudocubic perovskite subcell. The results revealed consistency with the space group $R3c$ for y $\leq$ 0.40.

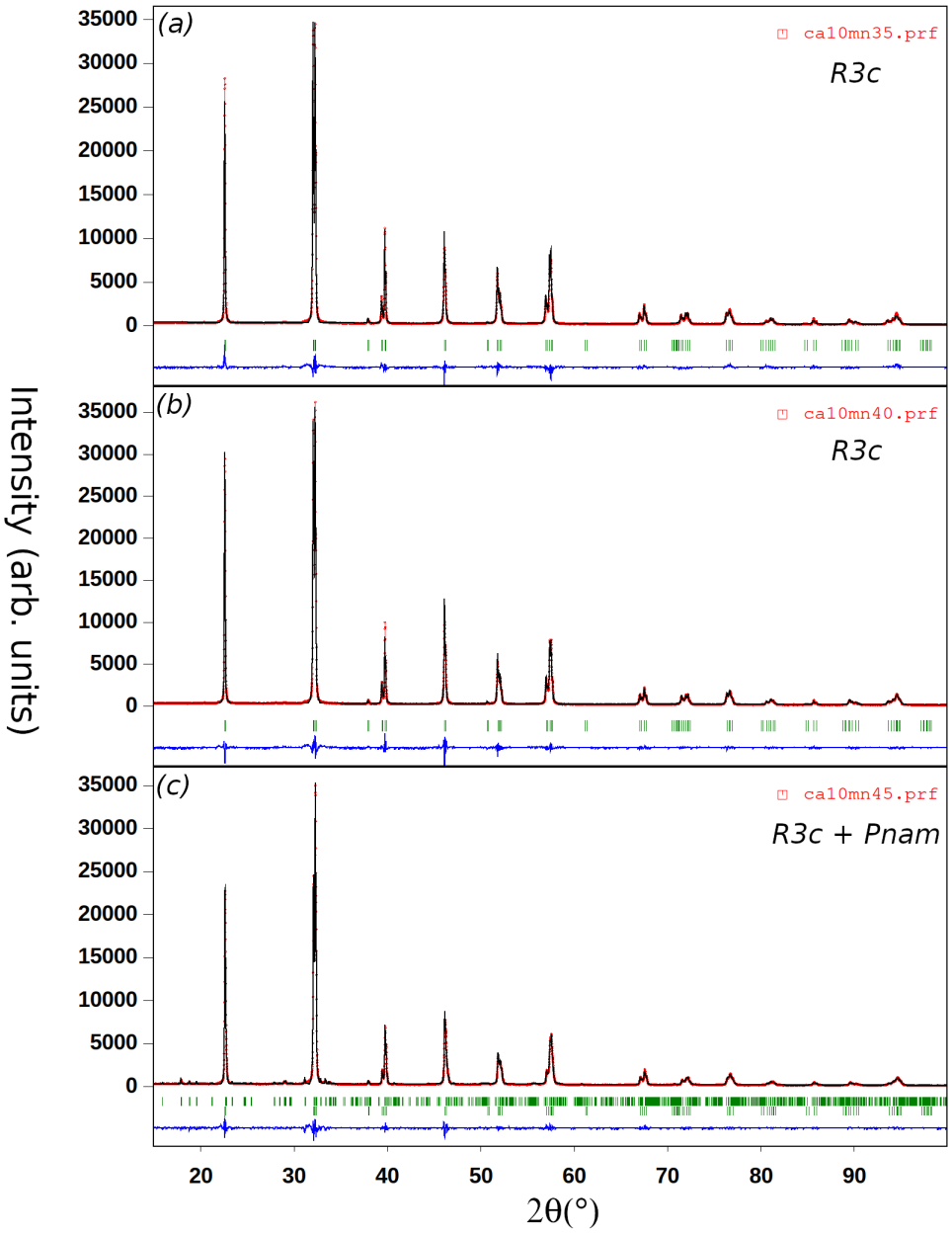

Fig. 22. Results obtained from X-ray diffraction (XRD) analysis for the $Bi_{0.90}Ca_{0.10}Fe_{1-y}Mn_yO_3$ samples with y = 0.35 (a), 0.40 (b), and 0.45 (c) at room temperature.

The associated structural distortions, as delineated in reference to the cubic perovskite ABO_3, can be expressed by the superposition of an alternating clockwise/counterclockwise tilting of the BO_6 octahedra along the threefold pseudocubic axis (tilt system $a^-a^-a^-$) accompanied by polar atomic displacements along the same axis (otherwise the structure would belong to space group $R-3c$) [129]. An additional increase of the Mn concentration (Fig. 22) in perovskite system $Bi_{1-x}Ca_xFe_{1-y}Mn_yO_3$, where x = 0.10, leads to the emergence of the antipolar orthorhombic phase (space group *Pnam*) unique to the $BiFe_{1-x}Mn_xO_3$ perovskites, where $0.25 < x < 0.65$ [108].

Indeed, the X-ray diffraction pattern shown in Fig. 22 (c) demonstrated additional reflections that diverge from the anticipated *R*3*c* structure for the y = 0.45 sample. Rietveld profile refinement analysis, incorporating the *Pnam* space group confirms the coexistance of *R*3*c* and *Pnam* phases, with a transition from the polar *R*3*c* to the antipolar *Pnam* configuration at y = 0.45 (Table 1). This finding aligns with earlier studies that similarly emphasize the antipolar attributes at y = 0.50, where no evidence of the rhombohedral phase was detected in the compound. [130].

y	Space Group	a (Å)	b (Å)	c (Å)
0.35	*R*3*c*	5.5459(4)	5.5459(4)	13.7197(5)
0.40	*R*3*c*	5.5446(4)	5.5446(4)	13.7087(5)
0.45	*Pnam*	5.5294(2)	11.1377(8)	15.6238(9)
	*R*3*c*	5.5446(4)	5.5446(4)	13.7083(6)

Table 1. The refined lattice parameters obtained from the analysis for $Bi_{0.90}Ca_{0.10}Fe_{1-y}Mn_yO_3$.

A structural phase transition has been observed in pure $BiFeO_3$ when subjected to applied pressure [131]. This transition appears to manifest under both internal and external pressure conditions, suggesting a broader trend toward polar–antipolar instability in $BiFeO_3$ as the unit cell experiences compression. The rhombohedral–orthorhombic transition is thought to be influenced by the complex interplay of structural distortions, driven by the stereochemically active $6s^2$ lone pair of the Bi^{3+} ions, and rotations of the $\langle Fe/Mn\rangle O_6$ octahedra, particularly under compression [107, 131, 132].

y	Space Group	a (Å)	b (Å)	c (Å)
0.35	*R*3*c*	5.5330(2)	5.5330(2)	13.6578(8)
0.40	*R*3*c*	5.5330(2)	5.5330(2)	13.6561(6)
0.45	*Pnma*	5.5570(3)	7.8023(4)	5.4619(3)

Table 2. The refined lattice parameters obtained from the analysis for $Bi_{0.85}Ca_{0.15}Fe_{1-y}Mn_yO_3$.

Furthermore, in the $Bi_{0.85}Ca_{0.15}Fe_{1-y}Mn_yO_3$ series, the introduction of Mn doping maintains the rhombohedral *R*3*c* structure at concentrations corresponding to $y = 0.35$ and 0.40, as illustrated in Fig. 23, further increase in Mn concentration stabilizes the nonpolar orthorhombic *Pnma* structure at $x = 0.45$, reminiscent of the paraelectric phase of $BiFeO_3$ [133] and the room-temperature phase of $CaMnO_3$ [134]. Similar perovskite compounds $Bi_{1-x}Ca_xFeO_{3-x/2}$ are renowned for pre-

serving the polar $R3c$ structure within a narrow concentration range of $0 \leq x \leq 0.1$ [96]. The formation of oxygen vacancies, arising from the heterovalent substitution of Bi^{3+} by Ca^{2+}, contributes to the elimination of polar order [130]. The incorporation of Mn^{4+} via simultaneous substitution not only eliminates oxygen vacancies in the lattice of $Bi_{1-x}Ca_xFe_{1-y}Mn_yO_3$ samples but also expands the compositional range of the ferroelectric phase up to $x = 0.19$. Furthermore, structural alteration is observed at the same critical value, resulting in the coexistence of the $R3c$ and $Pnma$ phases [109].

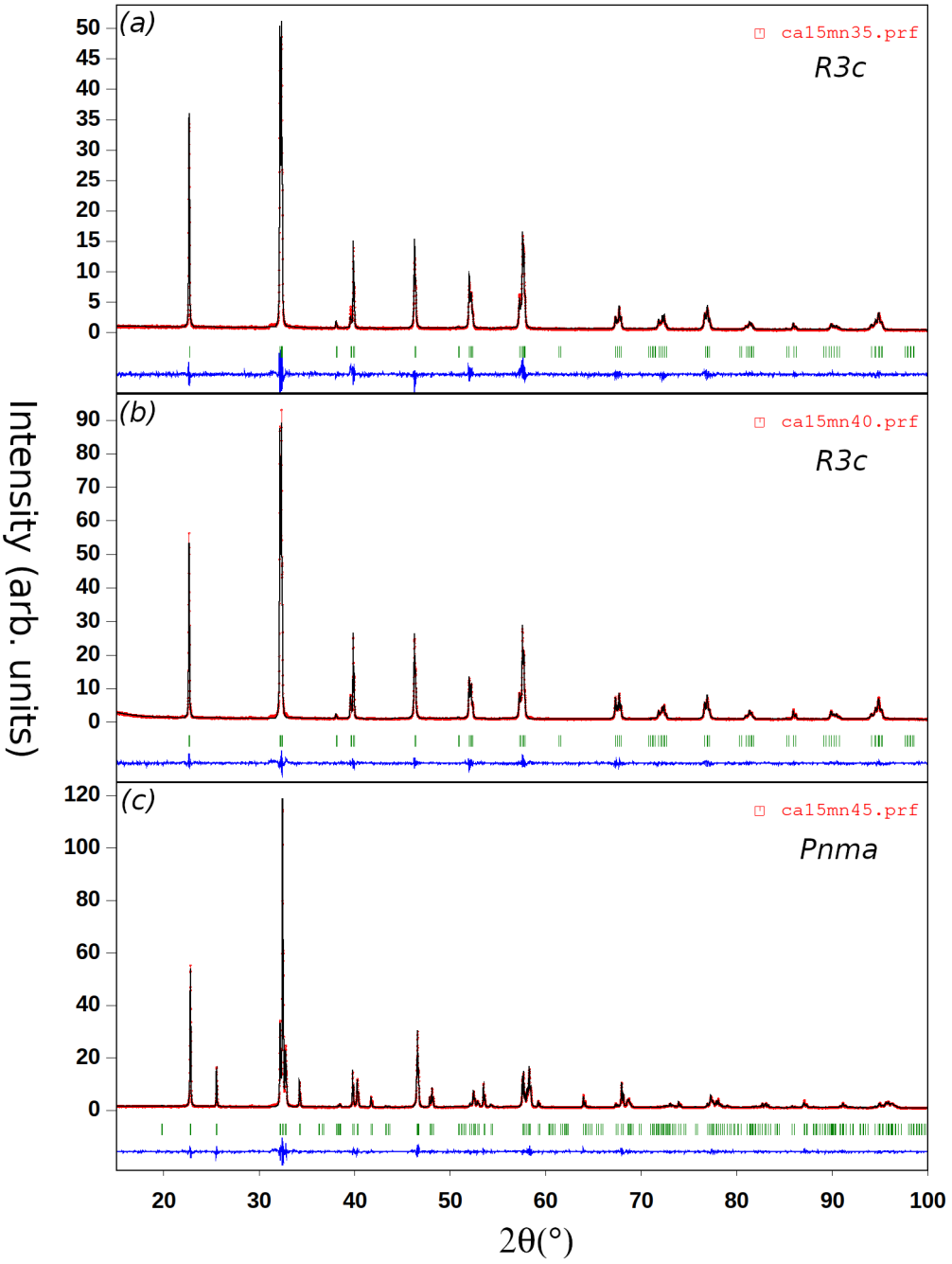

Fig. 23. Results obtained from X-ray diffraction (XRD) analysis of $Bi_{0.90}Ca_{0.15}Fe_{1-x}Mn_xO_3$ [with $x = 0.35$ (a), 0.40 (b), and 0.45 (c)] at room temperature.

However, no phase coexistence in $Bi_{1-x}Ca_xFe_{1-y}Mn_yO_3$ is observed for the $x = 0.15$ samples, as shown in Fig. 23. This absence suggests assumption that coexisting phase ($R3c + Pnma$) occurs within the range $0.15 < x \leq 0.19$. Furthermore, the crystal structure of the $Bi_{0.85}Ca_{0.15}Fe_{1-y}Mn_yO_3$ solid solution does not follow the trend toward the formation of an intermediate antipolar phase. Instead, this system undergoes a polar to nonpolar phase transition ($R3c \rightarrow Pnma$) within the range of $0.40 < x \leq 0.45$. The nonpolar $Pnma$ structure, akin to that found in $CaMnO_3$ [134], is observed at the upper threshold of this transition range.

In contrast, antipolar structure appears to be typical of the intermediate phase that separates the polar antiferromagnetic $R3c$ and nonpolar ferromagnetic $C2/c$ phases in the $BiFe_{1-x}Mn_xO_3$ system [135]. Additionally, it is noteworthy that in $Bi_{1-x}Ca_xFe_{1-y}Mn_yO_3$ at $x = 0.10$ and y = 0.45, an intermediate phase ($R3c + Pnam$) observed is different than at x = 0.15, suggesting that further increase in x leads to different transition: from polar-antipolar $|R3c \rightarrow Pnam|$ to polar-nonpolar $|R3c \rightarrow Pnma|$ as seen in Fig. 22, 23.

3.2 Scanning electron microscopy

The SEM images at 20 μm and 100 μm scales provide valuable insights into the surface properties of the samples. The former unveils intricate details and microstructures, where as the latter offers a broader view, capturing macroscopic features. Through SEM image analysis, distinct grain boundaries emerge, indicating variations in grain size and the presence of diverse crystalline domains within the sample. These boundaries provide valuable information about the material's microstructure, revealing the arrangement and interaction of individual grains. Additionally, the observed grain boundaries indicates the likelihood of crystalline defects. Furthermore, the magnetic properties of $BiFeO_3$ based multiferroics can be significantly influenced by the presence of ferromagnetic or ferrimagnetic impurities.

Although XRD measurements did not detect any traces of impurity phases in the samples under investigation, their uniform purity were further confirmed using scanning electron microscopy (SEM) techniques. A comparison between secondary electron microscopy images, providing information on the sample surface topography, and backscattered electron microscopy images, which are highly sensitive to the atomic number of the elements composing the phase, enabled the identification of different phases at the submicrometer level, revealing no composition-dependent variations in the image contrast. This observation further supports that the synthesis process yielded chemically uniform and homogeneous ceramic materials.

As mentioned in [136, 137], it is scientifically intriguing to note that the substitution of Fe by Mn within the $Bi_{1-x}R_xFe_{1-y}Mn_yO_3$ series does not induce any significant increase in grain size.

On the other hand, the initial findings observed in [108, 130] indicate a consistent pattern of increasing average grain size with rising Mn concentration within the $Bi_{1-x}Ca_xFe_{1-y}Mn_yO_3$ perovskite series, where $x = 0.10$ and 0.15. The grain size ranges from a few micrometers for the sample with $y = 0.10$ to several tens of micrometers for the samples with $y = 0.40$, 0.45 and 0.50.

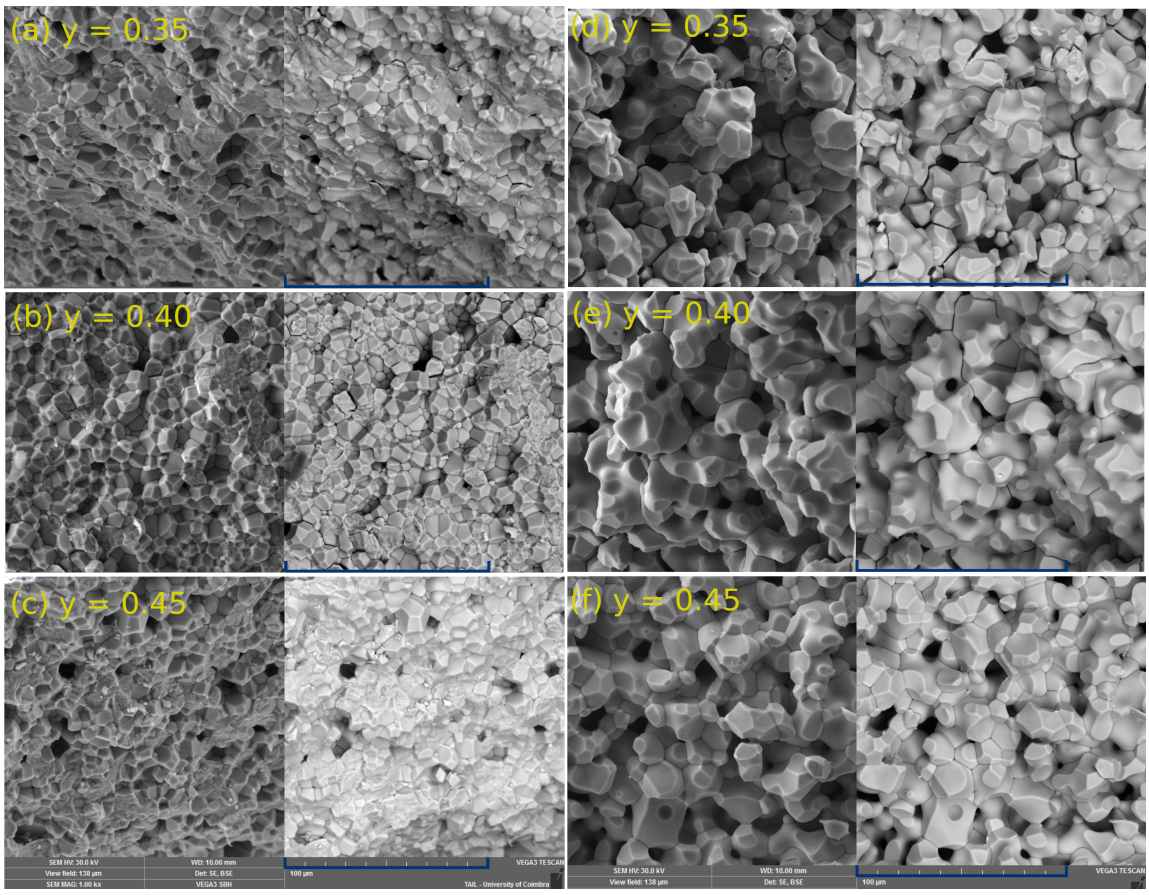

Fig. 24. SEM images were captured for $Bi_{1-x}Ca_xFe_{1-y}Mn_yO_3$ ceramics at x = 0.10 (a), (b), (c) and x = 0.15 (d), (e), (f) under both secondary electron (left column) and backscattered electron (right column) modes. The scale bar measures 100 μm.

As depicted in Fig. 24, the impact on grain size resulting from the substitution of Fe with Mn, particularly for ($0.35 \leq y \leq 0.45$) appears comparatively diminished in contrast to the effects of Bi substitution with Ca, specifically for $x = 0.10, 0.15$. This observation suggests the involvement of intricate mechanisms where the dependence in grain size from both x and y is delineated. The proposition arises that there exists a saturation threshold, where the influence of Ca on grain size surpasses that of Mn, upon reaching this threshold, the influence of Mn predominates, resulting in approximately a tenfold increase ($0.10 \leq y \leq 0.35$) in grain size. For clarity, the primary consequence of the increase in Ca content is the elevation of Mn^{4+} concentration. Mn^{4+} possesses a significantly smaller ionic radius compared to Fe^{3+} and Mn^{3+}, which can facilitate Mn diffusion and promote further crystal grain growth. Moreover, Ca demonstrates a approximately threefold decrease in magnitude of influence for grain size at $x = 0.10, 0.15$ ($0.35 \leq y \leq 0.45$) compared to the influence exerted by Mn at compositional range of $x = 0.10, 0.15$ ($0.10 \leq y \leq 0.35$) in $Bi_{1-x}Ca_xFe_{1-y}Mn_yO_3$ perovskite system.

Moreover, the SEM image depicted in Fig. 24 (c) illustrates slightly less distinct grain boundaries and an increase in grain defects, suggesting the sample brittleness nature compared to others in the series. This observation could be explained by the XRD Rietveld profile refinement analysis presented in Fig. 22 (c), which identifies two coexisting phases ($R3c + Pnam$) in this specific sample. The presence of these phases may instigate competition within the homogeneous sample

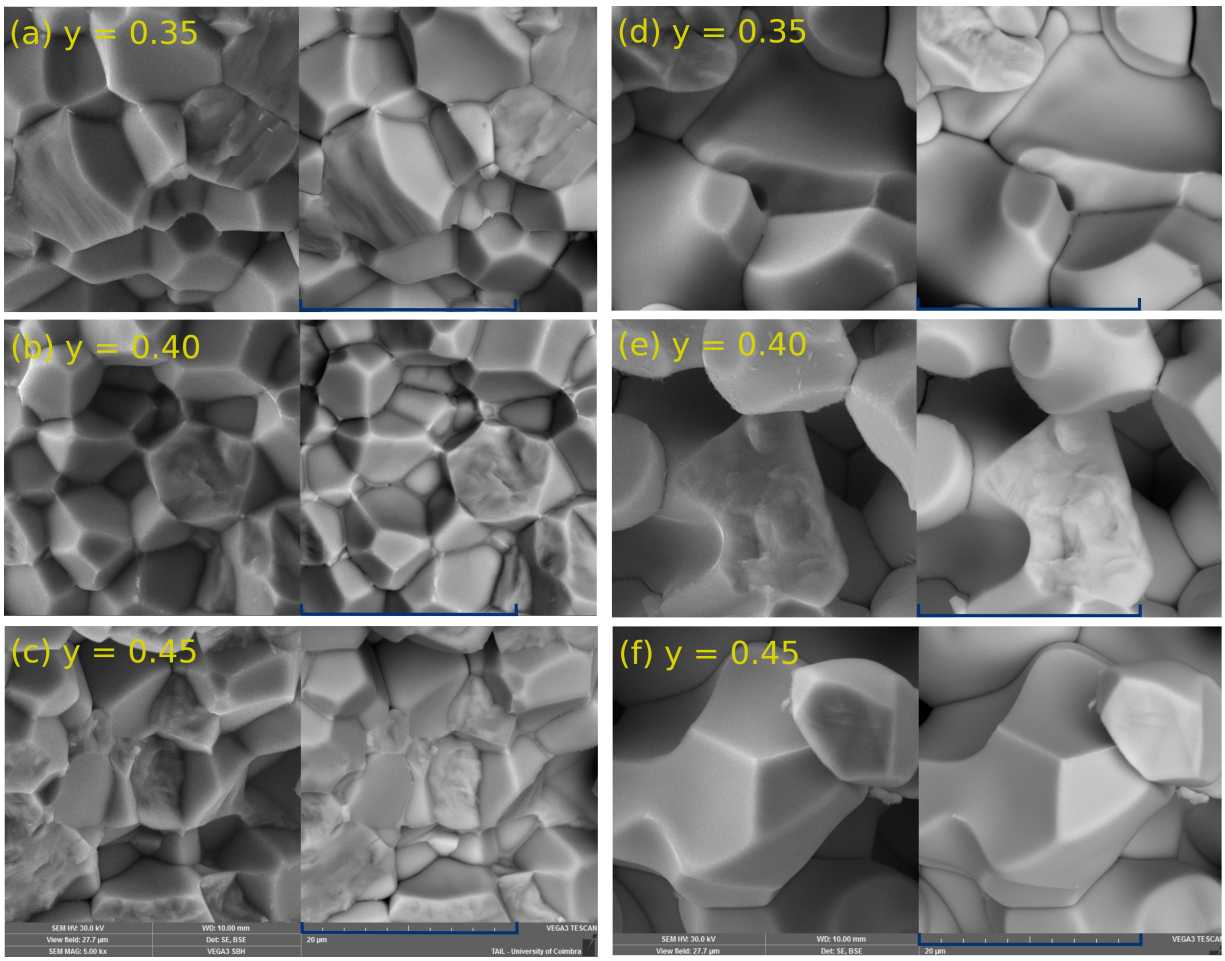

Fig. 25. SEM images were captured for $Bi_{1-x}Ca_xFe_{1-y}Mn_yO_3$ ceramics at x = 0.10 (a), (b), (c) and x = 0.15 (d), (e), (f) under both secondary electron (left column) and backscattered electron (right column) modes. The scale bar measures 20 μm.

grains, there by inducing internal strain forces within the grains and resulting in material brittleness. Further investigation is imperative to validate this hypothesis within the range $0.15 < x < 0.19$, as it is assumed that different phases coexistence of ($R3c + Pnma$) might be observed.

3.3 Vibrating sample magnetomery

To explore the magnetic state attributes of $Bi_{1-x}Ca_xFe_{1-y}Mn_yO_3$ samples near the juncture of polar/antipolar and polar/nonpolar phases, we conducted temperature-dependent magnetization measurements utilizing zero field cooling (ZFC), field-cooled cooling (FCC), and field-cooled warming (FCW) modes (Fig. 26). Examination of the $M(T)$ dependencies reveals that samples experience a transition from a paramagnetic to a magnetically ordered state at temperatures (Fig. 27) ranging from 383 K to 268 K.

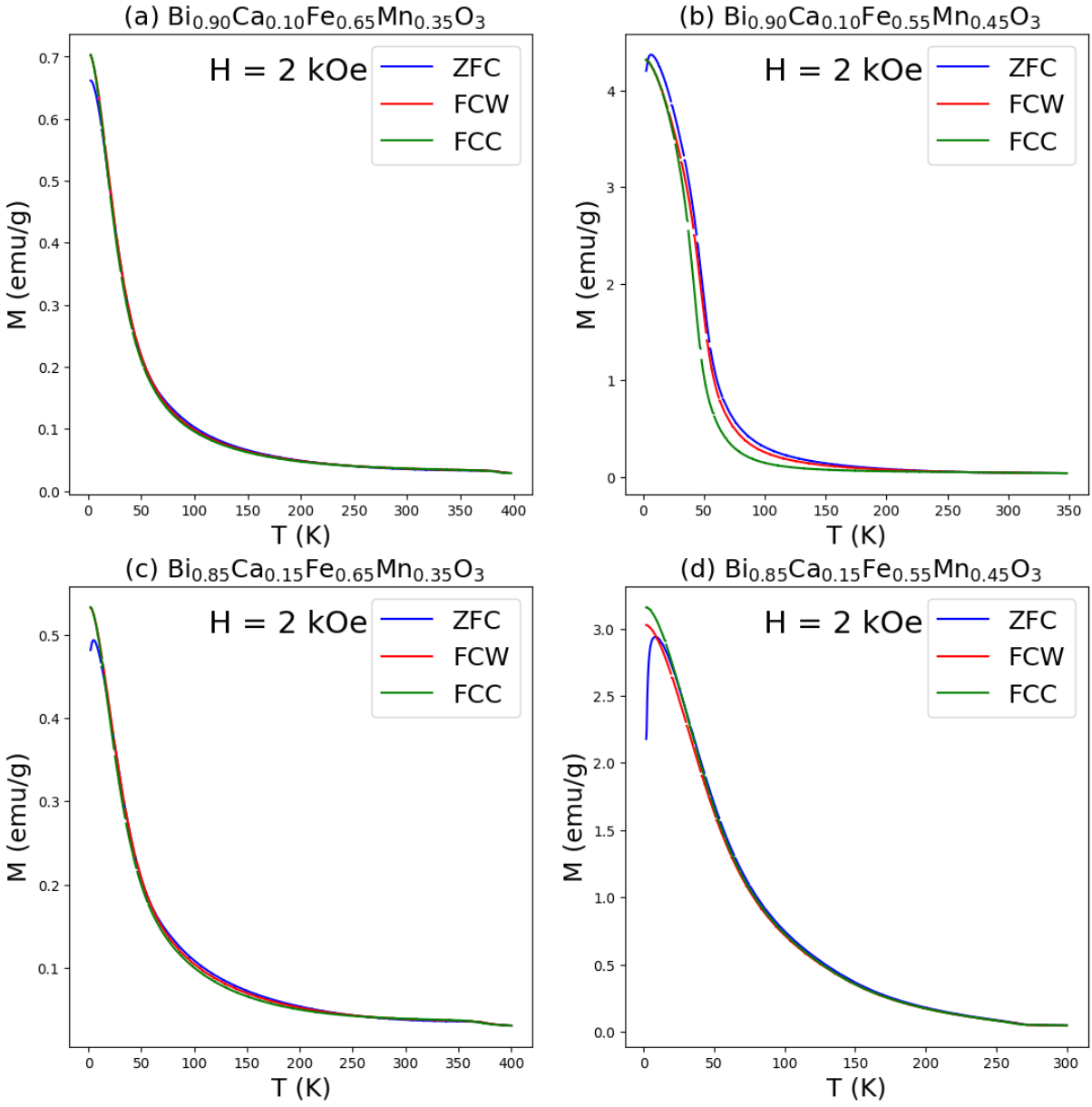

Fig. 26. The variations in magnetization with temperature were assessed for samples in perovskite system $Bi_{1-x}Ca_xFe_{1-y}Mn_yO_3$ using an applied field of H = 2 kOe, the experiments were conducted in zero field cooling (ZFC), field-cooled warming (FCW) and field-cooled cooling (FCC) modes.

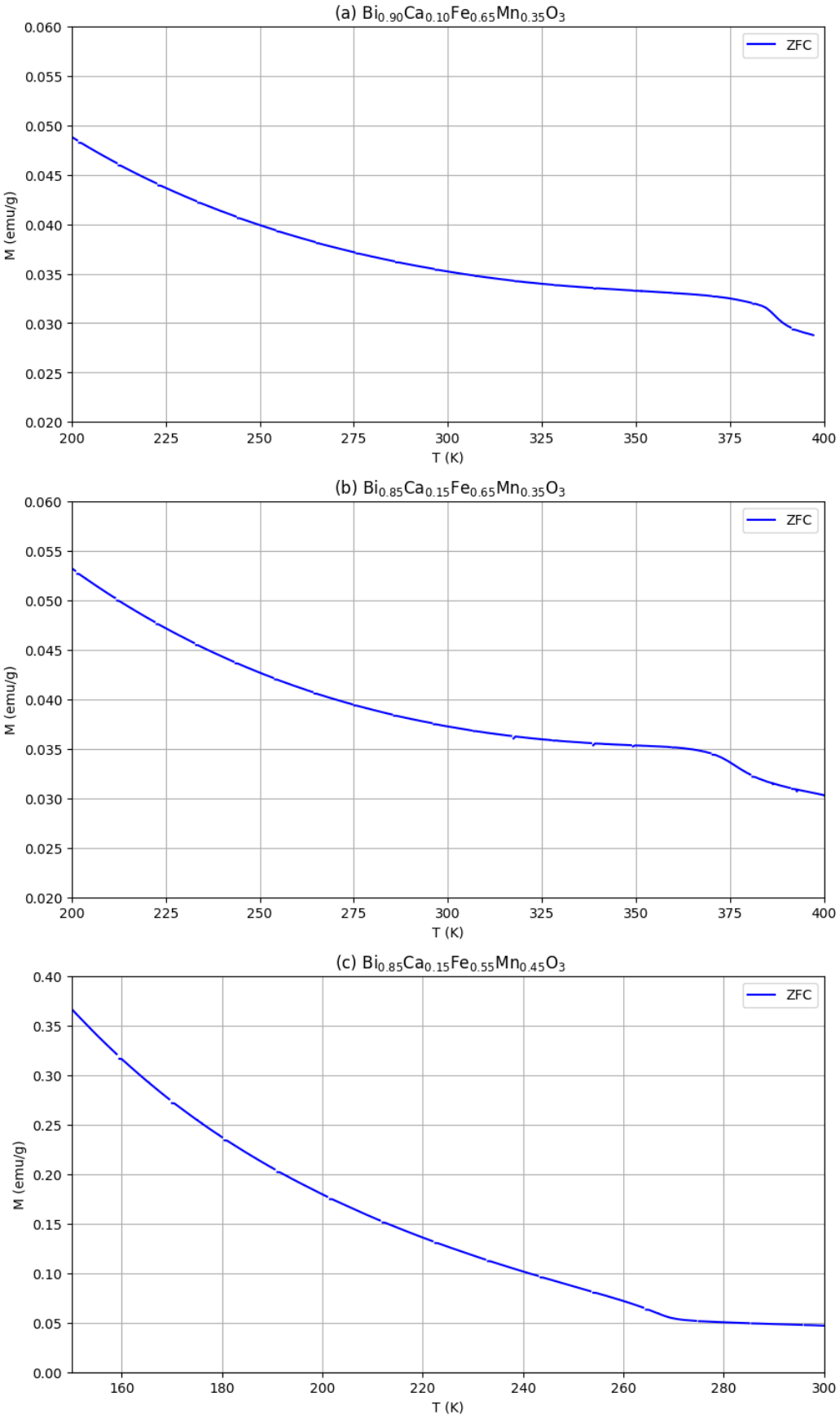

Fig. 27. The $M(T)$ dependencies observed for the samples in $Bi_{1-x}Ca_xFe_{1-y}Mn_yO_3$ perovskite system near Néel temperature points of 383 K (a), 369 K (b) , and 268 K (c) These dependencies were acquired following zero field cooling cycles under an applied magnetic field of H = 2 kOe.

The Néel temperatures, identified as the inflection points of the $M(T)$ curves, closely align with those characteristic of the $Bi_{0.85}Sr_{0.15}Fe_{1-y}Mn_yO_3$ [138] compounds with matching Mn (y = 0.35) concentrations, thus suggesting that manganese (Mn) exerts a predominant influence over the Néel temperature in comparison to alkali-earth (AE) substitution. This suggestion gains further reinforcement through observations in Fig. 27, where the impact of calcium (Ca) is shown in contrast (a and b) with the influence of manganese (Mn) on the Néel temperature (b and c).

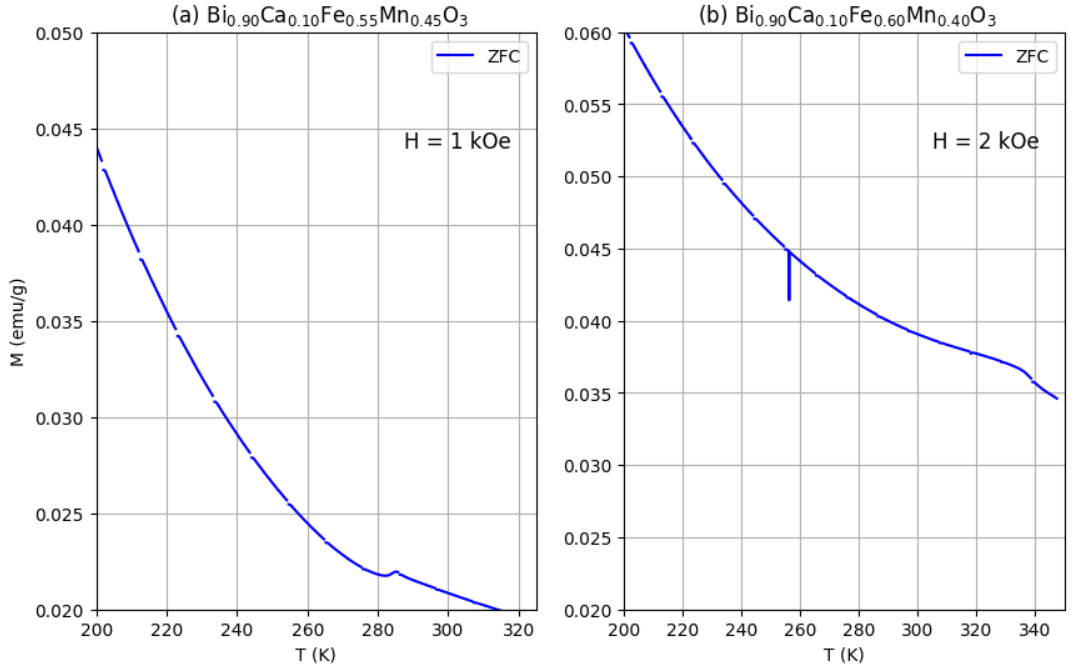

Fig. 28. The $M(T)$ dependencies observed for the samples in $Bi_{1-x}Ca_xFe_{1-y}Mn_yO_3$ perovskite system near Néel temperature points of 283K K (a) and 338 K (b). These dependencies were acquired following zero field cooling cycles under an applied magnetic field of H = 1 kOe and H = 2 kOe (for better observation of ZFC curve inflection point).

Notably, neutron diffraction and Mössbauer spectroscopy analyses on bulk $BiFe_{1-x}Mn_xO_3$ compounds suggest that Mn substitution induces modifications in the cycloidal spin modulation, transitioning towards a collinear (G-type) antiferromagnetic order, with spins aligned along the polar axis. This alignment of magnetic moments exclude the possibility of spin canting. [139–141].

Furthermore, the neutron diffraction study of the $Bi_{1-x}Ca_xFe_{0.60}Mn_{0.40}O_3$ (x = 0.10, 0.15) samples [142] confirms the stabilization of the collinear antiferromagnetic structure with the ordered moments of 1.48(2) μB and 1.35(2) μB per Fe/Mn atom at room temperature.

Our investigation supports previous deductions that the collinear antiferromagnetic arrangement, prevalent near the rhombohedral/orthorhombic phase boundary at room temperature is suppressed as the Mn concentration increases. This is corroborated by temperature-dependent magnetization measurements in Fig. 26, showing a decrease in the Néel temperature with increasing Mn and Ca content. Consequently, our results suggest the paramagnetic character of orthorhombic samples (x = 0.10, 0.15 and y = 0.45) at room temperature as their Néel temperatures are 283K (Fig. 28 (a)) and 268K (Fig. 27 (c)) respectively.

All samples exhibit linear field dependencies in magnetization, indicative of either paramagnetic or collinear (G-type) antiferromagnetic states (Fig. 29).

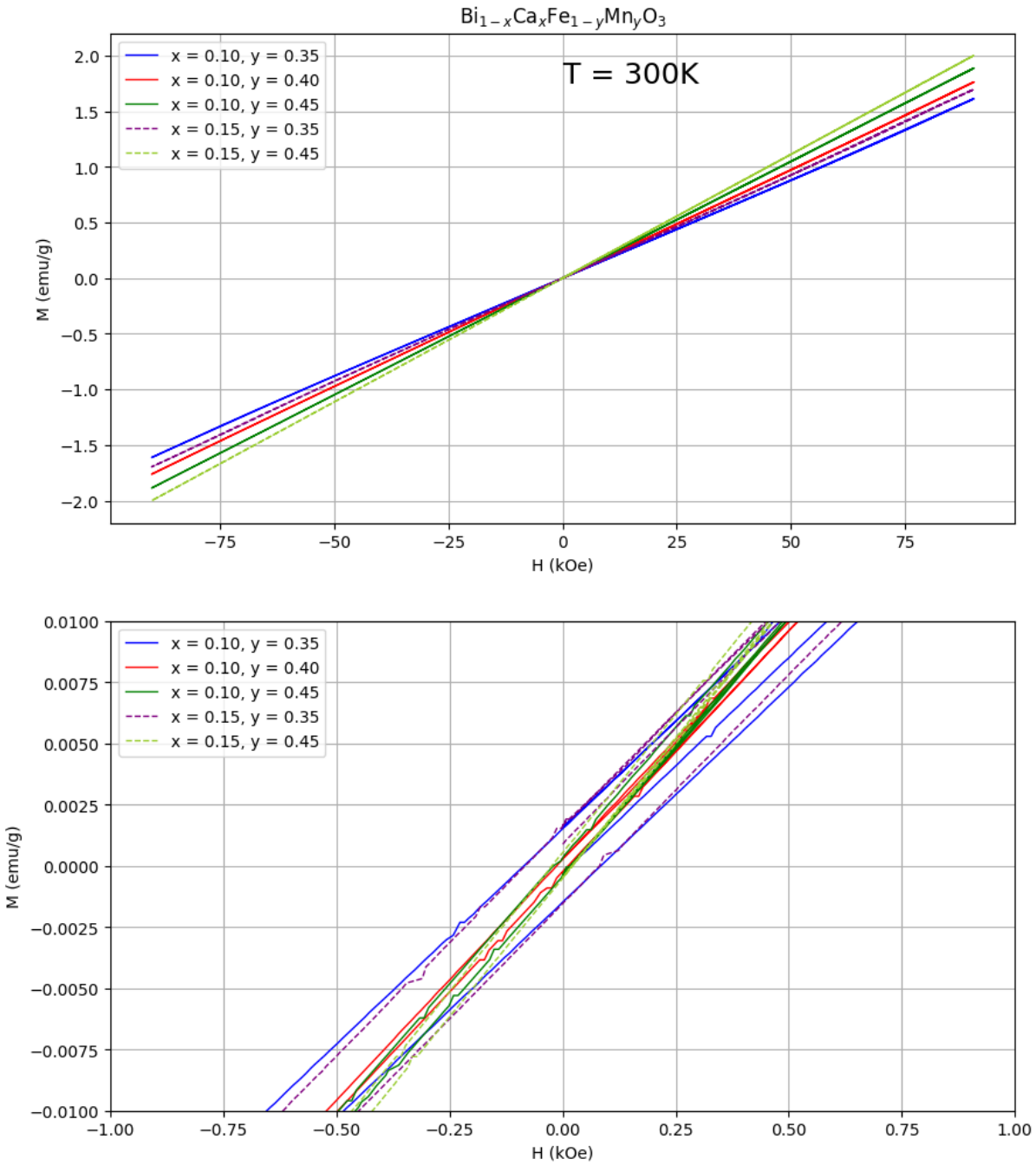

Fig. 29. Magnetic hysteresis loops were obtained through measurements conducted on the $Bi_{1-x}Ca_xFe_{1-y}Mn_yO_3$ compounds at a temperature of T = 300 K. Second image is an enlarged view of a specific region within the main figure, providing enhanced clarity.

Furthermore, no remnant magnetization (Fig. 29) as seen in $Bi_{1-x}Ca_xFeO_3$ with a canted AFM structure [96], nor the anticipated metamagnetic behavior associated with the cycloidal AFM order unique to pure $BiFeO_3$ has been observed for samples x = 0.10, 0.15, y = 0.40 [142], 0.45. However, upon closer examination of the M (H) dependencies obtained for the samples with x = 0.10, 0.15, and y = 0.35 we observe the existence of a small remnant magnetization of 0.0021 emu/g and 0.00213 emu/g.

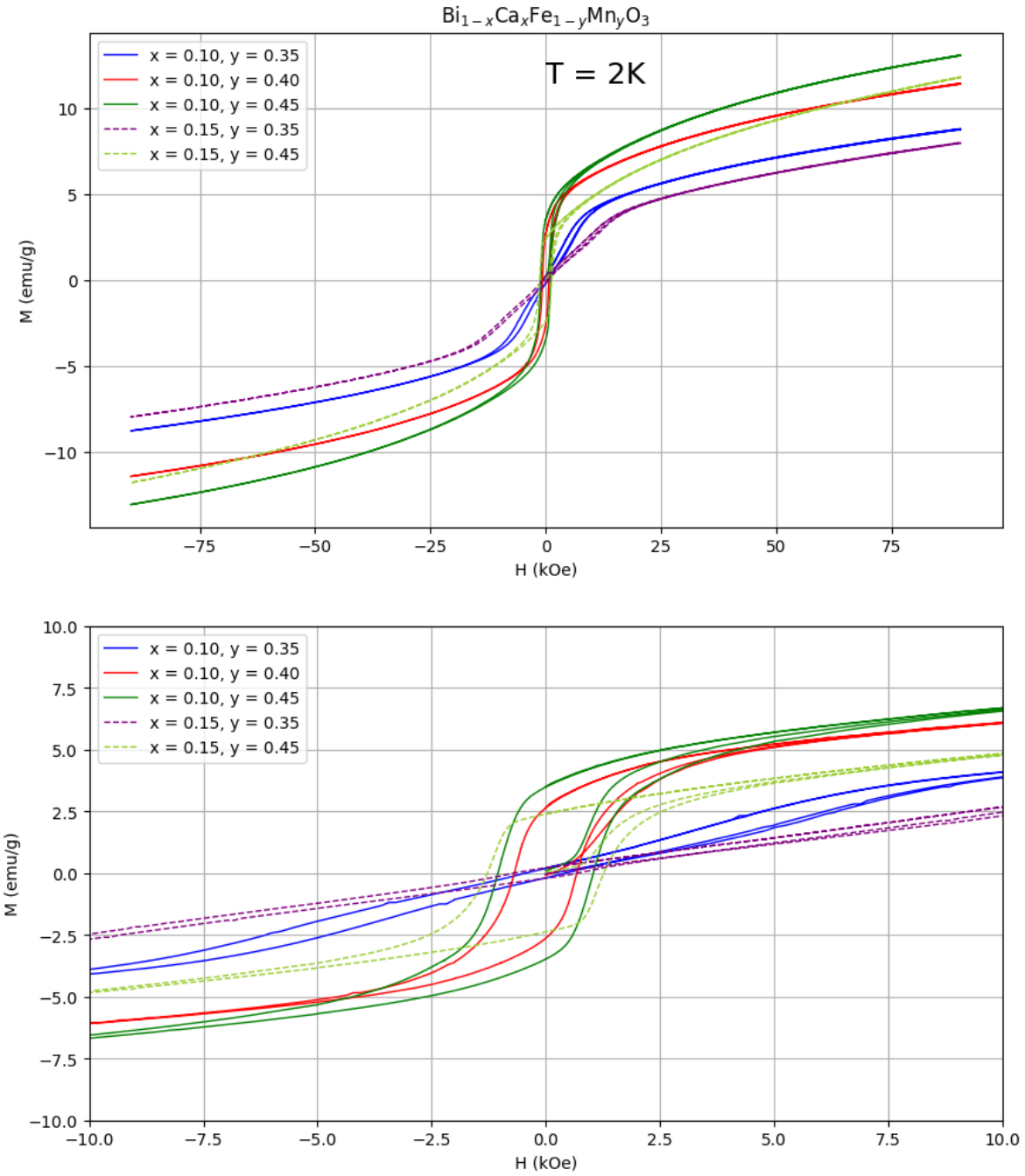

Fig. 30. Magnetic hysteresis loops were acquired by conducting measurements on the $Bi_{1-x}Ca_xFe_{1-y}Mn_yO_3$ compounds at a temperature of T = 2 K. The second image provides an enlarged view of a particular region within the main figure, offering improved clarity.

The magnetic measurements at low temperatures indicate a notable rise in the remanent magnetization in the samples as Mn concentration increases (Fig. 30). Table 3 provides a comparison of the measured remanent magnetization values at temperatures of T = 300 K and T = 2 K and their corresponding Néel temperatures. Several distinct characteristics pertaining to the temperature-dependent evolution of the magnetic properties can be observed.

The magnetic behavior of samples with y = 0.35 and 0.40 exhibits an unusual temperature dependency, characterized by a transition from predominantly antiferromagnetic to weakly ferromagnetic states as the temperature decreases (Fig. 30).

x	y	T = 300 K	T = 2 K	T_N
0.10	0.35	0.00211	0.20	383 K
	0.40	0	2.78	338 K
	0.45	0 (*paramagnetic*)	3.42	283 K
0.15	0.35	0.00213	0.21	369 K
	0.40	0	0.48	319 K
	0.45	0 (*paramagnetic*)	2.49	268 K

Table 3. The remanent magnetization (in emu/g) of the perovskite system $Bi_{1-x}Ca_xFe_{1-y}Mn_yO_3$ samples measured at temperatures of T = 300 K, T = 2 K and correspodning Néel temperatures.

The underlying cause of this behavior is elucidated in [142], where a neutron diffraction analysis of $Bi_{1-x}Ca_xFe_{0.6}Mn_{0.4}O_3$ samples with x = 0.10 and 0.15 revealed a reorientation trend of antiferromagnetically coupled magnetic moments from the c-axis to the a-axis as temperature decreases. This reconfiguration aligns with a weak ferromagnetic ordering at low temperatures.

At room temperature, samples with y = 0.35 display a small remnant magnetization, a deviation from the typical behavior associated with collinear G-type antiferromagnetic ordering as for y = 0.40. Moreover, with decreasing temperature, there is a discernible shift from assumed collinear G-type antiferromagnetism to weak ferromagnetism, as indicated by an increase in remanent magnetization, mirroring the behavior observed for y = 0.40. Although the characterization of samples at y = 0.35 as predominantly collinear G-type antiferromagnetic is complex due to their small remnant magnetization at room temperature, sample series also exhibit deviations from the weak ferromagnetism observed in lightly-doped $BiFeO_3$-based multiferroics, these materials are typically characterized by a high Néel temperature and show minimal changes in remnant magnetization with decreasing temperature. In contrast, we observe large remnant magnitization change in sample series y = 0.35 with temperature decrease, as seen in collinear G-type antiferromagnetic to weak ferromagnetic state order transition.

For clarity, the magnetic behavior observed in $Bi_{1-x}Ca_xFe_{0.65}Mn_{0.35}O_3$ samples with x = 0.10 and 0.15 closely resembles that of $Bi_{1-x}Ca_xFeO_3$ solid solutions which exhibits characteristics indicative of a mixed antiferromagnetic/weak ferromagnetic state. Specifically, these compounds demonstrated a nonzero remanent magnetization, suggesting a partial suppression of the cycloidal modulation which is typically associated with weak ferromagnetism in $BiFeO_3$-based perovskites. This suppression of the modulated structure is attributed to a doping-induced enhancement of magnetic anisotropy. Notably, the elimination of magnetic modulation leads to the emergence of spontaneous magnetization in the rhombohedral phase due to the Dzyaloshinsky–Moriya interaction. [143]. While the magnetic state is expected to be significantly influenced by Ca substitution in $Bi_{1-x}Ca_xFeO_3$, we observe that in $Bi_{1-x}Ca_xFe_{0.65}Mn_{0.35}O_3$ (x = 0.10, 0.15), no substantial change

in the magnetic state is noted. Therefore, we can assume that introduction of additional Mn results in a reduction of Ca influence on the magnetic state and shifts mixed antiferromagnetic/weak ferromagnetic state boundry to larger concentrations of Ca.

Moreover, the increase in Mn concentration within the perovskite system $Bi_{1-x}Ca_xFe_{1-y}Mn_yO_3$ (x = 0.10, 0.15) at room temperature results in intricate transitions in magnetic ordering. At y = 0.35, the samples exhibit a mixed antiferromagnetic/weak ferromagnetic order, reminiscent of the behavior observed in $Bi_{1-x}Ca_xFeO_3$ systems. Here implication is made that a partial suppression of the cycloidal modulation may result in partial stabilization of weak ferromagnetic order which is typical in $BiFeO_3$-based perovskites and lead to canted antiferromagnetic or metamagnetic behavior with a small remnant magnetization. Further increasing in the Mn concentration y = 0.40, 0.45, leads to stabilization of collinear G-type antiferromagnetism as seen in $BiFe_{1-x}Mn_xO_3$ systems. However, y = 0.45 can be described as paramagnetic as their low Néel temperature is observed.

All samples exhibit a linearly dependent increase in magnetization with higher Mn concentration, observed consistently at both T = 2 K and T = 300 K when measured under an applied magnetic field of H = 90 kOe. However, a similar dependence on increased magnetization with varying Ca concentration cannot be inferred at different temperatures. Notably, at T = 300 K, an increase in Ca concentration, known to heavily influence transition from polar to antipolar or nonpolar phases, leads to a higher overall magnetization. Conversely, examination of hysteresis loops at T = 2 K reveals that an increase in Ca concentration reduces the overall magnetization. This can be explained with low temperature induced magnetic ordering. Magnetic moment of Mn^{4+} is smaller than that of Mn^{3+} (S = 3/2 and S = 2, respectively), so some decrease in spontaneous magnetization observed with increase in Ca, which leads to the increase in the elevation of Mn^{4+} concentration (if we consider the samples with the same Mn content, y) is quite natural. On the other hand, increase magnetization with larger Ca concentration at T = 300 K and magnetic field of H = 90 kOe can arise due to the effect coming from the temperature and composition dependence of the magnetocrystalline anisotropy parameters which specify the energy required to magnetize a sample in a particular direction. The magnetocrystalline anisotropy is due to the coupling of the orbital motion of the electrons with the crystal electric field affecting the spin magnetic moments via the spin-orbit interaction.

Furthermore, the low-temperature remanent magnetization values for samples with y = 0.45 (refer to table 3) greatly exceed those commonly observed for weakly ferromagnetic bismuth ferrites near the polar/nonpolar (antipolar) phase boundary, typically falling within the range of approximately 0.3 emu/g. Moreover, samples at y = 0.35 exhibit remanent magnetization consistent with the anticipated values typical for weakly ferromagnetic order at T = 2 K.

Notably, within the perovskite system $Bi_{1-x}Ca_xFe_{1-y}Mn_yO_3$, specifically when considering x = 0.10, 0.15 [144] and y = 0.40 the magnetic properties exhibit remarkable similarity. The apparent disparity in their magnetic hysteresis loops at T = 2 K stems from a temperature-induced spin-reorientational transition. At T = 2 K, in x = 0.10 , the reorientation of antiferromagnetically-coupled spins from the c to a axis is already completed. Conversely, in x = 0.15, there exists a phase coexistence at T = 2 K. Here, an antiferromagnetic phase with spins aligned along the c axis coex-

ists with a weak ferromagnetic (canted) phase, where spins are predominantly aligned along the a axis. The application of a magnetic field aids in the complete reorientation of spins from the c to the a axis for x = 0.15 [144] This process is accompanied by the reorientation of the glassy-phase moments, which are exchange-coupled with the AFM spins across the boundaries of the antiferromagnetic and glassy phases. This results in a pronounced metamagnetic behavior [144]. This is due to the contribution of Mn^{3+}: $t_{2g}^3 e_g^1$–O–Mn^{4+}: $t_{2g}^3 e_g^0$ superexchange which compete with the main antiferromagnetic exchange involving Fe ions, thus resulting in the formation of a glassy magnetic phase at low temperatures.

Conclusions

Our project aimed to explore an innovative method for achieving large magnetization switching in ferroelectric compounds. We used a doping strategy which involves partial substitution of Fe^{3+} ions with manganese in the mixed (Mn^{3+}/Mn^{4+}) oxidation state, facilitating ferromagnetic exchange coupling. This approach was applied to $Bi_{1-x}Ca_xFe_{1-y}Mn_yO_3$ perovskite system, where the introduction of Mn^{4+} compensates for the charge imbalance caused by the substitution of Bi^{3+} with Ca^{2+} ions. Our investigation focused on alterations in crystal structure and magnetic properties near the chemically stabilized polar/anti(non)polar phase boundary. Ceramic samples of these perovskites where synthesized via a solid-state reaction method and analyzed using X-ray diffraction, scanning electron microscopy, and vibrating sample magnetometry techniques.

- X-ray diffraction (XRD) measurements and Retvield profile refinement analysis revealed the crystallographic structure of the samples, indicating a transition from a polar to anti(non)polar phase within the perovskite system $Bi_{1-x}Ca_xFe_{1-y}Mn_yO_3$. This transition becomes discernible for values of x = 0.10 (antipolar) and x = 0.15 (nonpolar), starting to occurr within the range of $0.40 < y < 0.45$.

- The transition to the nonpolar structure as Mn concentration increases in the perovskite system $Bi_{1-x}Ca_xFe_{1-y}Mn_yO_3$ takes place when x = 0.15, and notably, it occurs without any accompanying phase coexistence, in contrast to the antipolar transition observed at x = 0.10, y = 0.45. This discrepancy suggests assumption that phase coexistence may emerge for the nonpolar structure within the range of $0.15 < x \leq 0.19$ and/or at x = 0.15, within the interval $0.40 < y < 0.45$.

- SEM captured images displayed the involvement of intricate mechanisms facilitating crystal growth. It is proposed that a saturation threshold exists, where the influence of Ca on grain size exceeds that of Mn. Upon reaching this threshold, the influence of Mn becomes predominant, resulting in approximately a tenfold increase ($0.10 \leq y \leq 0.35$) in grain size. Further grain growth is faciliated by the primary consequence of the increase in Ca content which elavates Mn^{4+} concentration possessing a significantly smaller ionic radius compared to Fe^{3+} and Mn^{3+}, a factor which can facilitate manganese diffusion and further promote crystal grain growth.

- Slighty larger material brittleness is discernible in the $Bi_{0.90}Ca_{0.10}Fe_{0.55}Mn_{0.45}O_3$ sample. It can be atributed to the presence of $R3c + Pnam$ phases as identified through XRD analysis, which consequently may instigate internal strain forces within the grain structure, thus leading to heightened brittleness. Further investigation is imperative to corroborate this proposition within the parameter range of $0.15 < x < 0.19$, given the potential coexistence of different compositional structures may be observed.

- Samples high phase purity has been confirmed by comparing secondary electron microscopy images with backscattered electron microscopy images. In this case, no composition-dependent variations in image contrast were observed, indicating the absence of secondary impurity phases in the sample.

- VSM measurments revelead that all samples exhibit predominantly linear field dependencies in magnetization, indicative of either paramagnetic or collinear (G-type) antiferromagnetic state at room temperature.

- Samples with y = 0.45 in $Bi_{1-x}Ca_xFe_{1-y}Mn_yO_3$ perovskite system, can be characterized as paramagnetic as their Néel temperature are below room temperature, 283 K for x = 0.10 and 268 K for x = 0.15.

- The magnetic behavior of samples with y = 0.35 and 0.40 exhibits an unusual temperature dependency, characterized by a transition from predominantly collinear G-type antiferromagnetic to weakly ferromagnetic states as the temperature decrease.

- All samples exhibit a linearly dependent increase in magnetization with higher Mn concentration, observed consistently at both T = 2 K and T = 300 K when measured under an applied magnetic field of H = 90 kOe, although the similar dependency diverges when considering higher Ca concentration at T = 2 K. This divergence can arise due low temperature induced magnetic ordering.

- Remanent magnetization values at T = 2 K for samples with [0.10, 0.40], [0.10, 0.45], [0.15, 0.45] greatly exceed those commonly observed (≈ 0.3 emu/g) for weakly ferromagnetic bismuth ferrites near the juncture of the polar/nonpolar(antipolar) phases.

References

[1] N. A. Spaldin and R. Ramesh, Advances in magnetoelectric multiferroics, *Nature Materials*, Mar. 2019, **18**, 203–212.

[2] D. V. Karpinsky, M. V. Silibin, S. I. Latushka, *et al.*, Temperature-Driven Transformation of the Crystal and Magnetic Structures of $BiFe_{0.7}Mn_{0.3}O_3$ Ceramics, *Nanomaterials*, Jan. 2022, **12**, 2813.

[3] S. Ramay, M. H. Humayun, and M. S. Anwar, Electrical properties of ferroelectric materials, *LUMS School of Science and Engineering*, Mar. 2022.

[4] J. Fousek, Joseph valasek and the discovery of ferroelectricity, *Proceedings of 1994 IEEE International Symposium on Applications of Ferroelectrics*, 1994, 1–5.

[5] A. R. West, Basic solid state chemistry, *John Wiley and Sons*, 1996, 53–56, 331–338.

[6] A. Teja and P. Y. Koh, Synthesis, properties, and applications of magnetic iron oxide nanoparticles, *Prog. Cryst. Growth Charact. Mater.*, 03 2009, **55**, 22–45.

[7] K. Bhoi, H. S. Mohanty, Ravikant, *et al.*, Unravelling the nature of magneto-electric coupling in room temperature multiferroic particulate $(PbFe_{0.5}Nb_{0.5}O_3)$–$(Co_{0.6}Zn_{0.4}Fe_{1.7}Mn_{0.3}O_4)$ composites, *Scientific Reports*, Feb. 2021, **11**, 3149.

[8] M. S. Bernardo, Synthesis, microstructure and properties of $BiFeO_3$-based multiferroic materials: A review, *Boletín de la Sociedad Española de Cerámica y Vidrio*, Feb. 2014, **53**, 1–14.

[9] W. Eerenstein, N. D. Mathur, and J. F. Scott, Multiferroic and magnetoelectric materials, *Nature*, Aug. 2006, **442**, 759–765.

[10] N. Ortega, A. Kumar, J. F. Scott, and R. S. Katiyar, Multifunctional magnetoelectric materials for device applications, *Journal of Physics: Condensed Matter*, Dec. 2015, **27**, 504002.

[11] S. J. Williamson and M. Hoke, *Advances in Biomagnetism*. Springer Science & Business Media, Dec. 2012.

[12] E. Elzenheimer, C. Bald, E. Engelhardt, *et al.*, Quantitative Evaluation for Magnetoelectric Sensor Systems in Biomagnetic Diagnostics, *Sensors*, Jan. 2022, **22**, 1018.

[13] P. Hayes, Converse Magnetoelectric Resonators for Biomagnetic Field Sensing, May 2021. Dissertation Accepted: 2020-12-03.

[14] R. Jahns, R. Knochel, H. Greve, E. Woltermann, E. Lage, and E. Quandt, Magnetoelectric sensors for biomagnetic measurements, in *2011 IEEE International Symposium on Medical Measurements and Applications*, (Bari, Italy), 107–110, IEEE, May 2011.

[15] C. Bald and G. Schmidt, Processing Chain for Localization of Magnetoelectric Sensors in Real Time, *Sensors*, Aug. 2021, **21**, 5675.

[16] T. Sander, A. Jodko-Władzińska, S. Hartwig, R. Brühl, and T. Middelmann, Optically pumped magnetometers enable a new level of biomagnetic measurements, *Advanced Optical Technologies*, Nov. 2020, **9**, 247–251.

[17] P. Ripka, *Magnetic Sensors and Magnetometers, Second Edition*. Artech House, July 2021.

[18] H. Wu, A. Tatarenko, M. Bichurin, and Y. Wang, A multiferroic module for biomechanical energy harvesting, *Nano Energy*, May 2021, **83**, 105777.

[19] M. Bibes and A. Barthelemy, Oxide Spintronics, *IEEE Transactions on Electron Devices*, May 2007, **54**, 1003–1023.

[20] S. Manipatruni, D. E. Nikonov, C.-C. Lin, *et al.*, Scalable energy-efficient magnetoelectric spin–orbit logic, *Nature*, Jan. 2019, **565**, 35–42.

[21] J. M. D. Coey, Noncollinear spin structures, *Canadian Journal of Physics*, Oct. 1987, **65**, 1210–1232.

[22] P. Agarwal, L. Huang, S. Ter Lim, and R. Singh, Electric-field control of nonlinear THz spintronic emitters, *Nature Communications*, July 2022, **13**, 4072.

[23] A. A. Wagh, P. Garg, K. Mallick, S. Elizabeth, and P. S. A. Kumar, Highly tunable spin Hall magnetoresistance in room-temperature magnetoelectric multiferroic, $Sr_3Co_2Fe_{24}O_{41}$Pt hybrids, May 2022.

[24] S. R. Burns, O. Paull, J. Juraszek, V. Nagarajan, and D. Sando, The Experimentalist's Guide to the Cycloid, or Noncollinear Antiferromagnetism in Epitaxial BiFeO $_3$, *Advanced Materials*, Nov. 2020, **32**, 2003711.

[25] Z. Tan, L. Hong, Z. Fan, *et al.*, Thinning ferroelectric films for high-efficiency photovoltaics based on the Schottky barrier effect, *NPG Asia Materials*, Dec. 2019, **11**, 20.

[26] C. Paillard, X. Bai, I. C. Infante, *et al.*, Photovoltaics with Ferroelectrics: Current Status and Beyond, *Advanced Materials*, July 2016, **28**, 5153–5168.

[27] R. Nechache, C. Harnagea, S. Li, L. Cardenas, W. Huang, J. Chakrabartty, and F. Rosei, Bandgap tuning of multiferroic oxide solar cells, *Nature Photonics*, Jan. 2015, **9**, 61–67.

[28] Y. Sun, X. Liu, J. Zeng, J. Yan, D. Shi, and H. Liu, Photovoltaic Effects in Polarized Polycrystalline $BiFeO_3$ Films, *Journal of Electronic Materials*, Nov. 2015, **44**, 4207–4212.

[29] J. Chakrabartty, R. Nechache, C. Harnagea, S. Li, and F. Rosei, Enhanced photovoltaic properties in bilayer $BiFeO_3$/Bi-Mn-O thin films, *Nanotechnology*, May 2016, **27**, 215402.

[30] K. Guo, X. Wang, R. Zhang, Z. Fu, L. Zhang, G. Ma, and C. Deng, Multiferroic oxide BFCNT/BFCO heterojunction black silicon photovoltaic devices, *Light: Science & Applications*, Sept. 2021, **10**, 201.

[31] S. M. Young, F. Zheng, and A. M. Rappe, Prediction of a Linear Spin Bulk Photovoltaic Effect in Antiferromagnets, *Physical Review Letters*, Jan. 2013, **110**, 057201.

[32] E. Stimphil, A. Nagesetti, R. Guduru, T. Stewart, A. Rodzinski, P. Liang, and S. Khizroev, Physics considerations in targeted anticancer drug delivery by magnetoelectric nanoparticles, *Applied Physics Reviews*, June 2017, **4**, 021101.

[33] K. Yue, R. Guduru, J. Hong, P. Liang, M. Nair, and S. Khizroev, Magneto-Electric Nano-Particles for Non-Invasive Brain Stimulation, *PLoS ONE*, Sept. 2012, **7**, e44040.

[34] I. T. Smith, E. Zhang, Y. A. Yildirim, *et al.*, Nanomedicine and nanobiotechnology applications of magnetoelectric nanoparticles, *WIREs Nanomedicine and Nanobiotechnology*, Sept. 2022, **n/a**, e1849.

[35] R. Guduru, P. Liang, M. Yousef, J. Horstmyer, and S. Khizroev, Mapping the Brain's electric fields with Magnetoelectric nanoparticles, *Bioelectronic Medicine*, Dec. 2018, **4**, 10.

[36] D. Khomskii, Classifying multiferroics: Mechanisms and effects, *Physics*, Mar. 2009, **2**, 20.

[37] J. B. Goodenough, W. Gräper, F. Holtzberg, *et al.*, *Magnetic and Other Properties of Oxides and Related Compounds*. Springer Berlin Heidelberg, Jan. 1970.

[38] N. A. Hill, Why Are There so Few Magnetic Ferroelectrics?, *The Journal of Physical Chemistry B*, July 2000, **104**, 6694–6709.

[39] D. I. Khomskii, Multiferroics: Different ways to combine magnetism and ferroelectricity, *Journal of Magnetism and Magnetic Materials*, Nov. 2006, **306**, 1–8.

[40] T. Kimura, T. Goto, H. Shintani, K. Ishizaka, T. Arima, and Y. Tokura, Magnetic control of ferroelectric polarization, *Nature*, Nov. 2003, **426**, 55–58.

[41] N. Hur, S. Park, P. A. Sharma, J. S. Ahn, S. Guha, and S.-W. Cheong, Electric polarization reversal and memory in a multiferroic material induced by magnetic fields, *Nature*, May 2004, **429**, 392–395.

[42] H. Katsura, N. Nagaosa, and A. V. Balatsky, Spin Current and Magnetoelectric Effect in Noncollinear Magnets, *Physical Review Letters*, July 2005, **95**, 057205.

[43] M. Mostovoy, Ferroelectricity in Spiral Magnets, *Physical Review Letters*, Feb. 2006, **96**, 067601.

[44] T.-h. Arima, Ferroelectricity Induced by Proper-Screw Type Magnetic Order, *Journal of the Physical Society of Japan*, July 2007, **76**, 073702.

[45] Y. J. Choi, H. T. Yi, S. Lee, Q. Huang, V. Kiryukhin, and S.-W. Cheong, Ferroelectricity in an Ising Chain Magnet, *Physical Review Letters*, Jan. 2008, **100**, 047601.

[46] H. Wu, T. Burnus, Z. Hu, *et al.*, Ising Magnetism and Ferroelectricity in Ca_3CoMnO_6, *Physical Review Letters*, Jan. 2009, **102**, 026404.

[47] I. A. Sergienko, C. Şen, and E. Dagotto, Ferroelectricity in the Magnetic E-Phase of Orthorhombic Perovskites, *Physical Review Letters*, Nov. 2006, **97**, 227204.

[48] B. Lorenz, Y.-Q. Wang, and C.-W. Chu, Ferroelectricity in perovskite $HoMnO_3$ and $YMnO_3$, *Physical Review B*, Sept. 2007, **76**, 104405.

[49] G. D. Liu, X. F. Dai, S. Y. Yu, *et al.*, Physical and electronic structure and magnetism of Mn_2NiGa: Experiment and density-functional theory calculations, *Physical Review B*, Aug. 2006, **74**, 054435.

[50] L. N. Bulaevskii, C. D. Batista, M. V. Mostovoy, and D. I. Khomskii, Electronic orbital currents and polarization in Mott insulators, *Physical Review B*, July 2008, **78**, 024402.

[51] C. Pascual-Gonzalez, G. Schileo, and A. Feteira, Single-phase, composite and laminate multiferroics, in *Magnetic, Ferroelectric, and Multiferroic Metal Oxides*, 457–484, Elsevier, 2018.

[52] Y. Wang, J. Hu, Y. Lin, and C.-W. Nan, Multiferroic magnetoelectric composite nanostructures, *NPG Asia Materials*, Apr. 2010, **2**, 61–68.

[53] C. Chen, J. Cheng, S. Yu, L. Che, and Z. Meng, Hydrothermal synthesis of perovskite bismuth ferrite crystallites, *Journal of Crystal Growth*, May 2006, **291**, 135–139.

[54] J.-H. Xu, H. Ke, D.-C. Jia, W. Wang, and Y. Zhou, Low-temperature synthesis of $BiFeO_3$ nanopowders via a sol–gel method, *Journal of Alloys and Compounds*, Mar. 2009, **472**, 473–477.

[55] A. Srinivas, F. Boey, T. Sritharan, D. W. Kim, K. S. Hong, and S. V. Suryanarayana, Study of piezoelectric, magnetic and magnetoelectric measurements on $SrBi_3Nb_2FeO_{12}$ ceramic, *Ceramics International*, Jan. 2004, **30**, 1431–1433.

[56] M. T. Buscaglia, L. Mitoseriu, V. Buscaglia, I. Pallecchi, M. Viviani, P. Nanni, and A. S. Siri, Preparation and characterisation of the magneto-electric $xBiFeO_3$–$(1\text{-}x)BaTiO_3$ ceramics, *Journal of the European Ceramic Society*, Jan. 2006, **26**, 3027–3030.

[57] W. M. Zhu and Z. G. Ye, Effects of chemical modification on the electrical properties of $0.67BiFeO_3$-$0.33PbTiO_3$ ferroelectric ceramics, *Ceramics International*, Jan. 2004, **30**, 1435–1442.

[58] I. Szafraniak, M. Połomska, B. Hilczer, A. Pietraszko, and L. Kępiński, Characterization of $BiFeO_3$ nanopowder obtained by mechanochemical synthesis, *Journal of the European Ceramic Society*, Jan. 2007, **27**, 4399–4402.

[59] V. F. Freitas, H. L. C. Grande, S. N. de Medeiros, I. A. Santos, L. F. Cótica, and A. A. Coelho, Structural, microstructural and magnetic investigations in high-energy ball milled $BiFeO_3$ and $Bi_{0.95}Eu_{0.05}FeO_3$ powders, *Journal of Alloys and Compounds*, Aug. 2008, **461**, 48–52.

[60] J. K. Kim, S. S. Kim, and W.-J. Kim, Sol–gel synthesis and properties of multiferroic $BiFeO_3$, *Materials Letters*, Dec. 2005, **59**, 4006–4009.

[61] T. T. Carvalho and P. B. Tavares, Synthesis and thermodynamic stability of multiferroic $BiFeO_3$, *Materials Letters*, Sept. 2008, **62**, 3984–3986.

[62] L. Xiaomeng, X. Jimin, S. Yuanzhi, and L. Jiamin, Surfactant-assisted hydrothermal preparation of submicrometer-sized two-dimensional $BiFeO_3$ plates and their photocatalytic activity, *Journal of Materials Science*, Aug. 2007, **42**, 6824–6827.

[63] E. Jartych, T. Pikula, K. Kowal, J. Dzik, P. Guzdek, and D. Czekaj, Magnetoelectric Effect in Ceramics Based on Bismuth Ferrite, *Nanoscale Research Letters*, Apr. 2016, **11**, 234.

[64] G. Catalan and J. F. Scott, Physics and Applications of Bismuth Ferrite, *Advanced Materials*, June 2009, **21**, 2463–2485.

[65] H. Naganuma, *Multifunctional Characteristics of B-site Substituted $BiFeO_3$ Films*. InteChOpen, Aug. 2011.

[66] S. M. Selbach, T. Tybell, M.-A. Einarsrud, and T. Grande, Size-Dependent Properties of Multiferroic $BiFeO_3$ Nanoparticles, *Chemistry of Materials*, Dec. 2007, **19**, 6478–6484.

[67] J. Wang, J. B. Neaton, H. Zheng, *et al.*, Epitaxial $BiFeO_3$ multiferroic thin film heterostructures, *Science (New York, N.Y.)*, Mar. 2003, **299**, 1719–1722.

[68] H. Béa, M. Bibes, S. Fusil, *et al.*, Investigation on the origin of the magnetic moment of $BiFeO_3$ thin films by advanced x-ray characterizations, *Physical Review B*, July 2006, **74**, 020101.

[69] A. M. Glazer, The classification of tilted octahedra in perovskites, *Acta Crystallographica Section B Structural Crystallography and Crystal Chemistry*, Nov. 1972, **28**, 3384–3392.

[70] V. M. Goldschmidt, Die Gesetze der Krystallochemie, *Die Naturwissenschaften*, May 1926, **14**, 477–485.

[71] F. Kubel and H. Schmid, Structure of a ferroelectric and ferroelastic monodomain crystal of the perovskite $BiFeO_3$, *Acta Crystallographica Section B Structural Science*, Dec. 1990, **46**, 698–702.

[72] C. Michel, J.-M. Moreau, G. D. Achenbach, R. Gerson, and W. James, The atomic structure of $BiFeO_3$, *Solid State Communications*, May 1969, **7**, 701–704.

[73] J.-G. Park, M. D. Le, J. Jeong, and S. Lee, Structure and spin dynamics of multiferroic $BiFeO_3$, *Journal of Physics: Condensed Matter*, Oct. 2014, **26**, 433202.

[74] I. Sosnowska, R. Przeniosło, P. Fischer, and V. Murashov, Neutron diffraction studies of the crystal and magnetic structures of $BiFeO_3$ and $Bi_{0.93}La_{0.07}FeO_3$, *Journal of Magnetism and Magnetic Materials*, July 1996, **160**, 384–385.

[75] R. Fishman, The microscopic model of $BiFeO_3$, *Physica B: Condensed Matter*, May 2018, **536**, 115–117.

[76] I. Sosnowska, T. P. Neumaier, and E. Steichele, Spiral magnetic ordering in bismuth ferrite, *Journal of Physics C: Solid State Physics*, Aug. 1982, **15**, 4835–4846.

[77] D. L. Cortie, A. P. J. Stampfl, F. Klose, *et al.*, The magnetic structure of an epitaxial $BiMn_{0.5}Fe_0.5O_3$ thin film on $SrTiO_3$ (001) studied with neutron diffraction, *Applied Physics Letters*, Oct. 2012, **101**, 172404.

[78] D. Sando, F. Appert, B. Xu, *et al.*, A magnetic phase diagram for nanoscale epitaxial BiFeO $_3$ films, *Applied Physics Reviews*, Dec. 2019, **6**, 041404.

[79] A. Haykal, J. Fischer, W. Akhtar, *et al.*, Antiferromagnetic textures in $BiFeO_3$ controlled by strain and electric field, *Nature Communications*, Apr. 2020, **11**, 1704.

[80] D. Sando, A. Agbelele, D. Rahmedov, *et al.*, Crafting the magnonic and spintronic response of $BiFeO_3$ films by epitaxial strain, *Nature Materials*, July 2013, **12**, 641–646.

[81] A. M. Kadomtseva, Y. F. Popov, A. P. Pyatakov, G. P. Vorob'ev, A. K. Zvezdin, and D. Viehland *Phase transitions*, 2008.

[82] F. Bai, J. Wang, M. Wuttig, *et al.*, Destruction of spin cycloid in (111)c-oriented $BiFeO_3$ thin films by epitiaxial constraint: Enhanced polarization and release of latent magnetization, *Applied Physics Letters*, Jan. 2005, **86**, 032511.

[83] Y. F. Popov, A. M. Kadomtseva, G. P. Vorob'ev, and A. K. Zvezdin, Discovery of the linear magnetoelectric effect in magnetic ferroelectric BiFeo $_3$ in a strong magnetic field, *Ferroelectrics*, Jan. 1994, **162**, 135–140.

[84] A. Sparavigna, A. Strigazzi, and A. Zvezdin, Electric-field effects on the spin-density wave in magnetic ferroelectrics, *Physical Review B*, Aug. 1994, **50**, 2953–2957.

[85] C.-H. Yang, D. Kan, I. Takeuchi, V. Nagarajan, and J. Seidel, Doping $BiFeO_3$: approaches and enhanced functionality, *Physical Chemistry Chemical Physics*, 2012, **14**, 15953.

[86] D. Kan, L. Pálová, V. Anbusathaiah, *et al.*, Universal Behavior and Electric-Field-Induced Structural Transition in Rare-Earth-Substituted $BiFeO_3$, *Advanced Functional Materials*, Mar. 2010, **20**, 1108–1115.

[87] H. Hojo, K. Oka, K. Shimizu, H. Yamamoto, R. Kawabe, and M. Azuma, Development of Bismuth Ferrite as a Piezoelectric and Multiferroic Material by Cobalt Substitution, *Advanced Materials*, Aug. 2018, **30**, 1705665.

[88] J. Matthews and A. Blakeslee, Defects in epitaxial multilayers, *Journal of Crystal Growth*, Dec. 1974, **27**, 118–125.

[89] P. Zubko, G. Catalan, and A. K. Tagantsev, Flexoelectric Effect in Solids, *Annual Review of Materials Research*, July 2013, **43**, 387–421.

[90] Q. H. Jiang, J. Ma, Y. H. Lin, C.-W. Nan, Z. Shi, and Z. J. Shen, Multiferroic properties of $Bi_{0.87}La_{0.05}Tb_{0.08}FeO_3$ ceramics prepared by spark plasma sintering, *Applied Physics Letters*, July 2007, **91**, 022914.

[91] J. A. M. Cagigas, D. S. Candela, and E. Baggio-Saitovitch, Effect of rare earth doping on $BiFeO_3$ magnetic and structural properties (La, Gd), *Journal of Physics: Conference Series*, Jan. 2010, **200**, 012134.

[92] S. B. Emery, C.-J. Cheng, D. Kan, *et al.*, Phase coexistence near a morphotropic phase boundary in Sm-doped $BiFeO_3$ films, *Applied Physics Letters*, Oct. 2010, **97**, 152902.

[93] I. Levin, M. G. Tucker, H. Wu, *et al.*, Displacive Phase Transitions and Magnetic Structures in Nd-Substituted $BiFeO_3$, *Chemistry of Materials*, Apr. 2011, **23**, 2166–2175.

[94] X. Tan, C. Ma, J. Frederick, S. Beckman, and K. G. Webber, The Antiferroelectric Ferroelectric Phase Transition in Lead-Containing and Lead-Free Perovskite Ceramics, *Journal of the American Ceramic Society*, Dec. 2011, **94**, 4091–4107.

[95] B. Xu, D. Wang, J. Íñiguez, and L. Bellaiche, Finite-Temperature Properties of Rare-Earth-Substituted $BiFeO_3$ Multiferroic Solid Solutions, *Advanced Functional Materials*, Jan. 2015, **25**, 552–558.

[96] V. A. Khomchenko, I. O. Troyanchuk, D. M. Többens, V. Sikolenko, and J. A. Paixão, Composition- and temperature-driven structural transitions in $Bi_{1-x}Ca_xFeO_3$ multiferroics: a neutron diffraction study, *Journal of Physics: Condensed Matter*, Apr. 2013, **25**, 135902.

[97] A. Kozakov, A. Kochur, V. Torgashev, *et al.*, $Bi_{1-x}Ca_x$ $FeO_3(0 \leq x \leq 1)$ ceramics: Crystal structure, phase and elemental composition, and chemical bonding from X-ray diffraction, Raman scattering, Mössbauer, and X-ray photoelectron spectra, *Journal of Alloys and Compounds*, Apr. 2016, **664**, 392–405.

[98] V. A. Khomchenko and J. A. Paixão, Spontaneous magnetization in the polar phase of Bi_{1-x} Ca_x $FeO_{3-2/x}$ perovskites: The role of anion vacancies, *Journal of Applied Physics*, Dec. 2014, **116**, 214105.

[99] V. A. Khomchenko and J. A. Paixão, Structural defects as a factor controlling the magnetic properties of pure and Ti-doped $Bi_{1-x}Ca_{\ x}$ $FeO_{3-x/2}$ multiferroics, *Journal of Physics: Condensed Matter*, Nov. 2015, **27**, 436002.

[100] I. O. Troyanchuk, M. V. Bushinsky, D. V. Karpinsky, V. Sirenko, V. Sikolenko, and V. Efimov, Structural and magnetic phases of $Bi_{1-x}A_xFeO_3$-δ (A = Sr, Pb) perovskites, *The European Physical Journal B*, Feb. 2010, **73**, 375–381.

[101] R. D. Shannon, Revised effective ionic radii and systematic studies of interatomic distances in halides and chalcogenides, *Acta Crystallographica Section A*, Sept. 1976, **32**, 751–767.

[102] E. Mostafavi, A. Ataie, M. Ahmadzadeh, M. Palizdar, T. Comyn, and A. Bell, Synthesis of nano-structured $Bi_{1-x}Ba_xFeO_3$ ceramics with enhanced magnetic and electrical properties, *Materials Chemistry and Physics*, July 2015, **162**, 106–112.

[103] R. Mardani, The synthesis of Ba^{2+} doped multiferroic $BiFeO_3$ nanoparticles using co-precipitation method in the presence of various surfactants and the investigation of structural and magnetic features, *Modern Physics Letters B*, May 2017, **31**, 1750169.

[104] C. Lepoittevin, S. Malo, N. Barrier, N. Nguyen, G. Van Tendeloo, and M. Hervieu, Long-range ordering in the $Bi_{1-x}AE_xFeO_{3-x/2}$ perovskites: $Bi_{1/3}Sr_{2/3}FeO_{2.67}$ and $Bi_{1/2}Ca_{1/2}FeO_{2.75}$, *Journal of Solid State Chemistry*, Oct. 2008, **181**, 2601–2609.

[105] T. Kimura, S. Kawamoto, I. Yamada, M. Azuma, M. Takano, and Y. Tokura, Magnetocapacitance effect in multiferroic $BiMnO_3$, *Physical Review B*, May 2003, **67**, 180401.

[106] D. V. Karpinsky, M. V. Silibin, D. V. Zhaludkevich, *et al.*, Crystal and Magnetic Structure Transitions in BiMnO3+δ Ceramics Driven by Cation Vacancies and Temperature, *Materials*, Oct. 2021, **14**, 5805.

[107] V. A. Khomchenko, L. C. J. Pereira, and J. A. Paixão, Structural and magnetic phase transitions in Bi_{1-x} Nd_x Fe_{1-x} Mn_xO_3 multiferroics, *Journal of Applied Physics*, Jan. 2014, **115**, 034102.

[108] D. V. Karpinsky, M. V. Silibin, S. I. Latushka, *et al.*, Structural and Magnetic Phase Transitions in $BiFe_{1-x}Mn_xO_3$ Solid Solution Driven by Temperature, *Nanomaterials*, May 2022, **12**, 1565.

[109] D. Karpinsky, M. Silibin, A. Trukhanov, *et al.*, A correlation between crystal structure and magnetic properties in co-doped $BiFeO_3$ ceramics, *Journal of Physics and Chemistry of Solids*, Mar. 2019, **126**, 164–169.

[110] I. O. Troyanchuk, D. V. Karpinsky, M. V. Bushinsky, *et al.*, Isothermal structural transitions, magnetization and large piezoelectric response in Bi_{1-x} La_xFeO_3 perovskites, *Physical Review B*, Feb. 2011, **83**, 054109.

[111] I. O. Troyanchuk, D. V. Karpinsky, M. V. Bushinsky, O. S. Mantytskaya, N. V. Tereshko, and V. N. Shut, Phase Transitions, Magnetic and Piezoelectric Properties of Rare-Earth-Substituted $BiFeO_3$ Ceramics, *Journal of the American Ceramic Society*, Dec. 2011, **94**, 4502–4506.

[112] V. A. Khomchenko, D. V. Karpinsky, and J. A. Paixão, Magnetostructural correlations in $BiFeO_3$ based multiferroics, *Journal of Materials Chemistry C*, 2017, **5**, 3623–3629.

[113] L. Yin, Y. Sun, F. Zhang, *et al.*, Magnetic and electrical properties of $Bi_{0.8}Ca_{0.2}Fe_{1-x}Mn_xO_3$ ($0 \leq x \leq 0.5$), *Journal of Alloys and Compounds*, Nov. 2009, **488**, 254–259.

[114] D. Chateigner, Thin film analysis by X-ray scattering., *Journal of Applied Crystallography*, Dec. 2006, **39**, 925–926.

[115] L. H. Schwartz and J. B. Cohen, The Dynamical Theory of Diffraction, in *Diffraction from Materials*, 469–537, Berlin, Heidelberg: Springer Berlin Heidelberg, 1987.

[116] R. E. Dinnebier and S. J. L. Billinge, eds., *Powder Diffraction: Theory and Practice*. Cambridge: Royal Society of Chemistry, 2008.

[117] I. C. Noyan and J. B. Cohen, *Residual Stress: Measurement by Diffraction and Interpretation*. Springer, Mar. 2013.

[118] W. L. Bragg, The Diffraction of Short Electromagnetic Waves by a Crystal, *Scientia*, 1929, **23**, 153.

[119] Z. Wang, Experimental Study and Modelling of Thermomechanical Features and Heterogeneity of the Cr203-NiCr Systems, *Université de Technologie de Troyes*, 2021.

[120] G. Will, *Powder diffraction: the Rietveld method and the two-stage method to determine and refine crystal structures from powder diffraction data*. Springer, 2006.

[121] H. P. Klug and L. E. Alexander, *X-ray diffraction procedures for polycrystalline and amorphous materials*. Wiley, 1974.

[122] H. Imtiaz and T. Ahmed, Efficiency of XRD method for studying FRC composites – a review, *2nd Conference on Sustainability in Civil Engineering*, 2020.

[123] D. Stokes, *Principles and practice of variable pressure/environmental scanning electron microscopy (VP-ESEM)*. Wiley, 2008.

[124] F. Mokobi, Scanning Electron Microscope (SEM)- Definition, Principle, Parts, Images, Mar. 2022.

[125] K. Akhtar, S. A. Khan, S. B. Khan, and A. M. Asiri, Scanning Electron Microscopy: Principle and Applications in Nanomaterials Characterization, in *Handbook of Materials Characterization* (S. K. Sharma, ed.), 113–145, Springer International Publishing, 2018.

[126] A. Alyamani and O. M., FE-SEM Characterization of Some Nanomaterial, in *Scanning Electron Microscopy* (V. Kazmiruk, ed.), InTech, Mar. 2012.

[127] S. Foner, Versatile and Sensitive Vibrating-Sample Magnetometer, *Review of Scientific Instruments*, July 1959, **30**, 548–557.

[128] A. Adeyeye and G. Shimon, Growth and Characterization of Magnetic Thin Film and Nanostructures, in *Handbook of Surface Science*, vol. 5, 1–41, Elsevier, 2015.

[129] A. M. Glazer, Simple ways of determining perovskite structures, *Acta Crystallographica Section A*, Nov. 1975, **31**, 756–762.

[130] V. A. Khomchenko, L. C. J. Pereira, and J. A. Paixão, Mn substitution-induced revival of the ferroelectric antiferromagnetic phase in $Bi_{1-x}Ca_xFeO_{3-x/2}$ multiferroics, *Journal of Materials Science*, Feb. 2015, **50**, 1740–1745.

[131] D. P. Kozlenko, A. A. Belik, A. V. Belushkin, E. V. Lukin, W. G. Marshall, B. N. Savenko, and E. Takayama-Muromachi, Antipolar phase in multiferroic $BiFeO_3$ at high pressure, *Physical Review B*, Sept. 2011, **84**, 094108.

[132] A. A. Belik, A. M. Abakumov, A. A. Tsirlin, J. Hadermann, J. Kim, G. Van Tendeloo, and E. Takayama-Muromachi, Structure and Magnetic Properties of BiFe $_{0.75}$ Mn $_{0.25}$ O $_3$ Perovskite Prepared at Ambient and High Pressure, *Chemistry of Materials*, Oct. 2011, **23**, 4505–4514.

[133] D. C. Arnold, K. S. Knight, F. D. Morrison, and P. Lightfoot, Ferroelectric-Paraelectric Transition in $BiFeO_3$: Crystal Structure of the Orthorhombic Phase, *Physical Review Letters*, Jan. 2009, **102**, 027602.

[134] K. Poeppelmeier, M. Leonowicz, J. Scanlon, J. Longo, and W. Yelon, Structure determination of $CaMnO_3$ and $CaMnO_{2.5}$ by X-ray and neutron methods, *Journal of Solid State Chemistry*, Nov. 1982, **45**, 71–79.

[135] M. Azuma, H. Kanda, A. A. Belik, Y. Shimakawa, and M. Takano, Magnetic and structural properties of $BiMn_{1-x}Fe_xO_3$, *Journal of Magnetism and Magnetic Materials*, Mar. 2007, **310**, 1177–1179.

[136] C.-S. Tu, P.-Y. Chen, C.-S. Chen, *et al.*, Enhancement of local piezoresponse in samarium and manganese co-doped bismuth ferrite ceramics, *Journal of Alloys and Compounds*, Jan. 2020, **815**, 152383.

[137] C. Tian, Z. Tong, L. Huang, *et al.*, Mn Doping of $BiFeO_3$ for Microstructure and Electromagnetic Characteristics, *Journal of Superconductivity and Novel Magnetism*, Apr. 2021, **34**, 1199–1207.

[138] V. Khomchenko, M. Das, M. Henriques, and J. Paixão, Unusual magnetic properties of (Sr, Mn)-substituted $BiFeO_3$ near the polar/antipolar phase boundary, *Journal of Magnetism and Magnetic Materials*, Nov. 2023, **585**, 171142.

[139] I. Sosnowska, W. Schfer, W. Kockelmann, K. Andersen, and I. Troyanchuk, Crystal structure and spiral magnetic ordering of $BiFeO_3$ doped with manganese, *Applied Physics A: Materials Science & Processing*, Dec. 2002, **74**, s1040–s1042.

[140] K. Shigematsu, T. Asakura, H. Yamamoto, *et al.*, Room temperature ferromagnetism in $BiMn_{1-x}Fe_xO_3$ thin film induced by spin-structure manipulation, *Applied Physics Letters*, May 2018, **112**, 192905.

[141] C. Ederer and N. A. Spaldin, Weak ferromagnetism and magnetoelectric coupling in bismuth ferrite, *Physical Review B*, Feb. 2005, **71**, 060401.

[142] V. A. Khomchenko, M. V. Silibin, M. V. Bushinsky, *et al.*, Increased Low-Temperature Magnetization and Spin-Reorientational Transition in the Polar Phase of (Ca, Mn)-Doped Bismuth Ferrites, *physica status solidi (b)*, Aug. 2020, **257**, 2000121.

[143] V. Khomchenko, I. Troyanchuk, D. Többens, V. Sikolenko, and J. Paixão, Composition and temperature driven structural transitions in $Bi_{1-x}Ca_xFeO_3$ multiferroics: A neutron diffraction study, *Journal of physics. Condensed matter : an Institute of Physics journal*, 03 2013, **25**, 135902.

[144] V. A. Khomchenko, M. Das, J. A. Paixão, M. V. Silibin, and D. V. Karpinsky, Structural and magnetic phase transitions in Ca-substituted bismuth ferromanganites, *Journal of Alloys and Compounds*, 2022, **901**, 163682.

Supplementary material

Field dependencies of magnetization obtained for perovskite system $Bi_{1-x}Ca_xFe_{1-y}Mn_yO_3$ with temperatures ranging from T = 2 K to T = 325 K and magnetic field up to H = 90 kOe.

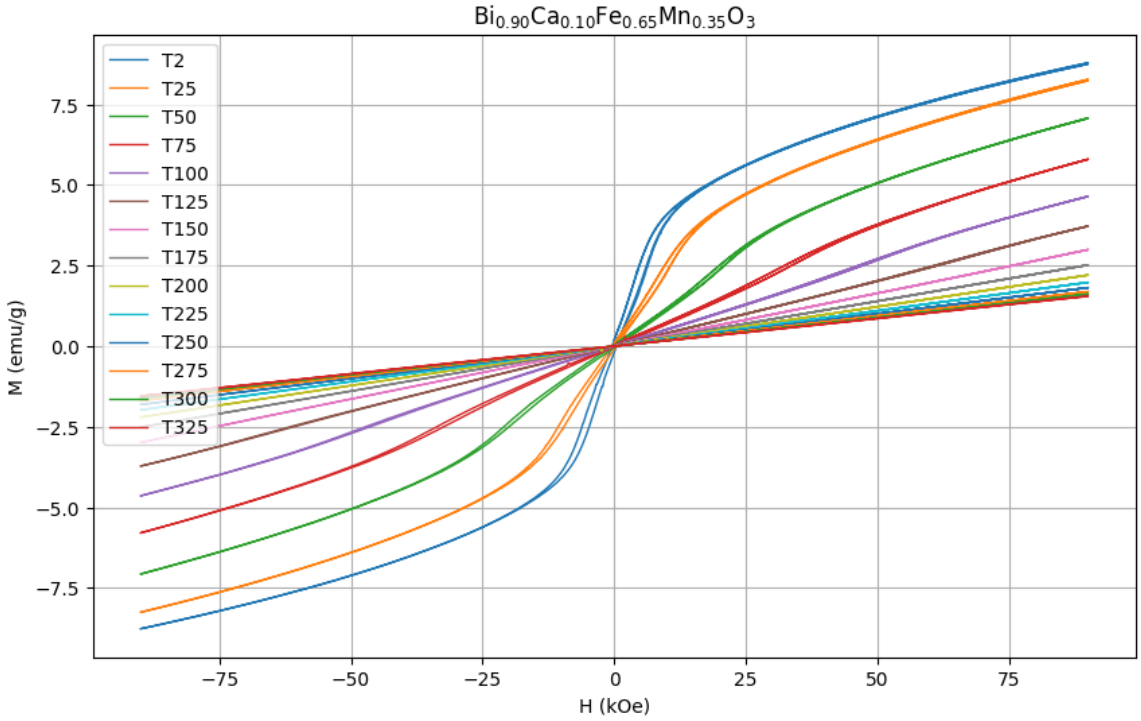

Fig. S1

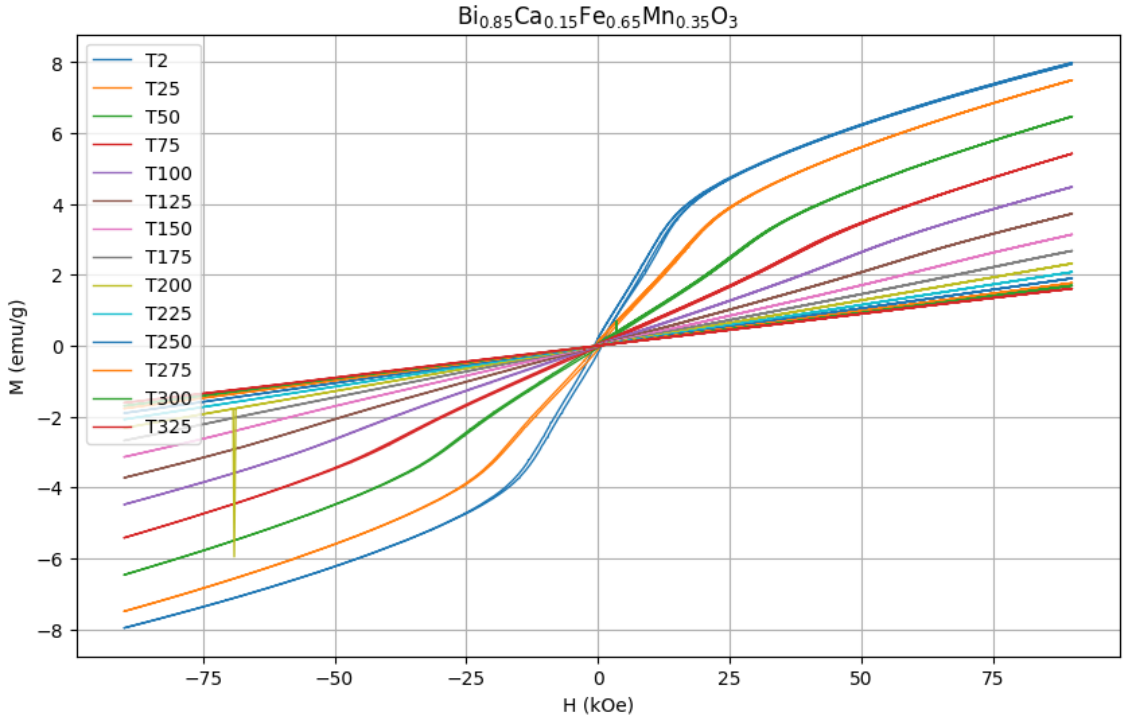

Fig. S2

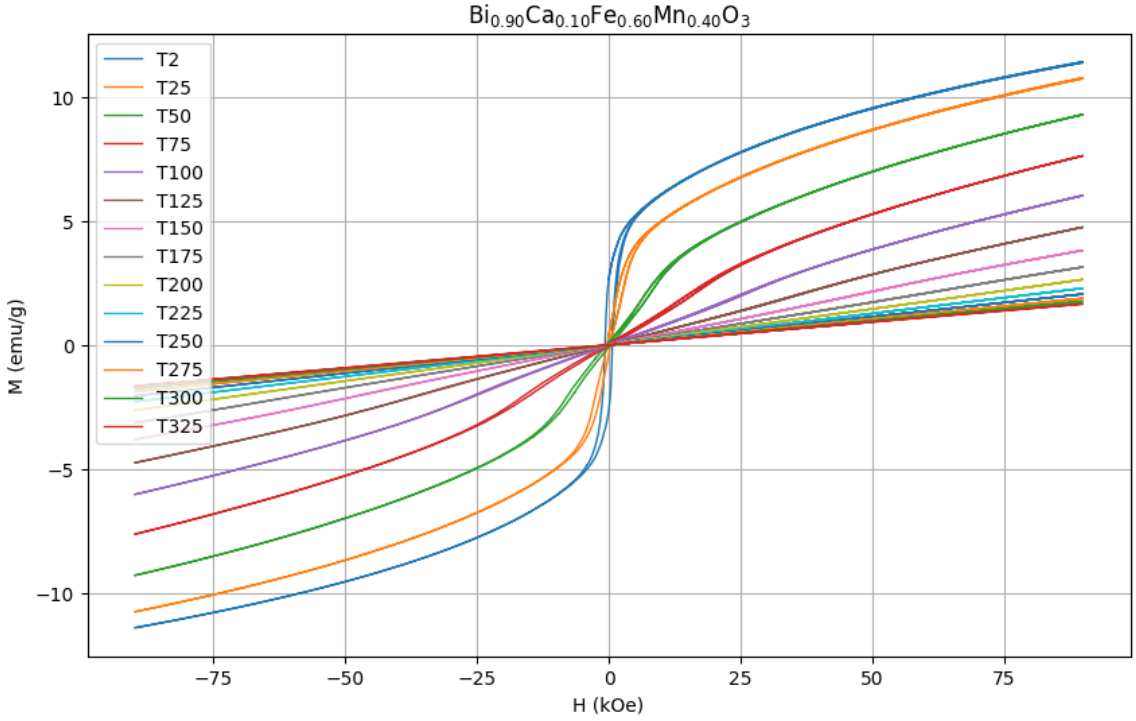
$Bi_{0.90}Ca_{0.10}Fe_{0.60}Mn_{0.40}O_3$
T2
T25
T50
T75
T100
T125
T150
T175
T200
T225
T250
T275
T300
T325
M (emu/g)
H (kOe)

Fig. S3

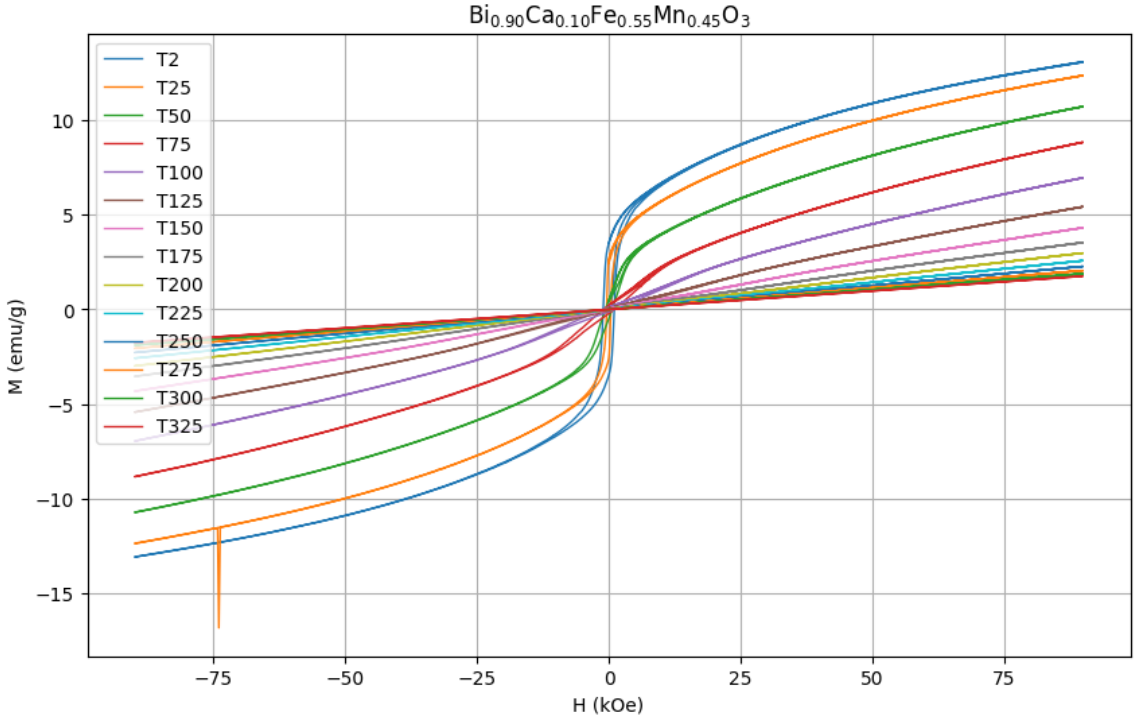
$Bi_{0.90}Ca_{0.10}Fe_{0.55}Mn_{0.45}O_3$
T2
T25
T50
T75
T100
T125
T150
T175
T200
T225
T250
T275
T300
T325
M (emu/g)
H (kOe)

Fig. S4

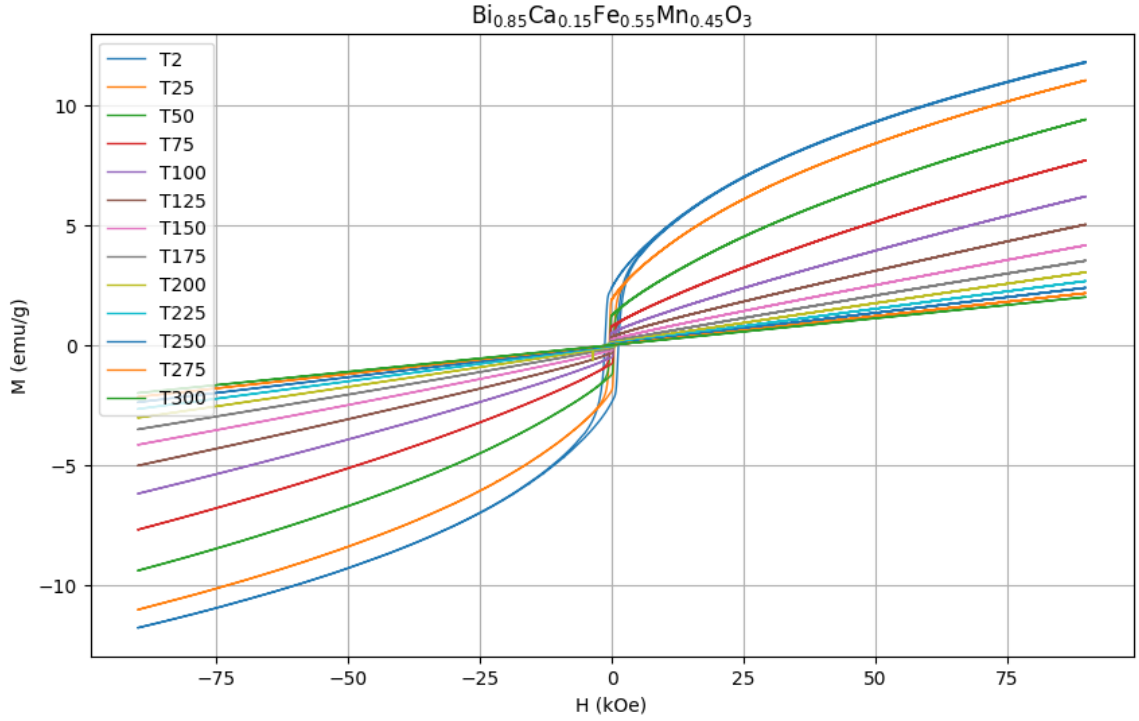
$Bi_{0.85}Ca_{0.15}Fe_{0.55}Mn_{0.45}O_3$
T2
T25
T50
T75
T100
T125
T150
T175
T200
T225
T250
T275
T300
M (emu/g)
H (kOe)

Fig. S5

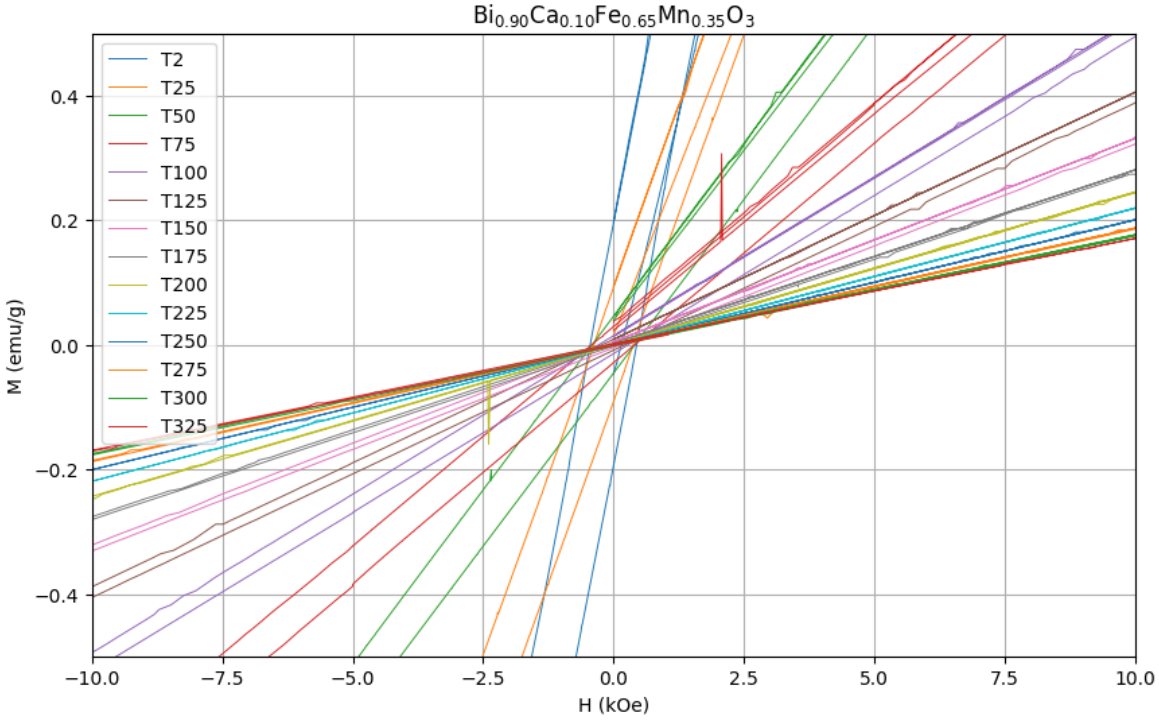
$Bi_{0.90}Ca_{0.10}Fe_{0.65}Mn_{0.35}O_3$
T2
T25
T50
T75
T100
T125
T150
T175
T200
T225
T250
T275
T300
T325
M (emu/g)
H (kOe)

Fig. S6

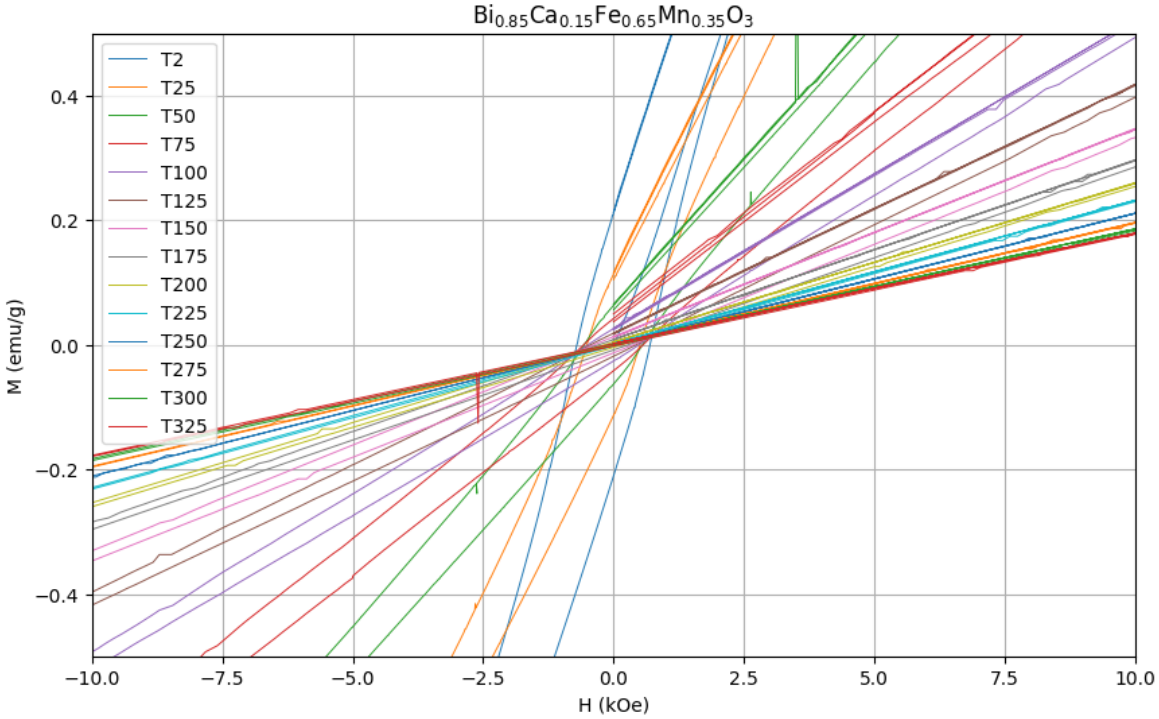
$Bi_{0.85}Ca_{0.15}Fe_{0.65}Mn_{0.35}O_3$
T2
T25
T50
T75
T100
T125
T150
T175
T200
T225
T250
T275
T300
T325
M (emu/g)
H (kOe)

Fig. S7

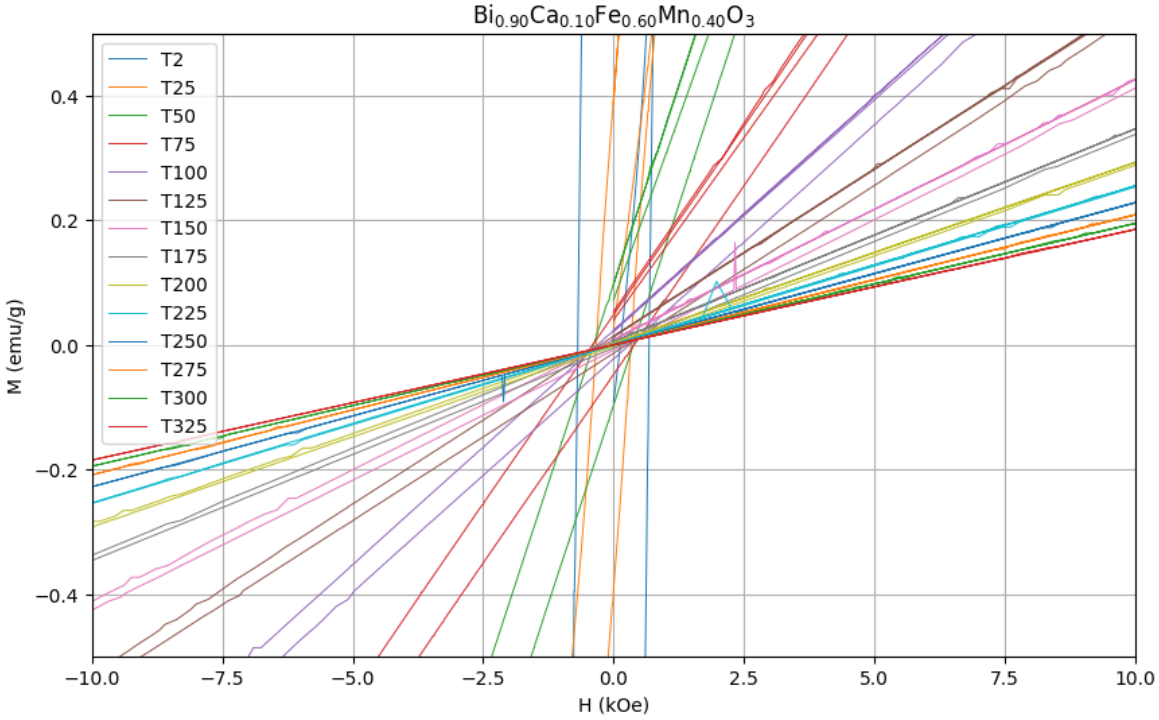
$Bi_{0.90}Ca_{0.10}Fe_{0.60}Mn_{0.40}O_3$
T2
T25
T50
T75
T100
T125
T150
T175
T200
T225
T250
T275
T300
T325
M (emu/g)
H (kOe)

Fig. S8

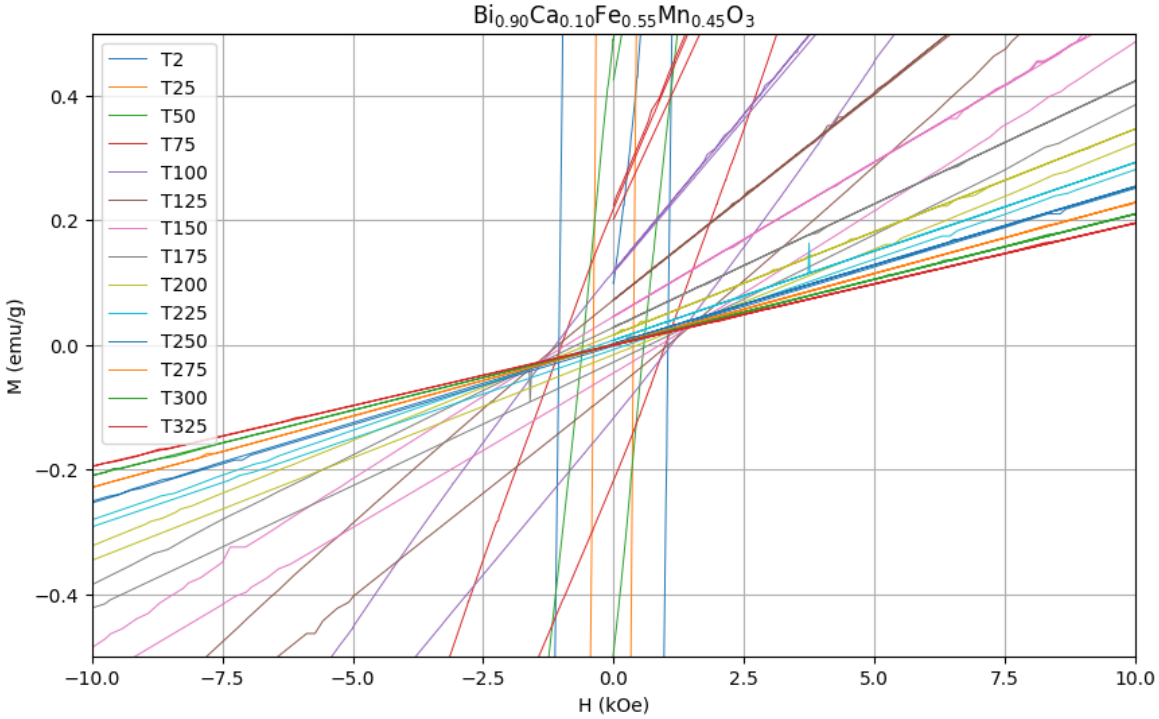

Fig. S9

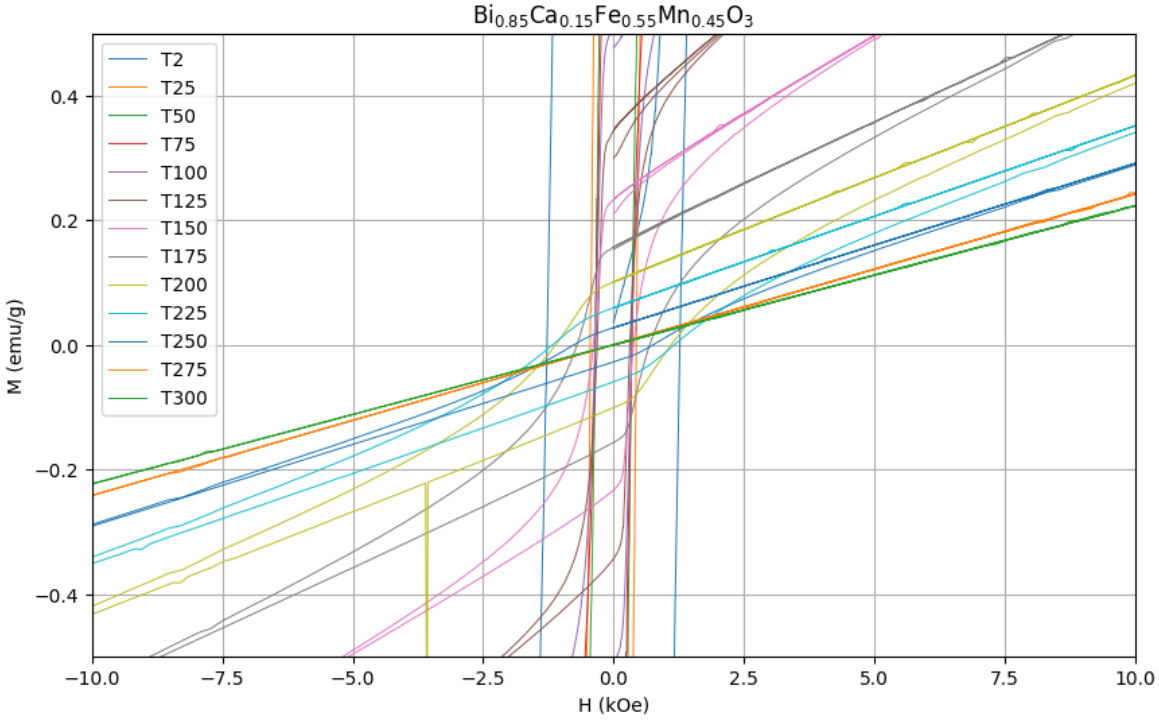

Fig. S10

$Bi_{1-x}Ca_xFe_{1-y}Mn_yO_3$ multiferoinių medžiagų magnetinės savybės ir kristalinė struktūra prie polinės-anti(ne)polinės fazių ribos

Mantas Skaržinskas

Santrauka

Multiferoinių medžiagų pasižyminčių magnetoelektrinėmis savybėmis vystymas išlieka svarbių tyrimų dėmesyje. Nors šioje srityje jau buvo padaryta pažanga, tam tikros sritys vis dar reikalauja gilesnio supratimo. Tyrėjams vis dar nepavyko rasti efektyvaus metodo, kaip sujungti spontanišką magnetizaciją ir poliarizaciją klasikiniame multiferoiniame junginyje, tokiame kaip $BiFeO_3$, kambario temperatūroje. Cheminės substitucijos įtaka medžiagos savybėms yra kritiška, nes tai stipriai veikia jos multiferoines savybes. Šis projektas siekia ištyrinėti alternatyvų metodą siekiant pasiekti didelę keičiamąją magnetizaciją feroelektriniame junginyje. Šis metodas apima dalinį pakeitimą Fe^{3+} jonų, mangano mišiniu (Mn^{3+}/Mn^{4+}) kuriame oksidacijos būsena užtikrina feromagnetinių mainų jungtį Mn^{3+}: $t_{2g}^3e_g^1$–O–Mn^{4+}: $t_{2g}^3e_g^0$. Toks metodas gali būti įgyvendintas $Bi_{1-x}AE_xFe_{1-y}Mn_yO_3$ sistemose, kuriose įkrovos disbalansas atsiranda pakeitus Bi^{3+} su AE^{2+} ir yra kompensuojamas Mn^{4+} (egzistuoja kartu su Mn^{3+}, kai y > x) [2]. Šio baigiamojo darbo metu buvo atlikti rentgeno spindulių difrakcijos, skenuojančios elektroninės mikroskopijos bei vibruojančio mėginio magnetometrijos matavimai, skirti nustatyti $Bi_{1-x}Ca_xFe_{1-y}Mn_yO_3$ perovskito sistemoje esančių mėginių kristalines struktūras ir magnetines savybes. Rentgeno spindulių difrakcijos (XRD) matavimai ir Retvield profilio tikslinimo analizė atskleidė mėginių kristalografinę struktūrą bei leido identifikuoti struktūrinį perėjimą iš polinės į anti(ne)polinę fazę. Šis perėjimas tampa pastebimas, kai vertės x = 0.10 (antipolinė), x = 0.15 (nepolinė) bei pradeda atsirasti Mn koncentracijos intervale $0.40 < y < 0.45$. Junginiai su koncentracija $y \leq 0.40$ demonstravo nuoseklų sutapimą su primityviąją pseudokubine pervoskito kristaline gardele, kuri priklauso $R3c$ erdvinei grupei ir leido patvirtinti šių junginių feroelektrinę prigimtį. Skenuojančios elektroninės mikroskopijos vaizdų analizė atskleidė, kad yra skirtingos grūdelių ribos, nurodančios grūdelių dydžių pokyčius ir skirtingų kristalinių domenų egzistavimą mėginyje. Be to, tyrimas patvirtina mėginio fazinį grynumą, lyginant antrinius elektronų mikroskopijos vaizdus ir atgal išsklaidytus elektronų mikroskopijos vaizdus. Šiuo atveju nepastebėta nuo kompozicijos priklausomų vaizdo kontrasto svyravimų, o tai rodo, kad mėginyje nėra antrinių fazių. Vibruojančio mėginio magnetometrijos matavimai rodo, kad visi mėginiai pasižymi linijine priklausomybe nuo magnetinio lauko, o tai sąlygoja paramagnetinę arba kolinearinę (G-tipo) antiferomagnetinę būseną kambario temperatūroje. Mėginiai su y = 0.35, 0.40 parodė neįprastą priklausomybę nuo temperatūros, kurios metu vyksta perėjimas nuo kolinearinės G-tipo antiferomagnetinės būsenos prie silpnai feromagnetinės būsenos temperatūrai mažėjant. Be to, magnetizacija mėginiuose, kai T = 2 K su sudėtimi [0,10, 0,40], [0,10, 0,45], [0,15, 0,45], žymiai viršija įprastai gaunamas vertes, būdingas silpnai feromagnetiniams bismuto feritams prie polinės/anti(ne)polinės fazių ribos.

Acknowledgments

I am deeply grateful to Prof. Dr. Uladzimir Khomchanka for his invaluable guidance, unwavering support, encouragement of academic freedom, profound wisdom and understanding throughout the journey that began at the University of Coimbra - Department of Physics and culminated in the completion of this thesis. His expertise, dedication and mentorship have significantly shaped my perspective and played a crucial role in shaping my vision for further growth and the successful culmination of this endeavor.

Additionally, I want to thank Prof. Dr. Rui Davide Martins Travasso for the warm welcome at the University of Coimbra and for helping me to find a suited research area. Furthermore, I am grateful to Prof. Dr. José António De Carvalho Paixão for setting an example of curiosity and enthusiasm driven exploration.

Moreover, I extend my gratitude to Laima Dumbravienė, Doc. Dr. Olga Rancova, and Prof. Dr. Vincas Tamošiūnas for their assistance in navigating the complexities surrounding my thesis within the Erasmus+ programme.